CARDIFF UNIVERSITY

Tantalum Oxide Anti-Reflective Thin Films for

C-Band Travelling-Wave Semiconductor Optical Amplifiers

Josie Travers-Nabialek

A thesis submitted in partial fulfilment for the degree of

Master of Philosophy

School of Physics and Astronomy

December 2023

"The thing that doesn't fit is the thing that's the most interesting: the part that doesn't go according to what you expected."

Richard Feynman

Abstract

The work in this thesis describes an approach to suppressing cavity resonances in Travelling-Wave Semiconductor Optical Amplifiers (TW-SOA) by application of a single layer anti-reflective thin film, tuned for C-Band (1530-1565 nm) emission.

A 215 nm layer of tantalum oxide (TaO_x) is applied to both facets of AlGaInAs/InP ridge waveguide (RWG) Fabry-Pérot (F-P) laser diodes (LD) via electron-beam (e-beam) evaporation. E-beam evaporation allows a dielectric layer, thicker than 200 nm, to be deposited onto many LD facets in a cost-effective and time efficient manner. This deposition technique is chosen as it allows the refractive index of the antireflection coating (ARC) to be tuned to produce a TaO_x layer of the required refractive index, n_{film}, by exploiting the relationship between n_{film} and chamber pressure during evaporation.

Monitoring the power-current characteristics and emission spectrum from the devices before and after coating demonstrates the successful realisation of a TW-SOA where lasing is no longer present. Remaining cavity resonances show gain ripple, G_r, values across the C-Band gain spectrum of ≤ 0.1 dB with a maximum of 0.5 dB at injection currents over three times the original laser threshold current. These values are competitive when compared to commercially available SOAs operating across the same wavelength region. The remaining FP fringes observed in the Amplified Spontaneous Emission (ASE) spectrum of the TW-SOA are consistent with geometric mean facet reflectivity, $\sqrt{R_1 R_2}$, values as low as 10^{-4} and 10^{-5} across the C-Band wavelength range (1530-1565 nm) of interest.

The results in this thesis show promise for the future use of TaO_x thin films to improve the performance of Distributed Feedback (DFB), and Distributed Bragg Reflector (DBR) laser diodes, or as an effective antireflection coating for different types of semiconductor optical amplifiers.

Acknowledgments

I would like to take this opportunity to acknowledge and thank all my colleagues at Cardiff University for their guidance and support over the last 5 years, and in particular, the duration of this project. I feel incredibly lucky to work amongst a group of talented and inspirational people, who also know all the best pubs in Cardiff!

I would like to begin by extending my utmost gratitude to my primary supervisor Professor Peter Smowton. I whole-heartedly believe that without this opportunity my future would look very different. Thank you for your encouragement, honesty, sense of humour, and continuing to listen even when I've talked at you excitedly for 15 minutes straight.

A big thank you to my secondary supervisor, line manager, and most importantly friend, Dr Sam Shutts. You are the most chilled out person I know and have always given me perspective on what's worth freaking out about, and what's not. Thank you for your time, patience, and understanding, and rescuing me on the occasions my car has died! You've helped me develop many scientific and technical skills, which have been invaluable to me during this project.

I would like to give special thanks to Dr Sara-Jayne Gillgrass for her contribution to the thin film development and fabrication of devices. This work would not have been possible without you. Thank you for your invaluable advice, guidance, and support throughout my time at the university, as well as your friendship. My taste in coffee has definitely improved, and I can guarantee the word count from our exchange of messages exceeds that of this thesis.

I'd also like to thank Dr Zhongming Cao for assisting with device fabrication and providing feedback on presentation abstracts, as well as Dr Richard Forrest for his outstanding engineering and CAD skills. Your ability to make an idea a reality is highly valued and without your help, those tiny SOAs would've got very lost in that big evaporator. Special thanks to Dr Dagmar Butkovicova, who appreciates the struggle in juggling a full-time job and research. Your kindness, support, and advice has been warmly received. Thanks to Dr Craig Allford for sharing endless experimental knowledge, and for always knowing where everything is.

Thanks to all my family and friends, especially my parents, Trudi and Peter. You are biggest supporters who always encourage me to be humble, curious, and fearless in my pursuit for happiness and success. Thank you for everything you've done, and continue to do for me, for that I am eternally grateful.

Last, but certainly not least, thank you to my wonderful wife Sophie who has shown me so much love and support along this journey. You've taken care of our home when I struggled to find time and kept me in an unlimited supply of Diet Coke and coffee during the endless hours of writing this thesis. Without your patience, support, and goofy sense of humour, I would not have made it through these last 3 years. It is to you that I dedicate this work.

Contents

Chapter 1 Introduction

Chapter 2 Background Scientific Theory

Chapter 3 Modelling and Simulations

Chapter 4 Fabrication and Sample Preparation Techniques

Chapter 5 Experimental Characteristics

Chapter 6 Conclusion and Future Work

Appendix A

Appendix B

Appendix C

Appendix D

List of Figures and Tables

Abbreviations

SOA Semiconductor Optical Amplifier

TW-SOA Travelling-Wave Semiconductor Optical Amplifier

OFA Optical Fibre Amplifier

EDFA Erbium-Doped Fibre Amplifier

ASE Amplified Spontaneous Emission

PIC Photonic Integrated Circuit

MWQ Multiple Quantum Well

PVD Physical Vapour Deposition

CVD Chemical Vapour Deposition

RIE Reactive Ion Etching

ICP Inductively Coupled Plasma

MOCVD Metalorganic Chemical Vapour Deposition

ARC Anti-Reflection Coating

ALD Atomic Layer Deposition

FP Fabry-Pérot

DBR Distributed Bragg Reflector

DFB Distributed Feedback

LD Laser Diode

DOS Density of States

RWG Ridge Waveguide

SRH Shockley-Read-Hall

FDE Finite Difference Eigenmode

FDTD Finite Difference Time Domain

GUI Graphical User Interface

TE Transverse Electric

TM Transverse Magnetic

SCH Separate Confinement Heterostructure

Chapter 1

Introduction

1.1 Thesis Rationale

Laser amplifiers have been a topic of discussion from as early as the 1960's **[1]** but gained considerably more attention across the mid 1980-1990's which saw the development of semiconductor optical amplifiers comparable to those commercially available today **[2]**. Their low power consumption and small footprint mean they are easily integrated with other passive and active optical components in modern Photonic Integrated Circuits (PIC) to perform a series of different functions, such as mitigating power losses of integrated lasers, or wavelength tuning of propagating optical signals. Tuning the epitaxial layers in the device, has enabled the realisation of SOAs that can amplify optical signals over a wide range of wavelengths. Further optimisation of the waveguiding region increases modal confinement and selectivity to allow single mode/multimode amplification and numerical aperture matching between neighbour components in PIC or fibres in optical communication systems. Strained and unstrained bulk semiconductor active layers have been used to make polarisation insensitive SOAs for optical network applications, including in-line and pre-amplifiers, and fast optical switches **[3-6]**. The non-linear behaviour, predominantly seen in quantum confined SOAs, can be exploited to produce frequency and wavelength converters **[7-10]**, phase modulators **[11]**, and multiplexers/demultiplexers **[12]**.

In its most basic form, an SOA offers an attractive solution for mitigating absorption and scattering losses experienced in optical fibre communication systems operating in the 1310 nm and 1550 nm window - wavelengths within the spectrum where attenuation is lower, but not completely absent. Fibre attenuation causes signal power losses which can in-turn significantly limit the transmission distance of the optical signal, whereas material dispersive effects, due to the wavelength dependence of the refractive index on the core material within the fibre, leads to broadening of the optical pulse, limiting the fibre bandwidth, and increasing system bit error rate **[13]**. Much work has already been done to realise 1310 nm SOAs to support these systems, but scattering losses are higher at shorter wavelengths, and therefore 1550 nm optical fibre communication systems are also desirable. Hence C-Band (1530-1565 nm) SOAs remain an active area of research and thus the focus of this work.

1

There are still challenges to overcome when producing SOAs since they typically possess some less desirable characteristics, when compared to Optical Fibre Amplifiers (OFA), such as Erbium-Doped Fibre Amplifiers (EDFAs). EDFAs typically consist of a silica cladding region that surrounds a core (gain region) that is doped with erbium (Er) ions, which are stimulated into an excited state when interacting with an optical pump signal of a given wavelength (1528-1620 nm). The relaxation of the Er ions to a lower energy level results in the emission of photons with the same properties as those that stimulated their release, thus the injected optical signal is amplified along the length of the EDFA and ejected at the other end, as seen in Figure 1.1.1. Despite their useful implementation in datacom systems, EDFAs are known to have a large footprint, and longer upper-state lifetime which makes them less practical for use in PICs and fast-switching applications.
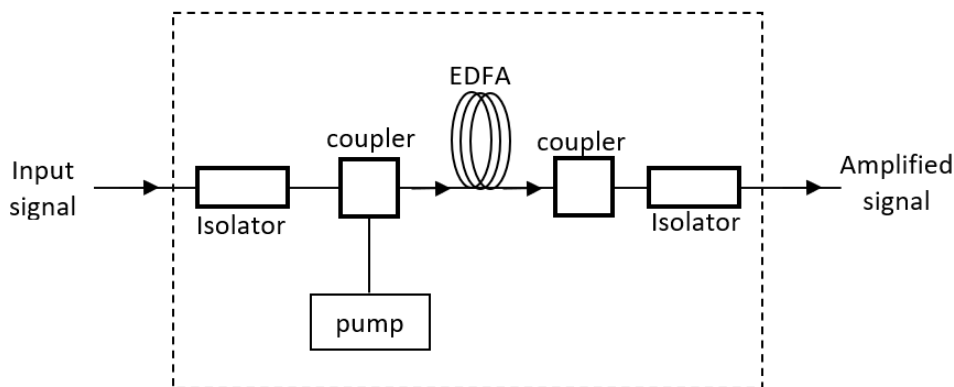
Figure 1.1.1: Diagram showing the typical layout of an EDFA system.

However, SOAs typically have higher values of noise figure and gain ripple which usually originate from the difficulty in reducing the facet reflectivity to a level necessary to achieve gain ripple values ≤ 0.5 dB. A geometric mean facet reflectivity, $\sqrt{R_1 R_2}$, as low as 10^{-4} is typically required for targeting lower gain ripple, and thus achieving higher single pass gain. To achieve this value of $\sqrt{R_1 R_2}$, previously explored techniques include tilted waveguide SOAs, as seen in Figure 1.1.2, where, as the name suggests, the waveguide region is tilted at an angle somewhere between 7°-10° off-axis with the semiconductor crystal plane, causing light to be reflected away from the resonant cavity mode instead of being unwantedly coupled back into the waveguide. A tilted waveguide can be useful in systems where the light coupling between waveguide and neighbouring fibre/components are not as crucial. However, it can be more challenging to produce a low reflectivity single mode tilted waveguide SOA at 1550 nm than 1310 nm since the proportion of reflected light is dependent on the overlap integral which contains an exponential term with an inverse proportionality dependence on wavelength, as described in **[14]**.

2

A specific waveguide geometry is necessary for single (lateral) mode SOA, but this gives rise to a smaller mode width, and therefore a higher effective facet reflectivity, typically in the region of 10^{-2} to 10^{-3} within the 7°-10° tilt angle range [15]. Two things can be done at this stage, one is to further increase the tilt angle of the waveguide, or the second is to coat the facets with a single/double layer ARC. Some issues can arise from this arrangement, increasing the tilt angle beyond 10° results in increased coupling losses between the SOA and optical fibres and neighbouring components. Applying an ARC to a tilted waveguide means that the light coupled to and from the waveguide strikes the coating at an oblique angle, changing the optical path length of the light, and shifting the reflectivity minimum away from the desired wavelength.
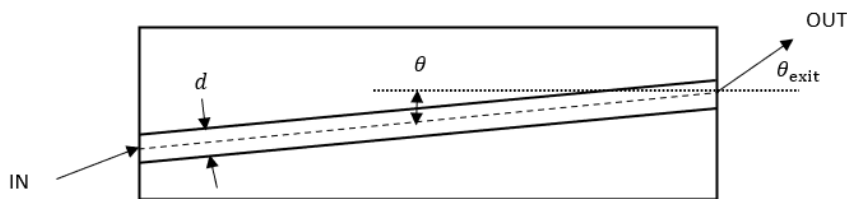
Figure 1.1.2: Top-down view of a titled waveguide SOA.

Angled facets have also been used to reduce optical feedback, with the same principle as the tilted waveguide, but this time the facet is etched to form the desired angle. Etching facets is a challenging task, since it can be difficult to control the etch with the precision needed for an angle error of less than 1°. Several issues can arise in etched facet devices, the first being deviations from the ideal facet angle, which can lead to higher values of facet reflectivity and thus increased gain ripple (5-6 dB) [16]. Secondly, the etching process can leave behind a rough facet surface, which leads to increased scattering losses and decreased fibre-to-fibre gain. Surface states and defects can also occur from a rough etch profile, giving rise to non-radiative recombination, increased photon absorption, and increased heating at the facet, consequently leading to Catastrophic Optical Damage (COD) and loss of the device [17].

Probably the most popular choice to suppress cavity resonances in SOAs is by deposition of an antireflective thin film, typically made of multiple layers of alternating high/low refractive index materials to reach the desired reflectivity values across a broad range of wavelengths [18-20]. Multilayer coatings are often complex to design, expensive to fabricate, and require precise thickness control over each layer to ensure the required reflectivity is achieved. Single layer AR-coatings are simpler to design but have practical limitations. The first is due to limited materials available with the required refractive indices (n_{film}=1.8-1.9) to match the effective index of the material used in the epitaxial stack of C-Band devices (n_{eff}=3.2-3.8). Small deviations from the

ideal refractive index (0.1) can lead to reflectivity values outside the range for a practical TW-SOA. However, by choosing a suitable metal-oxide and deposition technique, it is possible to tune the refractive index and thickness of the coating to produce a single layer antireflective thin film that has the required optical properties. One such material is tantalum pentoxide, Ta_2O_5, which has gained much interest for its use in optoelectronic applications spanning the visible and near infra-red (NIR) regions [21]. Ta_2O_5 has many desirable optical properties, such as negligible absorption over a wide range of wavelengths (<400 nm to 8 µm) [22], high resistance to laser damage, and resistance to moisture and environmental factors [23], all of which make it a favourable choice as an AR-coating for LD facets. Tantalum oxide films can be deposited via a number of different chemical and physical vapour deposition (PVD/CVD) techniques, such as plasma enhanced and low-pressure CVD, RF magnetron sputtering, atomic layer deposition (ALD), and electron-beam evaporation [24-30]. E-beam evaporation is a desirable deposition process for this work as it enables metal-oxide films to be fabricated with the desired optical properties by controlling the conditions within the chamber during the deposition phase.

This work aims to realise a single (lateral) mode TW-SOA which uses electron-beam evaporation to coat both facets with a single layer TaO_x antireflective thin film, optimised to reduce cavity resonances and exhibits competitively low gain ripple (<0.5 dB) and low geometric mean facet reflectivity values (10^{-4}) across the C-Band region.

1.2 Thesis Outline

This thesis beings (Chapter 2) with an overview of the scientific theory and concepts that are relevant to the work in the proceeding chapters. Chapter 3 details modelling, and simulation work carried out to find the most appropriate waveguide geometry for the device, followed by modelling of the thin film parameters key to reducing optical feedback in the C-Band TW-SOA. Chapter 4 outlines the steps taken to fabricate RWG F-P devices with different ridge widths and heights. This is followed by thin film development work that uses e-beam evaporation to deposit a TaO_x ARC onto bare InP substrates; first to optimise the films properties before subsequently applying the coating to the F-P device facets. Chapter 5 describes the experimental work carried out to test the performance of different RWG structures and the TaO_x coating, including details of the coated facet reflectivity and gain ripple values of the TW-SOAs. This chapter concludes with comparisons between experimental and simulated values of reflectivity to help explain the differences observed in the two datasets. To finish, Chapter 6 presents the conclusion of the work in this thesis, including suggestions for future work that could be carried out.

Chapter 1 References

[1] H. Steinberg, "The use of a laser amplifier in a laser communication system," in *Proceedings of the IEEE*, vol. 51, no. 6, pp. 943-943, June 1963, doi: 10.1109/PROC.1963.2342.

[2] Aneesh Sobhanan, Aravind Anthur, Sean O'Duill, Mark Pelusi, Shu Namiki, Liam Barry, Deepa Venkitesh, and Govind P Agrawal, "Semiconductor optical amplifiers: recent advances and applications," Adv. Opt. Photon. 14, 571-651 (2022).

[3] C. Holtmann, P. A. Besse, T. Brenner and H. Melchior, "Polarization independent bulk active region semiconductor optical amplifiers for 1.3 µm wavelengths," in *IEEE Photonics Technology Letters*, vol. 8, no. 3, pp. 343-345, March 1996, doi: 10.1109/68.481111.

[4] M. Itoh, Y. Shibata, T. Kakitsuka, Y. Kadota and Y. Tohmori, "Polarization-insensitive SOA with a strained bulk active layer for network device application," in *IEEE Photonics Technology Letters*, vol. 14, no. 6, pp. 765-767, June 2002, doi: 10.1109/LPT.2002.1003086.

[5] K. Morito, M. Ekawa, T. Watanabe and Y. Kotaki, "High-output-power polarization-insensitive semiconductor optical amplifier," in *Journal of Lightwave Technology*, vol. 21, no. 1, pp. 176-181, Jan. 2003, doi: 10.1109/JLT.2003.808643.

[6] C. Michie, A. E. Kelly, J. McGeough, I. Armstrong, I. Andonovic and C. Tombling, "Polarization-Insensitive SOAs Using Strained Bulk Active Regions," in *Journal of Lightwave Technology*, vol. 24, no. 11, pp. 3920-3927, Nov. 2006, doi: 10.1109/JLT.2006.883119.

[7] D. Marcenac and A. Mecozzi, "Switches and frequency converters based on cross-gain modulation in semiconductor optical amplifiers," in *IEEE Photonics Technology Letters*, vol. 9, no. 6, pp. 749-751, June 1997, doi: 10.1109/68.584978.

[8] D. T. Schaafsma and E. M. Bradley, "Cross-gain modulation and frequency conversion crosstalk effects in 1550-nm gain-clamped semiconductor optical amplifiers," in *IEEE Photonics Technology Letters*, vol. 11, no. 6, pp. 727-729, June 1999, doi: 10.1109/68.766799.

[9] S. J. B. Yoo, "Wavelength conversion technologies for WDM network applications," in *Journal of Lightwave Technology*, vol. 14, no. 6, pp. 955-966, June 1996, doi: 10.1109/50.511595.

[10] T. Durhuus, B. Mikkelsen, C. Joergensen, S. Lykke Danielsen and K. E. Stubkjaer, "All-optical wavelength conversion by semiconductor optical amplifiers," in *Journal of Lightwave Technology*, vol. 14, no. 6, pp. 942-954, June 1996, doi: 10.1109/50.511594.

[11] P. P. Baveja, D. N. Maywar, A. M. Kaplan and G. P. Agrawal, "Self-Phase Modulation in Semiconductor Optical Amplifiers: Impact of Amplified Spontaneous Emission," in *IEEE Journal of Quantum Electronics*, vol. 46, no. 9, pp. 1396-1403, Sept. 2010, doi: 10.1109/JQE.2010.2048743.

[12] W. H. Chung, Hwa-Yaw Tam, P. K. A. Wai and A. Khandelwal, "Time- and wavelength-division multiplexing of FBG sensors using a semiconductor optical amplifier in ring cavity configuration," in *IEEE Photonics Technology Letters*, vol. 17, no. 12, pp. 2709-2711, Dec. 2005, doi: 10.1109/LPT.2005.859484.

[13] M. J. Connelly, "Semiconductor Optical Amplifiers", Springer New York, NY, 978-0-7923-7657-6Published: 31 January 2002.

[14] C. E. Zah, R. Bhat, S. G. Menocal, N. Andreadakis, F. Favire, C. Caneau, M. A. Koza, and T. P. Lee, "1.5-µm GaInAsP angled-facet flared-waveguide traveling wave laser amplifiers," in *Optical Fiber Communication*, OSA Technical Digest (Optica Publishing Group, 1990), paper THB3.

[15] G De Valicourt, GH Duan, C Ware, M Lamponi, R Brenot, Experimental and theoretical investigation of mode size effects on tilted facet reflectivity", *IET Optoelectronics,* Vol. 5, No. 4, August 2011.

[16] L. Schares, R. Budd, D.Kuchta, F.Doany, C.Schow, M. Möhrle, A.Sigmund, W.Rehbein., "Etched-facet semiconductor optical amplifiers for gain-integrated photonic switch fabrics," *2015 European Conference on Optical Communication (ECOC)*, Valencia, Spain, 2015, pp. 1-3, doi: 10.1109/ECOC.2015.7341614.

[17] Ralph Doud Whaley, Jr., "Development and Analysis of Etched-Facet InP-based Active Photonic Components for Monolithically Integrated Fiber Coupling Assemblies" PhD Thesis*,* University of Maryland, 2001

[18] F. Lemarquis, T. Begou, A. Moreau, J. Lumeau, "Broadband antireflection coatings for visible and infrared ranges", CEAS Space J 11, 567–578 (2019). https://doi.org/10.1007/s12567-019-00266-8.

[19] Dale E. Morton, Ian Stevenson, Michel Garcia, "Design and development of optical coatings on laser bar facets", Proceedings Volume 5280, Materials, Active Devices, and Optical Amplifiers; (2004) https://doi.org/10.1117/12.519032.

[20] H. K. Raut, V. Anand Ganesh, A. Sreekumaran Nair, S. Ramakrishna, "Anti-reflective coatings: A critical, in-depth review", *Energy Environ. Sci.*, Vol. 4, Issue. 10, pp. 3779-3804, March 2011. DOI: 10.1039/C1EE01297E.

[21] C. Chaneliere, J.L. Autran, R.A.B. Devine, B. Balland, "Tantalum pentoxide (Ta2O5) thin films for advanced dielectric applications", *Material. Sci. Eng.,* Vol. 22, Issue. 6, pp. 269–322, May 1998, https://doi.org/10.1016/S0927-796X(97)00023-5.

[22] M. Audier, B. Chenevier, H. Roussel, L. Vincent, A. Peña, A. Lintanf Salaün, "A very promising piezoelectric property of Ta2O5 thin films. II: Birefringence and piezoelectricity", *Journal of Solid-State Chemistry,* Vol. 184, Issue 8, pp. 2033-2040, August 2011. https://doi.org/10.1016/j.jssc.2011.06.002.

[23] M. Kumar, N. Kumari, VSRS P. Kumar, V. Karar, A. L Sharma, "Determination of optical constants of tantalum oxide thin film deposited by electron beam evaporation", *Materialstoday: proceedings*, Vol. 5, Issue 2, Part 1, pp. 3764-3769, 2018. https://doi.org/10.1016/j.matpr.2017.11.629.

[24] M. T. Seman, J. J. Robbins, D. Leonhardt, S. Agarwal and C. A. Wolden, "Comparison of Electrolyte Performance for Ta2O5 Thin Films Produced by Pulsed and Continuous Wave PECVD", *Journal Electrochem. Soc.,* Vol. 155, No. 6, April 2008. DOI 10.1149/1.2901139

[25] H. Treichel, A. Mitwalsky, N. P. Sandler, D. Tribula, W. Kern, A. P. Lane, "Low-Pressure chemical vapour deposition of tantalum pentoxide films for ulsi devices using tantalum pentaethoxide as precursor", *Advanced Materials for Optics and Electronics*, Vol. 1, Issue. 6, pp. 299-308, December 1992. https://doi.org/10.1002/amo.860010607.

[26] S.V. Jagadeesh Chandra, Chel-Jong Choi, S. Uthanna, G. Mohan Road, "Structural and electrical properties of radio frequency magnetron sputtered tantalum oxide films: Influence of post-deposition annealing", *Materials Science in Semiconductor Processing*, Vol. 13, Issue. 4, pp. 245-251, December 2010. https://doi.org/10.1016/j.mssp.2010.08.002.

[27] K. Kukli, J. Aarik, A. Aidla, O. Kohan, T. Uustare, V. Sammelselg, "Properties of tantalum oxide thin films grown by atomic layer deposition", *Thin Solid Films*, Vol. 260, Issue. 2, pp. 135-142, May 1995. https://doi.org/10.1016/0040-6090(94)06388-5.

[28] Z. Todorova, et al., "Electrical and Optical Characteristics of Ta2O5 Thin Films Deposited by Electron-Beam Vapor Deposition", *Plasma Processes and Polymers*, Vol. 3, No. 2, pp. 174-178, November 2005. https://doi.org/10.1002/ppap.200500110.

[29] A. Kulpa, N. A. Jaeger, "Comparison of the Optical Properties of Tantalum Pentoxide, Ta2O5, Anodically Grown from E-beam Deposited Tantalum, Ta, with Ta2O5 E-beam Deposited from a Ta2O5 Source", ECS Trans., Vol. 41, No. 3, pp. 311-314, 2011. DOI 10.1149/1.3633047.

[30] G. A. Al-Jumaily, S. M. Edlou, "Optical properties of tantalum pentoxide coatings deposited using ion beam processes", Thin Film Solids, Vol. 209, Issue. 2, pp. 223-229, March 1992. https://doi.org/10.1016/0040-6090(92)90679-6.

Chapter 2

Background Scientific Theory

The following chapter is a brief overview of the scientific terms and concepts that are relevant to the work carried out in this project. For a more comprehensive description and deeper understanding of the material within each subsection, the reader is encouraged to refer to the references at the end of the chapter.

Subsection 2.1 details the working principle of a semiconductor optical amplifier (SOA). Subsection 2.2 describes the fundamental building blocks of the multiple-quantum well (MQW) SOAs used in this work, including the P-i-N junction, density of states (DOS), Fermi-Dirac distribution of carriers, and how a junction in forward-bias can lead to an inverted carrier population. Subsection 2.3 outlines the light-matter interactions that take place within an SOA under electrical and optical pumping, drawing particular attention to the phenomenon of amplified spontaneous emission (ASE) which is essential to understanding the observations detailed in Chapter 5 of this thesis. Subsection 2.4 describes the theory of transforming an F-P LD to a TW-SOA by applying a single layer ARC to the facets at either end of the device cavity. This is followed by details of how the remaining F-P fringes, observed in the ASE spectrum of the TW-SOA, can be used to extract the facet reflectivity of the device after coating. Subsection 2.5 and 2.6 discusses the optical properties of dielectric materials typically used for an ARC, including the thin film interference effects that are key to understanding the interaction of electromagnetic fields travelling between media of varying refractive index and thickness. This theory forms the basis for the design and optimisation of the TaO_x ARC used in this work.

2.1 Operating Principles of TW-SOA

An SOA is an optoelectronic device that can be used for the amplification of optical signals spanning single or multiple wavelengths, dependent upon application. This work focuses on a Travelling-Wave (TW) SOA that amplifies light of a single (or narrow band) of wavelengths. The gain chips can be packaged with butterfly-type terminals and a variety of single mode (SM) or polarisation-maintaining (PM) fibres, allowing them to be easily incorporated into fibre optic communication systems to mitigate losses that arise from attenuation, dispersion, and scattering effects within the fibre.

A TW-SOA is somewhat comparable to that of a LD, where both devices have an intrinsic active (gain) region sandwiched between p-and n-type doped semiconductor materials to form a

P-i-N junction. The structure of the active region is chosen to suit the application. The most basic structures are composed of a bulk semiconductor material, but more complex applications take advantage of quantum confined nanostructures such as quantum wells, wires, or dots. The TW-SOAs in this work have a gain region composed of multiple quantum wells (MQW), the light generation details of MQW devices will be explained in more detail in the following subsections of this chapter.

Amplification in both lasers and a TW-SOA begins in the same way, by applying a forward-bias to the P-i-N junction giving rise to an inverted carrier population, essential for stimulated emission and thus amplification to take place. Laser diodes produce a coherent amplified signal through direct electrical injection without the need for injection of light from an external source. Radiative recombination of electron-hole pairs results in the emission of photons. A fraction of these photons are coupled into the waveguiding region of the device and travel along the length of the cavity stimulating the release of further photons with the same fundamental properties. The light reaches the end of the cavity where some is transmitted and the rest is reflected at the mirror-like facet, making another trip through the cavity leading to yet more stimulated recombination events, self-sustained oscillations, and lasing. Conversely, a TW-SOA employs a mechanism to greatly reduce cavity resonances and inhibit lasing. This can be achieved in different ways, as outline in Chapter 1, but the common approach is to lower the reflectivity of the mirrors present at either end of the F-P laser diode structure. The gain region can still amplify an optical signal through the same stimulated emission processes present in a laser, but now, in the absence of the mirror-like facets, there is little to no feedback of the light and therefore light from an external optical source can be amplified as it propagates along the waveguiding region, as depicted in Figure 2.1.1.
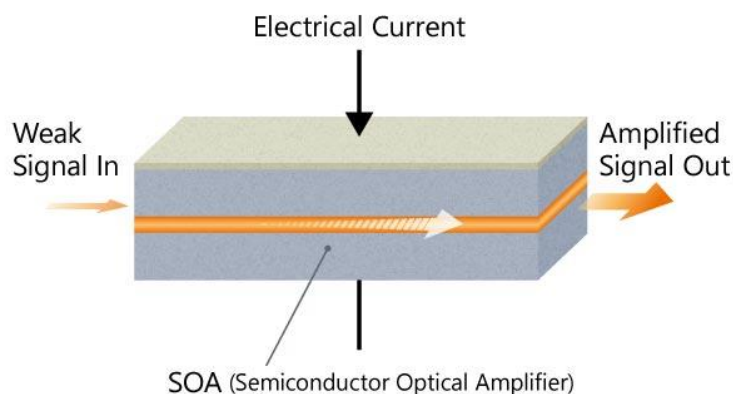
Figure 2.1.1: Semiconductor Optical Amplifier (SOA) depicting electrical/optical pumping and origin of amplified signal. **[1]**

A TW-SOA that is subject to only electrical pumping (without optical pumping) will eject photons generated via spontaneous emission events. These photons have a random energy, phase, and polarisation, but can still couple into the waveguide being amplified as they travel along the length of the cavity; this is known as Amplified Spontaneous Emission (ASE) and is described in further detail in subsection 2.3.4 If the mechanism for reducing optical feedback is not sufficient then incoming light will be coupled back into the TW-SOA cavity giving rise to unwanted resonance effects and F-P fringes across the top of the gain spectrum. If light, outside the desired wavelength range, is coupled back into the external optical pump source it will drive down the efficiency of the source by increasing its rate of amplified spontaneous emission (ASE) of photons of various energies, including those outside the frequency range of interest. This can lead to distorted signals, e.g., increasing bit-error rate, and incoherent data across a communication system, or even worse, device failure in neighbouring components within an integrated circuit.

It is somewhat challenging to design an SOA that exhibits outstanding performance for all key operating parameters. Therefore, it is necessary to consider the intended application, and tune the epitaxial material, waveguide structure, and mechanism for reducing optical feedback, to target the desired performance.

2.2 Band Structure and Carrier Dynamics in MQW TW-SOA

The process of light emission from MQW lasers and TW-SOAs begins with the realisation of a P-i-N junction, formed by stacking p and n-doped semiconductor materials around an intrinsic region, i, composed of varying semiconductor alloys. The composition, ordering, and thickness of the individual layers defines the band structure of the epitaxial stack, where the material forming the intrinsic (gain) region will have a band gap, E_g, suitable for the emission of photons with a desired wavelength. The band structure defines the number of available energy states, and how closely spaced the energy states are. This is known as the Density of States (DOS) and will differ for varying quantum confined structures. The occupation probability of the quantised energy states is described by the Fermi-Dirac distribution. The product of the DOS and Fermi-Dirac distribution describes the carrier distribution within the structure and goes some way to explaining the electrical and optical properties observed in the experimental results in Chapter 5.

2.2.1 Band Structure of AlGaInAs MQW

Figure 2.2.1 shows the simulated band diagram for the intrinsic (gain) region of the epitaxial structure used to make the TW-SOAs in this work. This epitaxial structure will be referred to as Wafer A throughout this thesis.
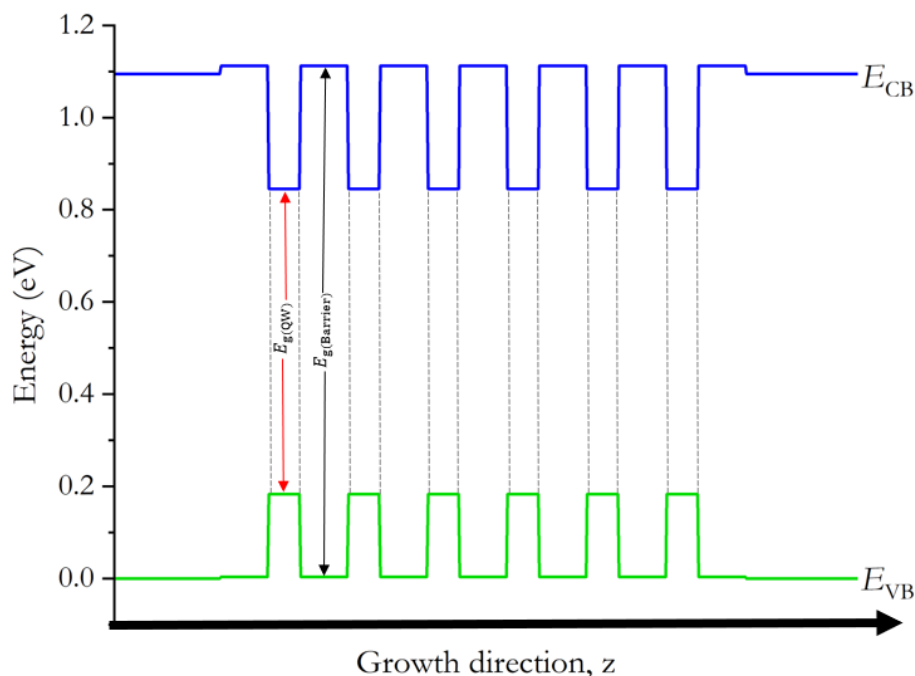
Figure 2.2.1: Simulated band diagram for the $Al_xGa_yIn_{1-x-y}As$ QW and barrier layers of the TW-SOA epitaxial structure. Blue line represents the conduction band energy, E_{CB}, and green line the valence band energy, E_{VB}. Red and black arrows indicate the energy gap, E_g, of the QW and barrier layer, respectively. Simulated using 'MQW' package in Ansys Lumerical.

Carrier confinement, holes in the valence band and electrons in the conduction band, is achieved by the construction of a potential barrier and potential well. A potential well is formed when a very narrow layer of lower energy gap material is sandwiched between two layers of thicker, wider energy gap material. Charge carriers with energy less than the depth of the potential well are unable to escape. When the width of the potential well is of the order of the de Broglie wavelength of the charge carriers, the allowed energy states the carriers can occupy become quantised and consequently, charge carriers in quantum wells are confined in one dimension, and only free to move in two dimensions, that is, perpendicular to the direction of growth. The de Broglie wavelength is given by equation (2.1)

$$\lambda_{dB} = \frac{h}{\sqrt{2mk_B T}} \qquad (2.1)$$

where h is Planck's constant, m is the mass of the particle, and k_B and T are the Boltzmann constant and temperature, respectively.

2.2.2 Carrier Confinement in Quantum Wells

The AlGaInAs quaternary alloy that forms the barrier layers of Wafer A is tuned to have a larger band gap than the AlGaInAs layers that forms the QWs. This means that the lowest energy states of the conduction and valence bands lie within the gap of the barrier layer, and therefore the electrons in the QW are trapped by the potential barriers at either side due to a discontinuity in the conduction band (CB), and the holes are trapped by the discontinuity in the valence band (VB). This gives rise to quantised carrier motion in the z-direction (direction of growth) and free carrier motion in the x and y plane of the quantum well. These quantised states in the CB and VB of the QW are characterised by their wave function, Ψ_n, and energies, E_n.

In the simplest, classical approach, the barrier is considered infinitely high and therefore carrier transport through the barrier is forbidden. However, in realistic QWs the barrier height is finite and therefore, due to quantum effects, particles can tunnel through the barrier and therefore the wave functions also spread out into the barrier, reducing the confinement energy.
Figure 2.2.2 depicts the first two energy levels and subsequent wave functions in a finite potential well of width L and depth V_0. Note how the wavefunctions spread into the barrier region, as mentioned above.
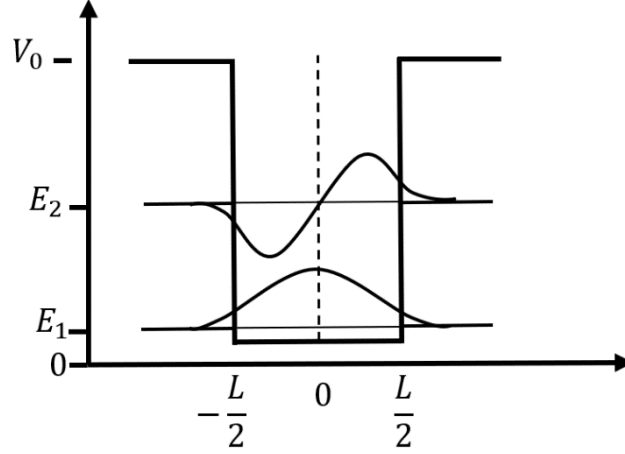
Figure 2.2.2: The finite potential well of width L and height V_0 with first two energy states E_1 and E_2 and associated wave functions.

As the potential well has a finite height, there are a finite number of bound states with $E < V_0$ that carriers can occupy. However, no matter how small V_0 is, there will always be at least one energy state present. The wavefunction and energy of the quantised states can be calculated using the time-independent Schrödinger equation, and effective mass approximation, respectively. A complete description of the associated equations and relevant solutions, both in and outside the well, can be found in many quantum mechanics textbooks. The author suggests **[2]** as a good starting point.

2.2.3 The Density of States

To understand the absorption/emission properties of the MQW TW-SOA knowledge of the inter-band transitions, within the wells, is essential. To quantify the concentration of electrons in the CB and holes in the VB, of the QW, it is necessary to calculate the density of states (DOS) for the system in question. The DOS is defined as the number of allowable states per unit energy per unit volume and will differ based on the quantum confinement of the nanostructure that makes up the intrinsic (gain) region of the device. For an TW-SOA that has a bulk active region, the carriers can move freely in all 3-dimesions, and therefore the density of states, $g(E)$, equation has the form

$$g(E)_{3\text{D}}\mathrm{d}E = \frac{1}{2\pi^2}\left(\frac{2m}{\hbar^2}\right)^{\frac{3}{2}} E^{\frac{1}{2}}\,\mathrm{d}E \qquad (2.2)$$

where m is the particle mass, $\hbar = \frac{h}{2\pi}$, and E is the energy of the state. Integrating over the different energy states gives the number of allowable states per unit volume.

Figure 2.2.3 is a schematic of the DOS function for electrons in the conduction band of a bulk TW-SOA.
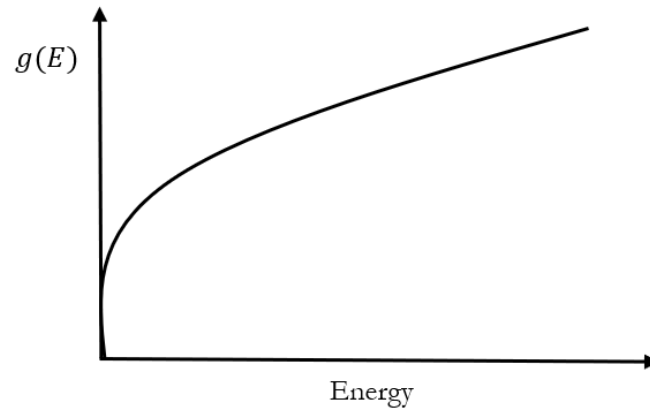
Figure 2.2.3: Schematic of DOS function for electrons in the conduction band of a bulk gain region.

However, as detailed above, the carrier confinement in a QW differs from that of bulk, and therefore the density of states function does not have the same equation or profile. As seen in Figure 2.2.4, the function now has a step-like nature, arising from the quantised energy levels from 1D confinement of electrons. Therefore, the equation for the DOS in a 2-dimentional QW is given by

$$g(E)_{2D}dE = \frac{m^*}{\pi\hbar^2} \sum_i \Theta(E - E_i) \, dE \tag{2.3}$$

where m^* is the effective mass, and $\Theta(E - E_i)$ is the unit step function that has a value of zero when $E < E_i$ and a value of one when $E \geq E_i$.
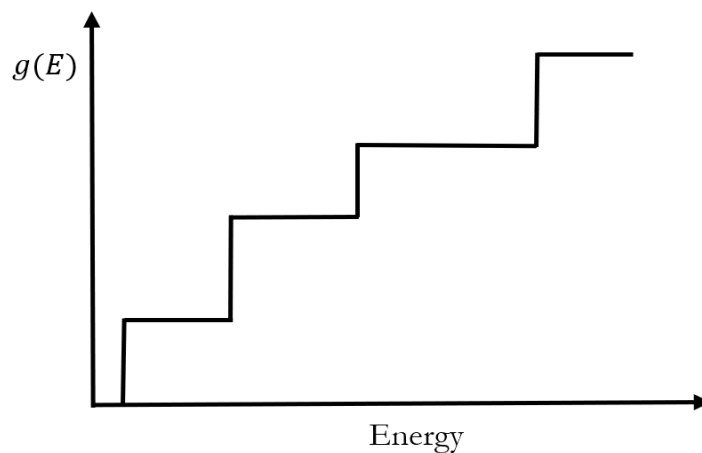
Figure 2.2.4: Schematic of DOS function for electrons in the conduction band of a QW.

2.2.3 The Fermi-Dirac Distribution

The probability distribution of energies in a quantum system is mathematically represented by the Fermi-Dirac probability function. Systems that contain more than one electron (fermion) have constraints that arise from the half-integer spin possessed by electrons. This constraint is known as the Pauli exclusion principle which states that no two fermions can have the exact same set of quantum numbers and therefore, only two electrons can occupy a single orbital – one 'spin-up' and one 'spin-down'. The distribution of electrons, that is the probability of a state at energy E being occupied, is described statistically by the Fermi-Dirac function given in equation (2.4)

$$f(E) = \frac{1}{e^{((E-\mu)/k_\mathrm{B}T)} + 1} \tag{2.4}$$

where $f(E)$ is the occupation probability of energy state E, μ is the chemical potential (which can be equated to the Fermi level for electrons), k_B is the Boltzmann constant, and T is temperature in Kelvin.

The thermodynamic properties of a system of electrons are found via equation (2.4) from knowledge of the available electron states and the number of states that have the same energy (degeneracy). When $T = 0\mathrm{K}$ (absolute zero) the value the chemical potential possesses is known as the Fermi energy. For undoped (intrinsic) semiconductors, at finite temperature, the Fermi energy lies halfway between the CB and VB.

2.2.4 Carrier Dynamics in Quantum Wells

Bringing together the information from the previous subsections gives a complete description of energy distribution of electrons in the QWs. The product of the density function, $g(E)_\mathrm{2D}$, and the occupation probability, $f(E)$, is given by equation (2.5), for a single sub-band **[3]**

$$n_a = \frac{mk_\mathrm{B}T}{\pi\hbar^2}\ln\left\{1 + \exp\left(-\frac{E_n - E_f}{k_\mathrm{B}T}\right)\right\} \tag{2.5}$$

per unit area, single sub-band. Figure 2.2.5 depicts the energy distribution of electrons in the quantum well, $n(E)$.
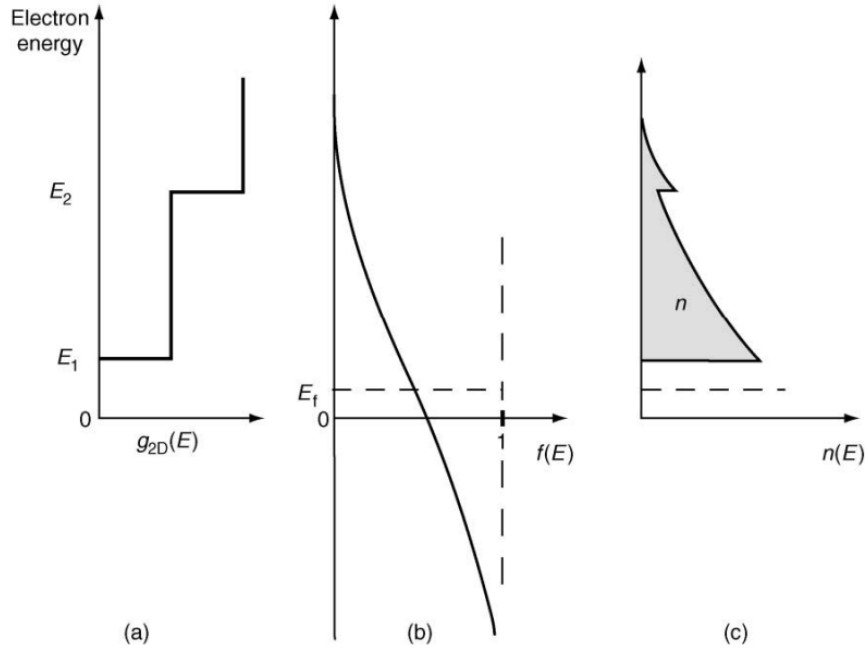
Figure 2.2.5: (a) The density of states function for a quantum well, with the value of $g(E)_{2D}$ on the horizontal axis indicating how the density of states varies with increasing electron energy. **(b)** is an illustration of the probability that a state is occupied by an electron, showing how $f(E)$ varies with increasing electron energy, given by equation (1.4). The actual density of electrons in a given energy interval at any energy $n(E)$ is given by the product of the density of available states and the probability that the state is occupied as shown in **(c).** The integral of $n(E)$ over energy gives the total density of electrons given for each sub-band by equation (2.5). **[4]**

2.2.5 The P-*i*-N Junction

The p-n junction is the at the heart of semiconductor devices, including the TW-SOA in this work. It begins with the doping of semiconductor materials to create material with altered electrical properties, such as p-type (abundance of holes) and n-type (abundance of electrons) materials. The dopants used can vary, but for Wafer A the InP is doped with zinc to produce the p-type material, and with silicon for the n-type material. The intrinsic (*i*) region remains undoped and is the region where devices experience gain under bias. Joining the p and n-type materials causes diffusion of electrons to the p-side and holes to the n-side where they recombine at the junction. Eventually a steady state is reached whereby further diffusion of charges is opposed by the built-in electric field across the junction **[5]**. In multiple quantum well devices, the junction takes the form of a double-heterojunction, as seen in Figure 2.2.6.

16
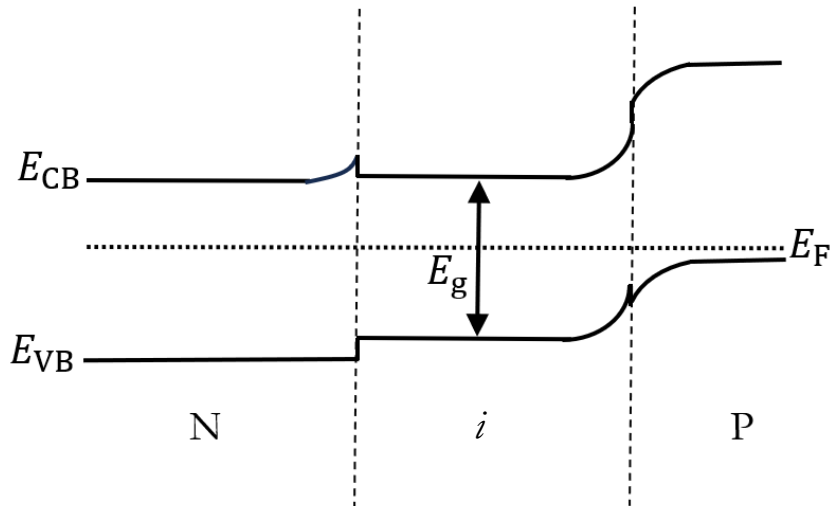
Figure 2.2.6: Energy band diagram of a double-heterojunction semiconductor TW-SOA under zero bias, that is $V = 0$.

Under zero bias, the Fermi level is constant across the whole structure and as previously stated, free carriers are excluded from either side of the junction, leaving a positive charge on the n-side, due to ionised donors, and a negative charge on the p-side due to ionised acceptors, leaving the depletion region neutral.

2.2.6 Population Inversion

For amplification to take place in the TW-SOA, the carrier population in the structure needs to be inverted. This is achieved by subjecting the junction to a forward-bias, i.e., injecting electrons into the conduction band and holes into the valence band. Figure 2.2.7 shows the double-heterostructure under forward-bias.
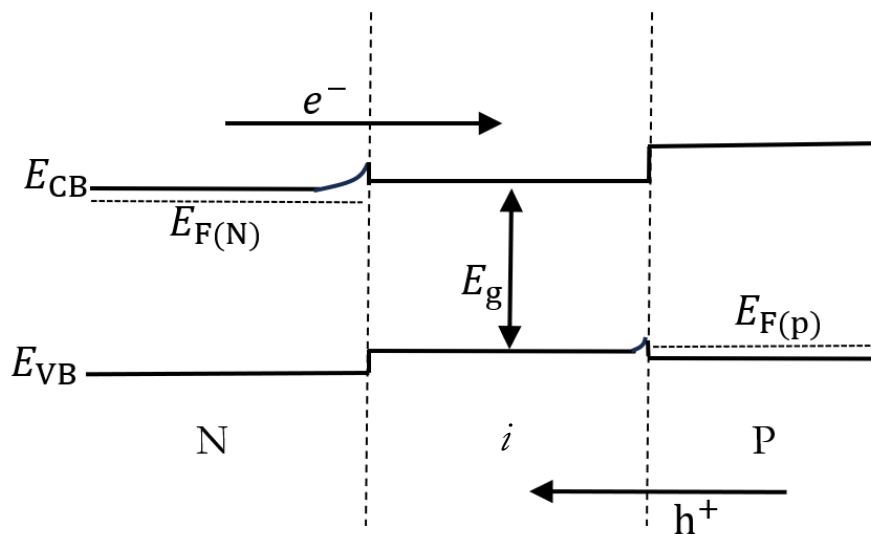
Figure 2.2.7: Energy band diagram of a double-heterojunction semiconductor TW-SOA under forward-bias, that is $V > 0$.

Electrons move freely from the n-type material, and holes from the p-type material to the active region, the narrow energy gap material, E_g. When there, further movement is restricted by the energy gap difference between narrow gap gain region, and the wider gap p and n-type cladding regions. This leads to a build-up of electrons in the conduction band, and holes in the valence band of the active (intrinsic) region of the device, where electron-hole recombination can take place via spontaneous and stimulated emission events. When the TW-SOA is optically pumped, incoming photons will stimulate the recombination of the electron-hole pairs, emitting a photon with the same optical properties as the one that stimulated its release. This process is repeated many times as the photons continue to travel the length of the cavity; amplification has been achieved.

2.3 Principles of Light Amplification

The different processes that give rise to light amplification in an SOA can be described using a simple two-level system, as shown in Figure 2.3.1. The following sections detail the three fundamental radiative processes that take place in the semiconductor gain region of an SOA, as well as describing some of the non-radiative processes that can be disruptive to the amplification process.
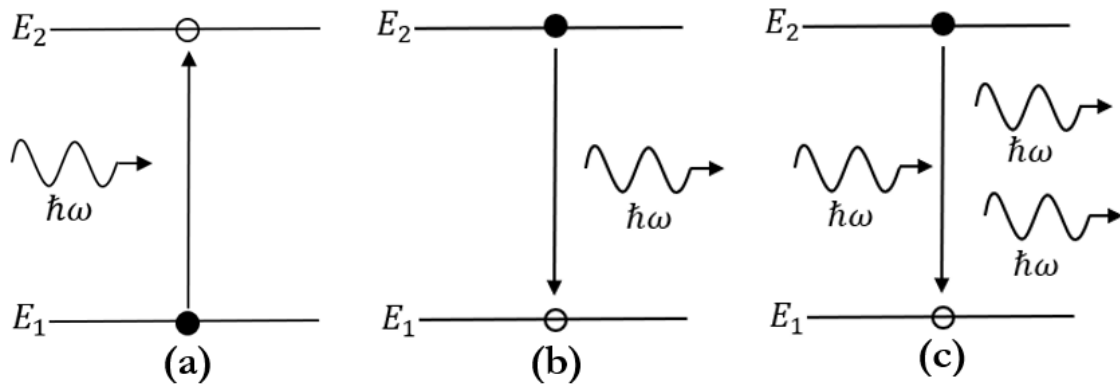
Figure 2.3.1: Radiative processes in a basic two-level system. **(a)** absorption, **(b)** spontaneous emission, and **(c)** stimulated emission.

2.3.1 Absorption

External optical pumping of an SOA can promote photon absorption within the active material of the device. If the associated energy of the incoming photon exceeds that of the band-gap energy, E_g, of the material the photon can be absorbed, and an electron will be stimulated from a lower energy level to a higher energy level in the CB whilst leaving behind a hole in the VB. This transition leaves the system in an excited state until electron-hole pairs recombine via spontaneous or stimulated events. The rate of absorption in the system is given by equation (2.6)

$$\left[\frac{dN_2}{dt}\right]_{abs} = -\left[\frac{dN_1}{dt}\right]_{abs} = B_{12}N_1\rho(f) \qquad (2.6)$$

where B_{12} is the absorption probability per unit spectral energy density, $\rho(f)$ is the average spectral density per unit frequency for blackbody radiation, and N_1 and N_2 are the carrier populations in the lower and excited energy states, respectively. Absorption is more likely to take place when the population of carriers in the lower energy state is much greater than the carrier population in the excited energy state, that is $N_1 > N_2$.

2.3.2 Spontaneous Emission

Spontaneous emission is a randomly occurring radiative process whereby an electron from the excited state, E_2, makes a downward transition to a lower energy state, E_1, thus releasing energy in the form of a photon. The photon possesses the magnitude of energy difference between the two states, $hf = E_2 - E_1$. The rate of spontaneous decay is represented by equation (2.7)

$$\left[\frac{dN_2}{dt}\right]_{sp} = -\left[\frac{dN_1}{dt}\right]_{sp} = -A_{21}N_2 \tag{2.7}$$

where A_{21} is the spontaneous emission probability, and N_1 and N_2 describe the carrier population densities in the lower and upper and energy states, respectively.

The rate of spontaneous emission is proportional to the population density of the higher energy state, N_2. In essence, as the upper energy state, E_2, becomes more populated, the greater the rate of spontaneous decay of an electron back to the lower energy state, E_1. Equation (2.8) describes the population density of the excited state, where N_2^0 is the population density of the excited state, at $t = 0$. The spontaneous emission lifetime, $\tau_{21,sp,} = \frac{1}{A_{21}}$, is the average lifetime an electron survives in the upper energy state before making a downward transition to a lower energy. The probability that a particular atom will undergo a spontaneous transition, in time dt, is $A_{21}dt$.

$$N_2 = N_2^0 \exp\left(-\frac{t}{\tau_{21,sp}}\right) \tag{2.8}$$

2.3.3 Stimulated Emission

If an incoming photon of frequency $f = \frac{(E_2 - E_1)}{h}$ interacts with an electron in a higher energy level, this triggers a radiative process where the electron loses energy and decays to a lower energy state, emitting a photon of equivalent energy. The emitted photon will have the same frequency, phase, direction, and polarisation as the photon that stimulated its release. Stimulated emission is the inverse of stimulated absorption and produces the amplification of an optical signal of a desired frequency and polarisation. The rate of stimulated emission depends on the incoming optical signal as well as the carrier population of the excited energy state and is given by equation (2.9),

$$\left[\frac{dN_2}{dt}\right]_{st} = -\left[\frac{dN_1}{dt}\right]_{st} = B_{21}N_2\rho(f) \qquad (2.9)$$

where B_{21} is the stimulated emission probability per unit time per unit spectral density.

2.3.4 Amplified Spontaneous Emission

Amplified spontaneous emission (ASE) occurs when a fraction of spontaneously emitted photons are coupled into the waveguide modes of the TW-SOA. In the absence of reflective end mirrors, the photons make a single pass along the cavity where they are amplified in the presence of an inverted carrier population before exiting the cavity at either end. The emitted light is effectively spontaneously generated photons that have been amplified by the process of stimulated emission [6].

Increased electrical pumping of the device leads to a large density of electrons in the CB which are free to occupy a range of different states available within a structure, and therefore the emitted photons have a range of different energies, giving rise to a broad ASE spectrum. The spontaneous power into the ASE modes per volume of gain medium is given by [7]

$$S(z) = F\hbar v B N(z)^2 \qquad (2.10)$$

where B is the bimolecular radiative recombination rate coefficient, N is the saturated carrier density, v is the laser frequency, and F is the fraction of spontaneous emission power contributing to the ASE modes.

ASE is problematic for TW-SOA's, particularly those with high gain, since it lowers the electron density in the CB leaving less carriers available for amplifying the external optical pump source.

2.3.5 Non-Radiative Processes

In addition to desirable radiative (photon producing) processes that take place within the TW-SOA gain medium, there are also less desirable non-radiative (non-photon producing) processes. Semiconductor epitaxial structures can possess imperfections throughout the crystal lattice, known as defect states which usually occur during the material growth and processing phases. Certain material combinations have a greater lattice mismatch than others, causing difficulties during the growth of the epitaxial layers onto the chosen substrate. These mismatches produce unwanted point defects which travel throughout the structure giving rise to various types of

dislocations **[8]**. The presence of defect states can cause "traps" within the material which form sites for unwanted non-radiative processes to take place. An example of such non-radiative transitions is Shockley-Read-Hall (SRH) recombination. SRH recombination occurs when an electron (e^-) and hole (h^+) recombine within a "trap" and release a phonon (lattice vibrational energy) instead of a photon. Such processes are problematic in functioning SOA devices, as they increase losses due to the generation of heat within the crystal lattice which ultimately leads to decreased photon generation efficiency and consequently less amplified light.

Other forms of non-radiative recombination can occur in semiconductor structures such as Auger recombination. Here, the excess energy from electron-hole recombination is transferred to an electron or hole that are subsequently excited to a higher energy level within the same band, rather than releasing the energy as a photon. Auger recombination is particularly important in devices that have a high carrier density since the rate of recombination is proportional to the cube of the carrier density.

2.4 Fabry-Pérot Laser Diode to TW-SOA

To begin, we examine the equations necessary to model the amplification of optical signals in an FP laser diode with two partially reflective mirrors ($\sim 30\%$) at either end of the cavity. Modifications to the equations are suggested to account for the unknown values of R_1 and R_2 after an antireflection coating is applied to both facets of the device to create a TW-SOA, followed by details of extracting the coated facet reflectivity from the depth of the remaining ripples in the measured gain spectrum of the TW-SOA.

Figure 2.4.1 shows the layout of a cleaved facet RWG laser diode optical cavity used as the basis for the TW-SOA. The planar waveguiding region has a length L_c which is bounded by two uncoated mirrors of reflectivity R_1 and R_2.
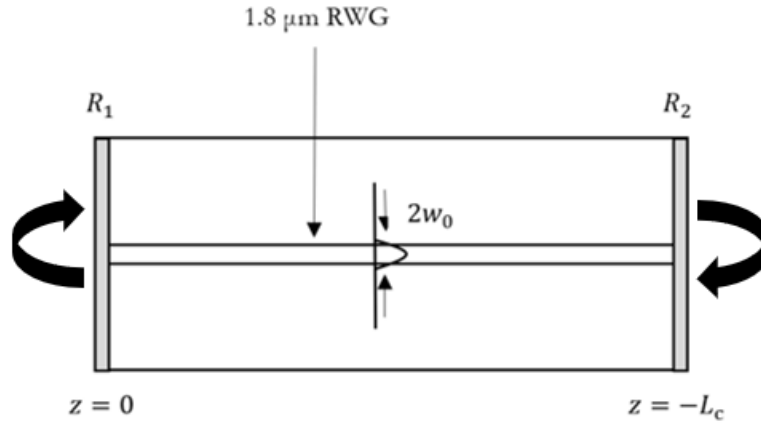
Figure 2.4.1: RWG Laser diode with uncoated mirrors R_1 and R_2

As described in **[9]** when an optical field $E(0)$ travels from $z = 0$ to $z = -L$ it experiences a logarithmic power gain, G_- and when travelling in the opposite direction, from $z = -L$ to $z = 0$ the gain is represented by G_+. When both facets are uncoated, the reflectivity of each mirror is $R_1 = R_2 = R_l$, where R_l denotes the reflectivity of the original laser before coating. Assuming $R_1 = R_2$ the overall laser gain, G_l is represented by equation (2.11)

$$G_+ = G_- = G_l \tag{2.11}$$

and after N complete roundtrips, the field has the value

$$E'(0) = E(0) \sum_0^N a^n = E(0)(1-a)^{-1} \tag{2.12}$$

where $N \to \infty$ and the roundtrip amplification factor is

$$a = R_l e^{2j\beta L} e^{G_l} \tag{2.13}$$

where $2\beta L$ is the roundtrip phase shift, $|a| \ll 1$ to conserve energy, and at laser threshold $a \approx 1$.

As outlined in subsection 2.3, initially, photons are emitted via spontaneous carrier recombination in the active region of the device. A fraction of these photons will be coupled into the waveguide mode, being amplified (via stimulated emission) as they propagate along the length of the cavity. Some of the light will exit the waveguide and some will be reflected by the mirrors at either end of the structure. The reflected light will make a number of trips along the cavity, stimulating the transition of excited electrons to lower energy states, and thus emission of further photons will the same properties, e.g.., energy. After several trips around the cavity, the amplified light becomes coherent along the length of the waveguide and the light emitted immediately after the facet is both intense and focussed – lasing has commenced. To achieve single pass amplification, where light travels along the cavity just once, optical feedback must be suppressed, and lasing inhibited. One approach to this, is to apply an antireflective thin film to either end of the FP laser diode to create a TW-SOA. In an *ideal* SOA $\sqrt{R_1 R_2} = 0$, however this is incredibly challenging to achieve, and therefore some feedback may still be present. The reflectivity of each facet is no longer equal to the reflectivity of the uncoated laser diode facets, that is $\sqrt{R_1 R_2} \neq R_l$. Therefore, equation (2.13) becomes

$$a = \sqrt{R_1 R_2}\, e^{2j\beta L} e^{\frac{1}{2}(G_+ + G_+)} \tag{2.14}$$

The total output power of the spectrum of the device is given by

$$P(\lambda) = P_z(1 - R_1)|1 - a|^{-2} \tag{2.15}$$

where P_z is the integrated initial spontaneous emission power and $(1 - R_1)|E(0)|^2|1 - a|^{-2}$ is due to the power transmitted through the mirror at $z = 0$ due to initial spontaneous emission at this mirror [10]. The spectrum of a non-ideal TW-SOA, $(\sqrt{R_1 R_2} \neq 0)$ comprises of the photons emitted from the gain medium that have been modulated by remaining cavity resonance. Therefore, FP fringes are still present across the top of the spectrum, and their depth can be represented by equation (2.16)

$$m = \frac{P_{\max} - P_{\min}}{P_{\max} + P_{\min}} \tag{2.16}$$

where the values $P_{\max}$ and $P_{\min}$ are taken from the maximum and minimum points of the modulated signal. Bringing together equation (2.14), (2.15), and (2.16) we form an equation for the modulation index in terms of the round-trip amplification of the TW-SOA, namely equation (2.17)

$$m = \frac{2|a|}{1 + |a|^2} \tag{2.17}$$

where for an ideal laser, $m = 1$ and for an ideal TW-SOA $m = 0$. The derivation of equation (2.17) can be found in Appendix A of this thesis.

For a device that has both facets coated, as seen in Figure 2.4.2, if gain saturation is negligible (at $I = I_{th}$) for both the original laser and TW-SOA, and $a = 1$ for the original laser, then the reflectivity of the coated facets is given by

$$\sqrt{R_1 R_2} = |a| R_l \tag{2.18}$$

where $|a|$ is measured at the original threshold current of the uncoated laser, $I = I_{th}$.
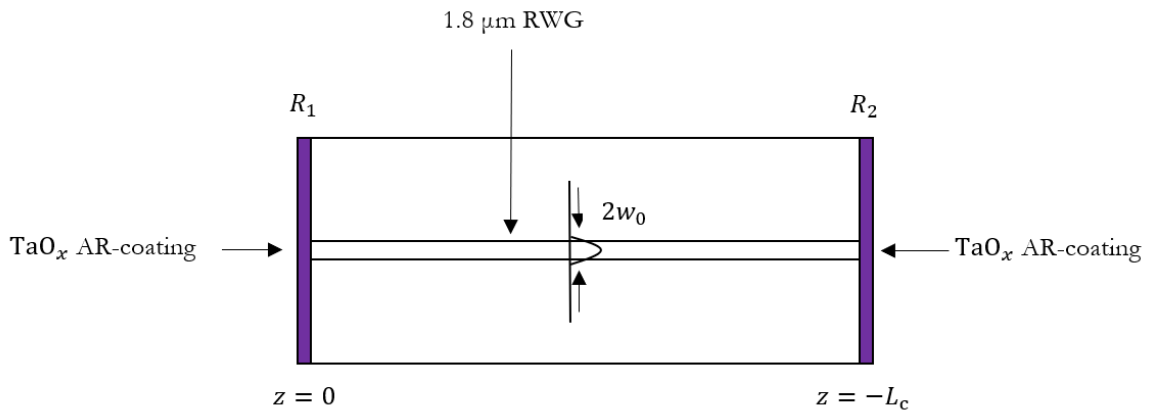
Figure 2.4.2: TW-SOA with mirrors R_1 and R_2 coated with a single layer antireflective thin film.

If the reflectivity of each facet is of order 10^{-4} to 10^{-5}-, at $I \leq I_{th}$, the F-P fringes can be small and hard to distinguish in the presence of noise. Therefore, if we take the net gain as a linear function of injection current, we get

$$\frac{G_+ + G_-}{2} = \left(\gamma \frac{I}{I_{\text{th}}} - \alpha\right) L_{\text{c}} \tag{2.19}$$

where γ is the power gain coefficient at $I = I_{\text{th}}$ and α is the power loss coefficient.

The threshold gain of the original laser is given by

$$G_l = (\gamma - \alpha) L_{\text{c}} \tag{2.20}$$

where $\alpha = \frac{1}{L_{\text{c}}} \ln\left(\frac{1}{\sqrt{R_1 R_2}}\right)$ and with equations (2.13), (2.14), and (2.19) yields

$$\ln|a| = (\gamma L_{\text{c}}) \frac{I}{I_{\text{th}}} - \left(\gamma L_{\text{c}} - \ln \frac{\sqrt{R_1 R_2}}{R_l}\right) \tag{2.21}$$

When R_l and I_{th} are known for the original uncoated laser, values of m and a can be found by measuring the ASE of the coated TW-SOA as a function of injection current. A plot of $\ln|a|$ versus normalised current, $\frac{I}{I_{\text{th}}}$, can be constructed, and using equation (2.21) the coated facet reflectivity for the TW-SOA, $\sqrt{R_1 R_2}$, can be deduced from fitting the linear region of the graph, where gain saturation is negligible, and extracting $\ln|a|$ the point where $\frac{I}{I_{\text{th}}} = 0$. The use of this technique is demonstrated in Chapter 5 of this thesis.

2.5 Dielectrics for Thin Film Coatings

Dielectric materials come in many different variations, such as metal-oxides (Ta_2O_5), metal-fluorides (MgF_2), or even metal-sulphides (ZnS). They've gained much interest over the decades for their use as optical filters and coatings, since their unique properties give rise to interference effects necessary for reducing the reflectivity of a wide variety of surfaces. Due to their large band gap energy dielectrics exhibit low absorption and high transparency over a wide range of wavelengths, as well as their excellent resistance to most environmental influences, make dielectrics materials an attractive choice as antireflective thin films for optoelectronic devices.

2.5.1 Optical Properties of Dielectrics

Dielectric materials can be described in terms of their complex refractive index, $\tilde{n}$, as shown in equation (2.22),

$$\tilde{n} = n + ik \tag{2.22}$$

The real part of the refractive index, $n = \frac{c}{v}$ describes the propagation of light through the medium, where c is the velocity of light in free space, and v is the velocity of light in the medium. The imaginary part, k, is known as the extinction coefficient, and is related to the absorption, α, of the material by equation (2.23),

$$\alpha = \frac{4\pi k}{\lambda} \tag{2.23}$$

where λ is the wavelength of light in a vacuum. When light, of a given wavelength, travels through materials with varying values of $\tilde{n}$ it undergoes refraction at the boundary between the two materials. If k is large for one/both materials (at that λ) then some of the light will be absorbed, but if k is very small, then absorption is regarded as negligible and the material is deemed transparent at that wavelength, and therefore a portion of the light will travel through the material. Light can also be reflected at the boundary between one medium and another, due to the contrast in refractive index of medium one, n_1, and medium two, n_2. The reflection coefficient, R, is given by equation (2.24) and assumes that k is negligible, for light is at normal incidence **[11]**

$$R = \left| \frac{n_1 - n_2}{n_1 + n_2} \right|^2 \tag{2.24}$$

2.6 Thin film Interference Effects

To design anti-reflective thin films with a reflectivity $R \cong 0$ the film must be as close to the ideal refractive index, n_{film}, and thickness, d, to give rise to the desired interference effects, and thus cancellation of reflected light over the wavelength region of interest. To find the ideal values of n_{film} and d the origin of thin film interference effects must be understood, which, more precisely, relates to the interactions between the electromagnetic (EM) radiation and material under consideration. To do this we begin with Maxwell's equations, a set of four equations that describe the behaviour of EM fields in different media,

$$\nabla \cdot \boldsymbol{D} = \rho \tag{2.25}$$

$$\nabla \cdot \boldsymbol{B} = 0 \tag{2.26}$$

$$\nabla \times \boldsymbol{E} = -\frac{\partial \boldsymbol{B}}{\partial t} \tag{2.27}$$

$$\nabla \times \boldsymbol{H} = \boldsymbol{J} + \frac{\partial \boldsymbol{D}}{\partial t} \tag{2.28}$$

where $\boldsymbol{D}$ and $\boldsymbol{B}$ are the electric and magnetic flux densities; $\boldsymbol{E}$ and $\boldsymbol{H}$ are the electric and magnetic field intensities, and ρ and $\boldsymbol{J}$ are the volume charge density, and electric current density, respectively.

We examine the case for a dielectric thin film where there is no volume distribution of charge (isotropic) and therefore, $\rho = 0$, and there are no outermost valence electrons and therefore no flow of current, that is, the current density, $\boldsymbol{J}$, is also zero. The constitutive relations for such a medium link $\boldsymbol{D}$ and $\boldsymbol{B}$ to $\boldsymbol{E}$ and $\boldsymbol{H}$ via equations (2.29) and (2.30) shown below,

$$\boldsymbol{D} = \epsilon \boldsymbol{E} \tag{2.29}$$

$$\boldsymbol{B} = \mu \boldsymbol{H} \tag{2.30}$$

where ϵ and μ the permittivity and permeability of the medium.
Substituting these values into equations (2.25) to (2.28) yields Maxwell's equations for EM fields propagating in a dielectric material

$$\nabla \cdot \boldsymbol{E} = 0 \tag{2.31}$$

$$\nabla \cdot \boldsymbol{B} = 0 \tag{2.32}$$

$$\nabla \times \boldsymbol{E} = -\frac{\partial \boldsymbol{B}}{\partial t} \tag{2.33}$$

$$\nabla \times \boldsymbol{B} = \mu\epsilon \frac{\partial \boldsymbol{E}}{\partial t} \tag{2.34}$$

where $\mu = {}^n/_c$, $\epsilon = {}^1/_{nc}$ and $c = {}^1/_{\sqrt{\mu\epsilon}}$.

Figure 2.6.1. depicts a monochromatic planewave propagating in an isotropic, homogenous dielectric. The electric field is linearly polarised in the x-direction and propagating in the z-direction.
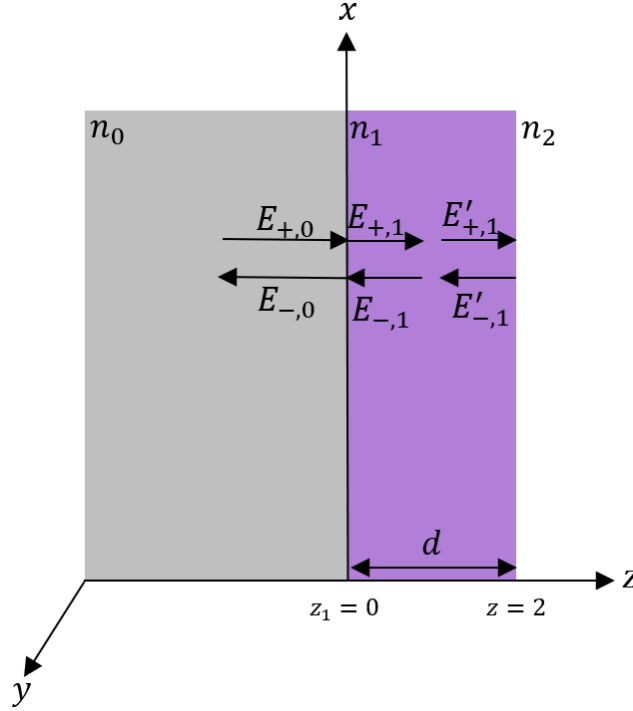
Figures 2.6.1: Thin film interference effects for a single layer coating on a laser diode facet.

The forward, E_+, and backward, E_-, propagating waves, seen in the figure above, can be described via time-varying field equations. In medium 0 the non-zero components of electric field E_x and magnetic field B_y have the following form **[12]**

$$E_0(\mathbf{x}, t) = \left[E_{+,0}e^{ikz} + E_{-,0}e^{-ikz}\right]e^{-i\omega t} \tag{2.35}$$

$$B_0(\mathbf{y}, t) = \left[\frac{n_0 E_{+,0}}{c}e^{ikz} + \frac{n_0 E_{-,0}}{c}e^{-ikz}\right]e^{-i\omega t} \tag{2.36}$$

where $k = {}^{2\pi}/_\lambda = {}^\omega/_v = {}^n/_c$ is the amplitude of the wavevector and λ is the wavelength inside the medium, and ω is the angular frequency. Similar expressions can be found for the EM fields in medium 1.

As light propagates from medium 0, to medium 1, some light is transmitted through medium 1 and some is reflected at the boundary 0-1. The transmitted light will propagate through medium 1 until it reaches the boundary between medium 1 and 2 where, once again some of the light is transmitted through to medium 2 and some is reflected at the boundary 1-2. This can be described in the form of a matrix by taking into consideration the continuity of E and B at the first interface z_1 we find [13]

$$\begin{pmatrix} E_+ \\ E_- \end{pmatrix} = \frac{1}{\tau} \begin{pmatrix} 1 & r \\ r & 1 \end{pmatrix} \begin{pmatrix} E'_+ \\ E'_- \end{pmatrix} \tag{2.37}$$

where the *amplitude* of light transmitted and reflected can be described by equations (2.38) and (2.39) [14]. The reflection coefficient ρ is replaced with r to eliminate confusion with the use of ρ for the charge density.

$$r = \frac{n_0 - n_1}{n_0 + n_1} \tag{2.38}$$

$$\tau = \frac{2n_0}{n_0 + n_1} \tag{2.39}$$

Examining equations (2.38) and (2.39) we see that when $n_0 > n_1$ then r there will be positive but when $n_0 < n_1$ the value of r will become negative, which corresponds to a phase shift of the reflected beam.

The *intensity* of light reflected and transmitted, across the interfaces for a wave travelling from left to right in Figure 2.6.1 is given by equation (2.40) and (2.41)

$$R = \frac{|E_r|^2}{|E_i|^2} \tag{2.40}$$

$$T = \frac{\text{Re}|E_t|^2}{\text{Re}|E_i|^2} \tag{2.41}$$

where $E_r = E_{-,0}$, $E_i = E_{+,0}$, and $E_t = E'_{+,1}$.

For the case of the single layer antireflective thin film depicted in Figure 2.6.1, the reflected power for the coated surface is given by equation (2.42)

$$R = \frac{r_{01} + r_{12} + 2r_{01}r_{12}\cos(2\varphi)}{1 + r_{01}r_{12} + 2r_{01}r_{12}\cos(2\varphi)} \tag{2.42}$$

$$r_{01} = \frac{n_1 - n_0}{n_1 + n_0} \tag{2.43}$$

$$r_{12} = \frac{n_2 - n_1}{n_2 + n_1} \tag{2.44}$$

$$\varphi = \frac{2\pi n_1 d}{\lambda} \tag{2.45}$$

where r_{01} and r_{12} are the amplitude reflectivity's for facet/film and film/air interfaces, respectively, and φ is the phase difference between the light reflected at the two boundaries.

To ensure complete destructive interference between the waves reflected at the front and back surfaces of the thin film, the waves need to be out of phase by π (180°). Setting $\varphi = \pi$ into (2.45) we see that this occurs when the film has an optical thickness of $\frac{\lambda}{4}$, that is a physical film thickness of

$$d = \frac{\lambda}{4n_1}; \ \frac{3\lambda}{4n_1} \ ; \ \frac{5\lambda}{4n_1}, \ ... \tag{2.46}$$

where λ is the wavelength of light incident on the film. If the film is insufficiently thick, for the wavelength of interest, then the dephasing of the of the beam, as it travel through the film, will not be "complete" thereby, when light is reflected at the front surface of the film, it will not be a full 180° out of phase with the light reflected at the back surface, resulting in only partial cancellation of these waves, and thus a higher value of R.

When $d = \frac{\lambda}{4n_1}$, R becomes a minimum, that is

$$R = \left(\frac{n_0 n_2 - n_1^2}{n_0 n_1 + n_1^2} \right)^2 \tag{2.47}$$

Therefore, for $R = 0$ we require that the refractive index of the film be equal to equation (2.48)

$$n_1 = \sqrt{n_0 n_2} \tag{2.48}$$

Chapter 2 References

[1] Anritsu, Optical Devices for Communication, SOA (Semiconductor Optical Amplifier), https://www.anritsu.com/en-au/sensing-devices/products/soa, accessed on 12/05/2020.

[2] M. Fox, "Optical Properties of Solids," Oxford Uni. Press. pp. 144-151, 2010.

[3] P. Blood, "Quantum Wells and GaAs-Based Structures", Encyclopedia of Modern Optics, pp. 13, 2005.

[4] P. Blood, "Quantum Wells and GaAs-Based Structures", Encyclopedia of Modern Optics, pp. 14, 2005.

[5] G. P. Agrawal and N. K. Dutta, "Semicondcutor Lasers", Second edition, ITP Publishing, pg. 9, 1993.

[6] P.Blood, "Quantum Confined Laser Devices", Oxford Uni. Press, pg. 51, 2015.

[7] W. W. Chow and R. R. Craig, "Amplified spontaneous emission effects in semiconductor laser amplifiers," in *IEEE Journal of Quantum Electronics*, vol. 26, no. 8, pp. 1363-1368, Aug. 1990, doi: 10.1109/3.59683.

[8] H. Ghafouri Shiraz, "Fundamentals of Laser Diode Amplifiers", John Wiley & Sons, pg. 39, 1996.

[9] I. Kaminow, G. Eisenstein and L. Stulz, "Measurement of the modal reflectivity of an antireflection coating on a superluminescent diode," in *IEEE Journal of Quantum Electronics*, vol. 19, no. 4, pp. 493-495, April 1983, doi: 10.1109/JQE.1983.1071887.

[10] B. W. Hakki and T. L. Paoli, "CW degradation at 300°K of GaAs double-heterostructure junction lasers-11: Electronic gain," J. Appl. Phys., Vol. 44, pp. 4113-4119, 1973.

[11] M. Fox, "Optical Properties of Solids," Oxford Uni. Press. pg. 7, 2010.

[12] R. Maulini, "Broadly tunable mid-infrared quantum cascade lasers for spectroscopic applications", PhD Thesis, Universit´e de Neuchˆatel, pg 55, 2006.

[13] S. J. Orfandis, "Electromagnetic Waves and Antennas", Department of Electrical & Computer Engineering, Rutgers University, Piscataway, pg 157, 2016.

[14] H. A. Macleod, "Thin Film Optical Filters, Fourth Edition", CRC Press, Taylor & Francis Group, pg. 22, 2010.

Chapter 3
Modelling and Simulations

The following chapter outlines the modelling and simulation work undertaken to realise a sufficiently confined single (lateral) mode AlGaInAs/InP MQW TW-SOA with competitively low facet reflectivity.

Section 3.1 gives details of the epitaxial wafer used to fabricate the TW-SOA structures. Section 3.2 describes the rationale for choosing different ridge designs for the optical waveguide of the device. Section 3.3 outlines the simulation work carried to find waveguide dimensions that are suitable for the propagation of a well confined single optical mode within the cavity of the device. Section 3.4 presents a model for TW-SOA facet reflectivity as a function of single pass gain, G_s, and gain ripple, G_r. Section 3.5 details the modelling and simulation work carried out to design and optimise a single layer TaO_x anti-reflective thin film that can be used to coat both facets of the amplifier. To realise the TW-SOA, the design stage focusses on two key areas: the waveguide geometry of the device, and mechanisms for suppressing cavity resonances. To support a single (lateral) mode that is well confined in the active medium of the device, different waveguide structures are explored using Lumerical simulation software. The same software is used to design a single-layer antireflection thin film that can be applied to both facets of the structure to reduce roundtrip amplification that gives rise to lasing.

3.1 Material Structure

The MQW epitaxial structure detailed in this report was grown via Metalorganic Chemical Vapour Deposition (MOCVD) on an n-type InP substrate. The layer compositions are detailed in Figure 3.1.1, and will subsequently be referred to as Wafer A. The material has an active medium containing six QWs with surrounding barrier layers composed of $Al_xGa_yIn_{1-x-y}As$. The aluminium and indium fractions within the active layers meet the bandgap requirements for emission in the 1550 nm region. The difference in chemical composition between the active and cladding regions of the structure provide the necessary energy difference for increased carrier confinement within in the QW and reduced carrier leakage into the surrounding cladding layers. The refractive index step between the active and cladding layers serves to increase optical confinement within the gain (higher index) region and reduce optical losses from modes spreading into the surrounding cladding regions (lower index). The aluminium containing material system chosen for this work provides light emission in the required C-Band region and

33

has shown good temperature stability and reduced carrier leakage from the active region due to its larger conduction band offset ($\Delta Ec = 0.72\Delta Eg$) compared to the more conventional GaInAsP/InP ($\Delta Ec = 0.40\Delta Eg$) structures used in producing SOAs within the data communications frequency range [1-2].
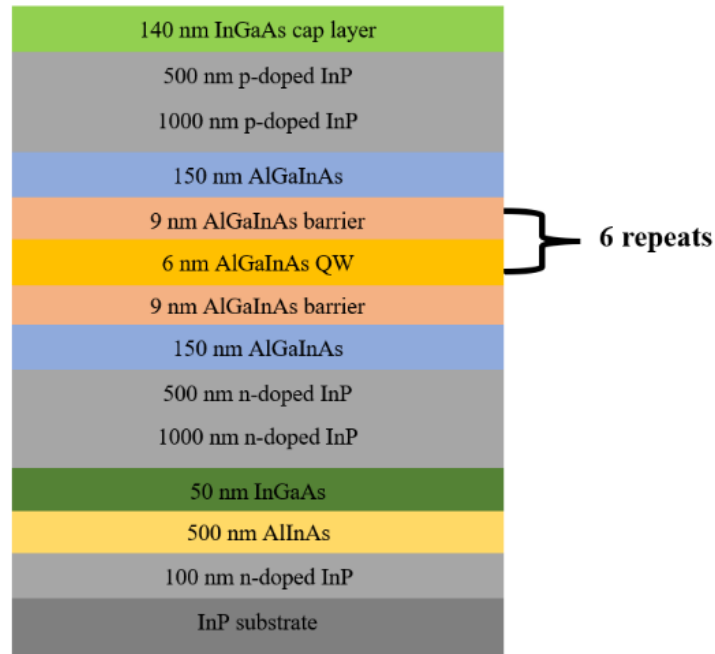
Figures 3.1.1: Wafer A - 6QW AlGaInAs/InP epitaxial structure used in this work.

The surrounding 150 nm AlGaInAs cladding layers, either side of the barrier layers, form part of the separate confinement heterostructure (SCH) used to reduce electron tunnelling from the QW/barrier layers. It is vitally important to keep the electrons in the desired active region of the structure for increased radiative electron-hole recombination events, which is key to improved device performance. The 1.5 μm thick p-type and n-type (doped) InP layers surrounding the AlGaInAs cladding layers form the p-n junction of the device. These layers are necessary for the effective injection of electrons (and subsequently holes) into the structure when under bias. The lower bandgap 140 nm InGaAs capping layer is placed at the top of the structure to facilitate the formation of an ohmic metal contact. The epitaxial structure used in this work was intended for more than one project, and therefore a 500 nm AlInAs layer is grown at the bottom of the stack as a sacrificial etch layer. An explanation of the necessity and importance of this layer is beyond the scope of the work outlined in this thesis.

3.2 Waveguide Geometry

For sufficient amplification of incoming optical signals, every effort must be made to ensure that light is well confined and guided within the active (amplifying region) as it propagates through the structure. Insufficient confinement and guiding leads to incident photons being "lost" to the surrounding cladding layers through mechanisms such as absorption and scattering, leading to a low photon density within the QW region of the device. A lower fraction of photons within the active region leads to less stimulated electron-hole recombination events thus less amplified light exiting the cavity. Additionally, single mode SOAs are desirable for the efficient coupling of light between the input/output facet(s) and single mode optical fibres, typically used in data transmission systems, or coupling between single mode components in Photonic Integrated Circuit (PIC).

To understand how waveguides of varying geometry effect the confinement within the cavity it is sufficient to treat the optical signal as an electromagnetic (EM) wave by simulating the EM field distribution inside the waveguide, which in-turn allows the photon density in the cavity to be inferred. The subsequent modelling work aims to find a waveguide cross-section that supports only a single lateral mode, namely the fundamental Transverse-Electric (TE) and Transverse-Magnetic (TM) modes, for a given frequency range, but also to ensure there is sufficient overlap between the mode and the active region. Typically, both criteria can be met by reducing the cross-section of the waveguide so that the unwanted higher order modes are "cut-off" – they are not confined within the region of interest.

A ridge waveguide (RWG) structure was chosen for the TW-SOA where single mode (SM) amplification can be obtained unlike in broad-area devices, such as oxide-isolated stripe lasers, which are inherently multimode (MM). The width of the waveguide needs to be narrow enough to support only the fundamental mode, but wide enough to avoid the large non-radiative losses associated with very narrow and deeply etched waveguides that are etched beyond the active layers, typically down to the substrate. RWGs with different etch depths have advantages and disadvantages which can have an impact on how efficiently the TW-SOA will amplify optical signals under forward-bias. Therefore, two different etch depths are chosen for the test structures - a shallow-etch (above the active region) and a deep-etch (below the active region). Figures 3.2.2(a) and 3.2.2(b) show the targeted etch-depth stop points for Wafer A.
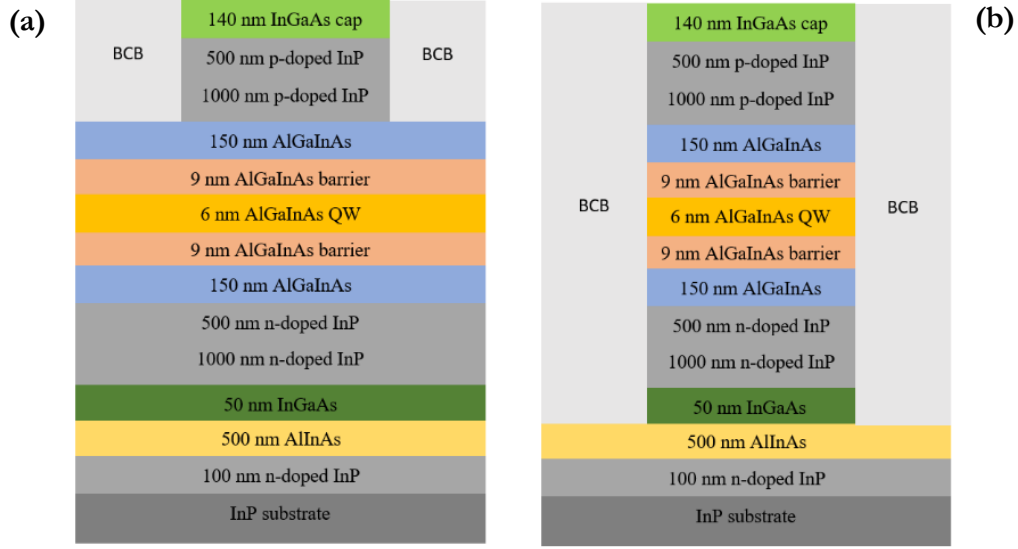
Figures 3.2.2: (a) Shallow-etch stop point and **(b)** deep-etch stop point. The ridges are surrounded by an isolation layer of benzocyclobutene (BCB).

3.3 FDE Mode Simulations

A Finite Difference Eigenmode (FDE) solver, as part of the (Ansys) Lumerical simulation software, is used to probe the mode characteristics of RWG structures of varying geometry, constructed from Wafer A. Photonic device simulations suites, such as the one used in this work, are useful tools for extracting information about the supported modes within the optical waveguide, thus allowing us to draw conclusions about the photon density within the active region of the device. The FDE solver calculates the spatial profile and frequency dependence of the supported modes by solving Maxwell's equations on a cross-sectional mesh of the waveguide. The solver calculates the mode field profiles, effective indices, and mode losses associated with each waveguide structure, as well as using integrated frequency sweeps to calculate the group delay and dispersive effects within the epitaxial layers **[3].** Using the GUI in the FDE solver, each layer of the structure is built, and the shape parameters modified to reflect the thicknesses and refractive indices of each layer **[4]**. The final structure is meshed so that it is fine enough in the y-direction (layer thickness) to match the thinnest quantum well and barrier layers of the structure, but coarser in the x-direction where the smallest feature size is greater than 1 μm. Adequate meshing is important for the mode solver, as it needs to be fine enough to resolve the modes, but not too fine that the simulation time and memory is too large to run. The FDE solver makes a cross-sectional cut though the centre of the structure in the z-direction - direction of propagation. Parameter sweeps are carried out to identify a reasonable x-span for the solver region, taking the metal boundary conditions into consideration. If the separation between the RWG structure and the metal boundaries is not great enough, then scattered fields

can couple into artificial modes created at the metal boundary which are in-turn detected by the solver and can compromise the s-matrix results obtained from the solver. Initial parameter sweeps are important to ensure that small changes in solver geometry do not have an appreciable impact on the calculated mode parameters, and therefore values obtained by the solver are reliable and not just artifacts of the simulation setup. The background refractive index, $n_{\text{background}}$, of the solver is set to 1.54 which is the refractive index of benzocyclobutene (BCB) at 1550 nm. This is the dielectric material to be used as the electrical isolation layer surrounding the RWG. Figure 3.3.1 depicts the layout of the structure in the simulation software, including the positioning of the mesh and solver.
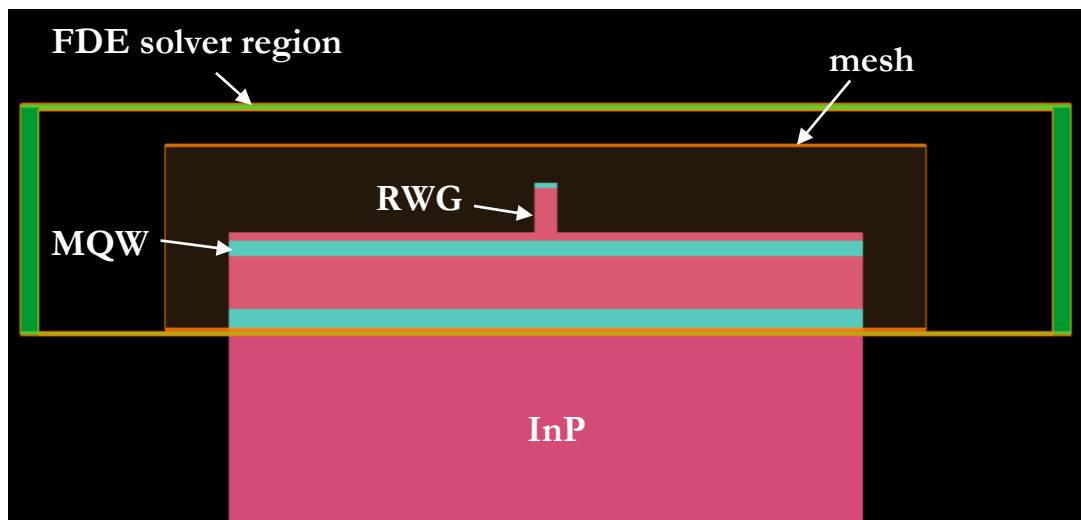
Figures 3.3.1 FDE simulation layout for 1.8 μm shallow-etched RWG. Pink layers are InP.

The solver is set to calculate the first 100 modes near the active layers of the structure by specifying the refractive index and wavelength (1550 nm) of interest. If the specified number of modes to be found is too small, then there is a risk that the solver will miss some. Setting this number to a 100 should ensure that all physical modes, near the refractive index of interest, are detected. The effective indices and spatial profiles of the detected modes are of most interest, since it is these parameters that gives some indication to which modes are bound and guided, and whether higher order TE modes significantly overlap with the gain region of the structure. If the effective index of the mode is higher than the refractive index of the cladding layers, but lower than the refractive index of the MQW layers, then the mode is tracked. The percentage overlap between the selected mode and the active layers is calculated to determine how well the fundamental mode is confined to the gain region and whether the ridge dimensions are sufficient for supporting *only* the fundamental TE mode or if higher order modes are also supported. This procedure is repeated for the two different etch-depths and ridge widths spanning 1.6-3.0 μm in

0.2 µm increments. The mode profiles for the calculated TE_1, TM_1, and TE_2 modes at 1550 nm, for the various waveguide geometries, can be seen in Appendix B at the end of this thesis. Figures 3.3.2(a) and 3.3.2(b) summarise the results calculated by the FDE solver, indicating the percentage of the fundamental mode, TE_1, that is confined to the amplifying region, as well as the confinement of the higher order TE_2 mode giving an indication at which widths and heights the RWG supports on a single (lateral) mode.
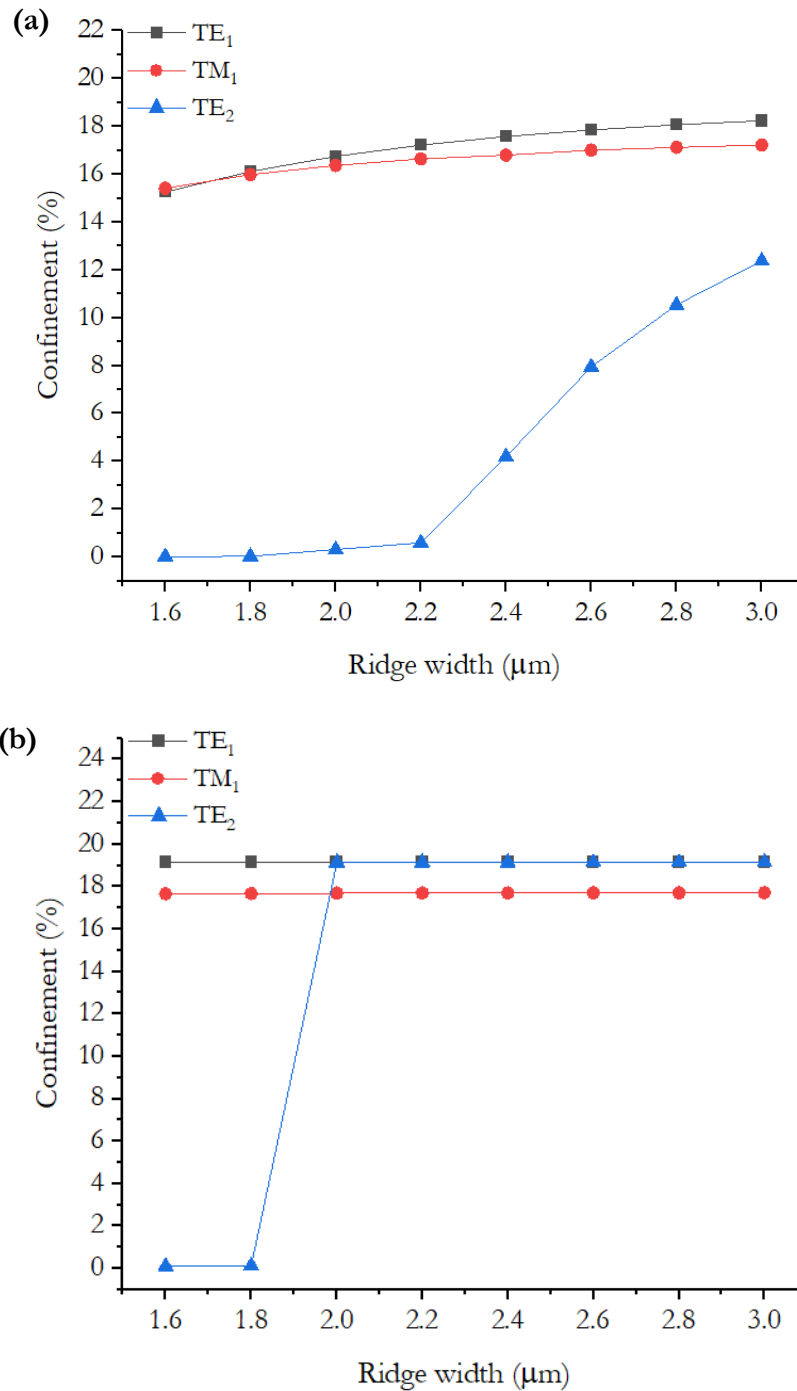
Figures 3.3.2: Confinement of fundamental and higher order modes for varying RWG widths and heights. **(a)** shallow-etch waveguide and **(b)** deep-etch waveguide.

Figure 3.3.2(a) shows the simulated data for the shallow-etched ridges, where, for ridge widths 2.2 µm and below, the fundamental TE_1 and TM_1 modes have very similar confinement, and there is very little overlap of the higher order TE_2 mode with the MQW layers. As the ridge width increases beyond 2.2 µm the difference in overlap for the TE_1 and TM_1 modes begins to increase slightly, and there is a noticeable increase in confinement of the higher order TE_2 mode. For the widest ridge width of 3.0 µm, there is only a 10% difference in confinement between the TE_1 and TE_2 modes. The deep-etched ridges, seen in Figure 3.3.2(b), show that single mode behaviour is observed for only the narrowest ridge widths, namely 1.6 and 1.8 µm. Beyond this width the confinement of the TE_1 and TE_2 modes are almost identical. There is approximately a 4% confinement difference between the TE_1 and TM_1 modes, for all ridge widths in the deep-etch structures. At a ridge width of 1.8 µm, where both etch depths appear to be single mode, the simulated results show slightly higher confinement of the fundamental TE_1 mode in the deep-etch structures (19%) compared to the shallow-etch structure (16%).

The FDE simulation results indicate that to increase the confinement of the fundamental TE_1 mode a deep-etched RWG is preferential over a shallow-etched RWG. However, this is at the expense of needing much narrower ridges, for the deep-etch structures, to maintain single mode operation. Conversely, the shallow-etch RWG does not cut through the MQW layers of the structure and therefore the modes are not completely confined under the ridge which means higher order modes are not bound and guided for ridge widths up to 2.2 µm. However, this also leads to poorer confinement of the fundamental TE_1.

At first it may seem intuitive to choose a deep-etch narrow ridge for the final TW-SOA, however, as previously stated, very deep and narrow ridges can be susceptible to non-radiative recombination and scattering losses via surfaces states created during the fabrication stage. This can ultimately lead to an inefficient TW-SOA and therefore it is beneficial to fabricate a set of devices with both etch depths to understand how detrimental these losses are for the epitaxial structure in question and to verify the results obtained from the FDE simulations. Chapter 5 discusses in detail the impact of each RWG geometry on device performance.

3.4 Suppressing Cavity Resonances

To realise a functional TW-SOA a mechanism for lowering the amount of light coupling back into the waveguide, due to reflections, needs to be employed. When optical feedback occurs, resonant and anti-resonant features will be visible as "ripples" in the measured gain spectrum of the device. These features are aptly known as gain ripple and are depicted in Figure 3.4.1. Gain ripple is a major limiting factor to the performance of an SOA, causing inter-symbol interference and depleting the device gain which leads to insufficient amplification on incoming optical signals [5].
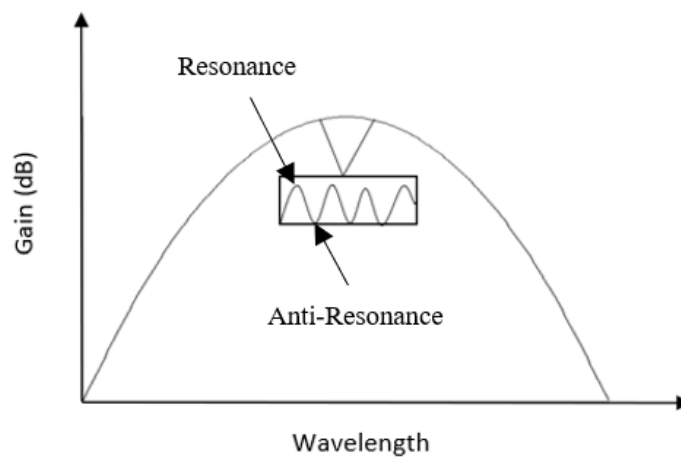
Figure 3.4.1: Sketched example of gain ripple in an SOA.

Theoretically, an *ideal* TW-SOA would have a gain ripple value of zero, however, realistically, this is incredibly difficult to achieve. Typical values of gain ripple, for commercially available C-Band SOAs, have a maximum around 0.5 dB [6-8] and therefore it is reasonable to aim for a gain ripple value better, but certainly no worse, than this value. The gain ripple, G_r, of an SOA is defined as the ratio between the maximum (resonant) gain and minimum (anti-resonant) gain and can be modelled using equation (3.1)

$$G_r = \left(\frac{1 + G_s\sqrt{R_1 R_2}}{1 - G_s\sqrt{R_1 R_2}} \right)^2 \tag{3.1}$$

where G_s is the single-pass amplifier gain, R_1 and R_2 are the intensity reflectivity coefficients of input and output facets, respectively [9].

It is clear from equation (3.1) that to reduce gain ripple it is essential to reduce the geometric mean facet reflectivity, $\sqrt{R_1 R_2}$. If the facet reflectivity remains too high, the value of the gain ripple will also be too high which ultimately depletes the single pass gain and distorts the signal at the output of the SOA. Modelling $\sqrt{R_1 R_2}$ as a function of G_s for $G_r = 0.5$ dB we can obtain an acceptable value of facet reflectivity for the TW-SOA.

From Figure 3.4.2 for single pass gain of 30 dB and gain ripple of 0.5 dB, both facets need to have, at most, a reflectivity of approximately 1.2×10^{-4}, as indicated by the red arrow. Typically, AlGaInAs cleaved facet laser didoes have (uncoated) facet reflectivity values in the region of 0.3 and therefore some work needs to be done to target $\sqrt{R_1 R_2} = 10^{-4}$. Previous work has demonstrated $\sqrt{R_1 R_2}$ in the region of 10^{-4} [10] but these often rely on complex and expensive techniques that can limit the application of an SOA due to the complications outlined in Chapter 1. Therefore, the following subsection outlines the use of a single layer TaO_x antireflective thin film as a straightforward approach of achieving competitively low facet reflectivity.
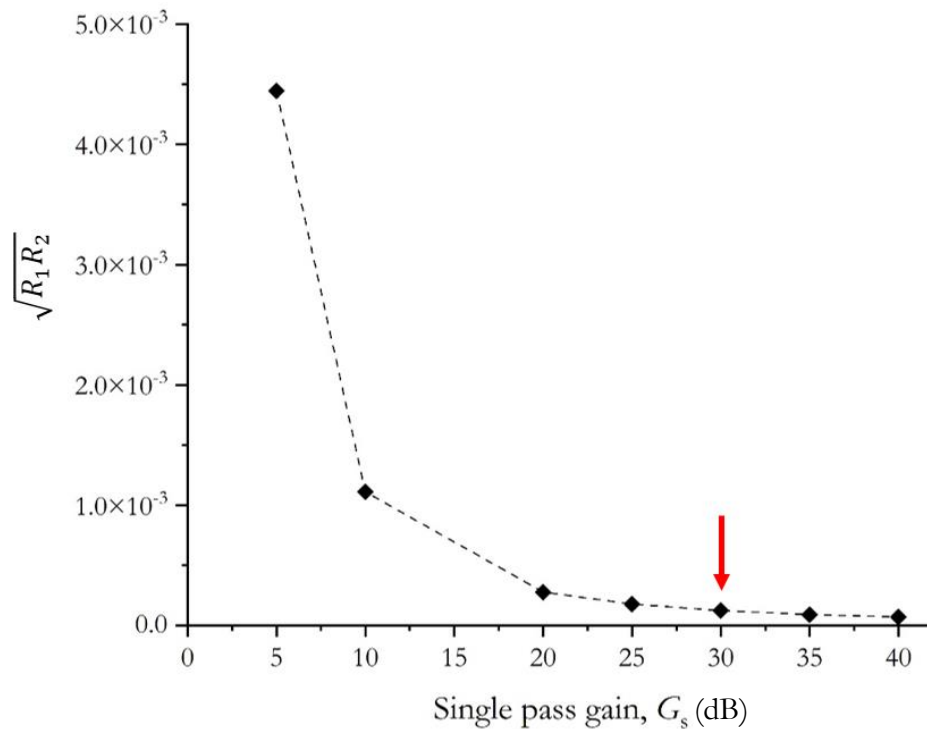
Figure 3.4.2: Geometric mean facet reflectivity versus single pass gain for gain ripple of 0.5 dB. Red arrow indicates the maximum reflectivity, $\sqrt{R_1 R_2} = 1.2 \times 10^{-4}$, for $G_s = 30$ dB.

3.5 Design and Optimisation of Single Layer Anti-Reflective Coating

Using the thin film theory outlined in Chapter 2, an ideal single layer antireflective thin film is modelled, and the parameters retrieved for the refractive index, n_{film}, and thickness, d of the film. Simulations are carried out to model the planewave interference effects between the air/film/substrate interfaces. FDTD and STACK simulation packages are used to monitor the reflection and transmission as a function of film thickness and source wavelength.

3.5.1 AR-Coating Parameters

Theory suggests that to be able to realise an AR thin film suitable for a low gain ripple TW-SOA, the coating must have a refractive index that is equal to the square root of the product of the refractive indices of the two media surrounding the film, which in this case is the semiconductor (facet) and air. The emitted light will exit a waveguide composed of different semiconductor materials, each with their own associated refractive index, and enter the surrounding air, which has a refractive index, $n_{\text{air}} = 1$. Therefore, the effective refractive index, n_{eff}, of the propagating fundamental TE (lasing) mode is used to find the desired film refractive index. The FDE simulations, detailed in the previous subsection, gives an effective refractive index value of $n_{\text{eff}} = 3.24$, for all RWG heights and widths. Incorporating this value into equation (3.2) theory suggests that for zero reflectivity, the thin film must have a refractive index of

$$n_{\text{film}} = \sqrt{n_{\text{eff}} n_{\text{air}}} = 1.80 \tag{3.2}$$

The thickness of the coating, d, can be found from equation (3.3) below,

$$d = \frac{\lambda}{4 n_{\text{eff}}} \approx 215 \text{ nm} \tag{3.3}$$

where the wavelength of light, λ, is centred around 1550 nm.

3.5.2 AR-Coating FDTD Simulations

A Finite-Difference Time Domain (FDTD) solver, offered by (Ansys) Lumerical, is used to simulate the planewave reflectivity of the AR thin film as a function of thickness.

The data is collected from the specified simulation region by solving Maxwell's equations on a discrete spatial and temporal grid which monitors the EM field interactions between materials of different refractive indices, as detailed in subsection 2.6. The finer details of the solver physics can be found on the Ansys Lumerical website **[11].**

Figure 3.5.1 shows the layout of the simulation objects where two 3D blocks are constructed using the GUI to represent the object to be coated (facet) and the material that makes up the thin film coating. The objects are assigned dimensions and refractive indices via the edit object window. The pink block represents the facet to be coated, where the n_{eff} represents the effective index of the fundamental waveguide mode, found during the FDE simulation in the previous subsection. The blue block represents the thin film coating, where n_{film} is the specified refractive index, calculated using equation (3.2). The planewave source is positioned a fixed distance from the film surface at an incidence angle of 0° and operating wavelength of 1550 nm. Two monitors, one transmission and one reflection, are placed to the front and rear of the source, respectively. The simulation is scripted to carry out a parameter sweep to measure both the transmission and reflection coefficients whilst sweeping through thicknesses from 0-1000 nm, in 1 nm steps. This stage helps to find all the reflectivity minima across a given thickness range which may be useful in the film optimisation stage.
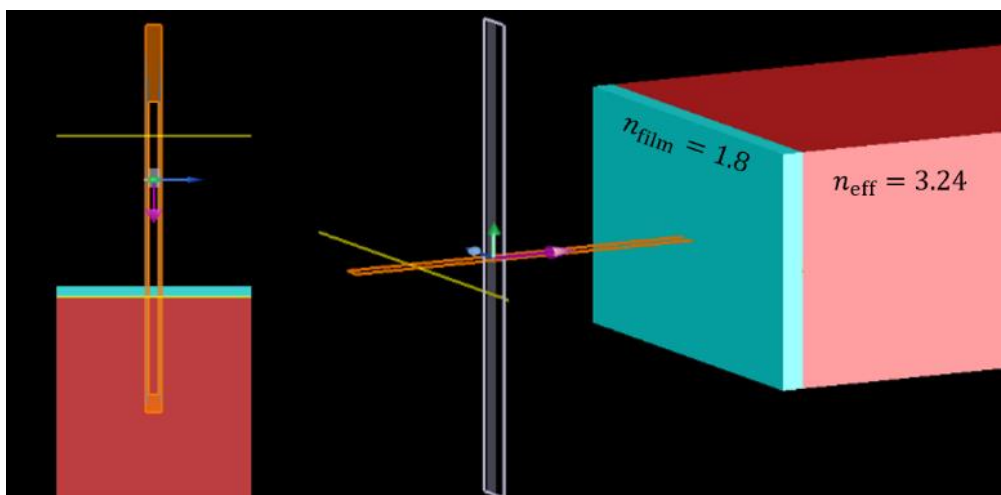
Figure 3.5.1: Planewave FDTD simulation of a single layer anti-reflective thin film applied to a material with a refractive index equal to the effective refractive index of fundamental mode of the TW-SOA. The wavelength of the plane-wave source, λ_{source}, is fixed at 1550 nm.

The simulated reflectivity, as a function of film thickness can be seen in Figure 3.5.2 below.
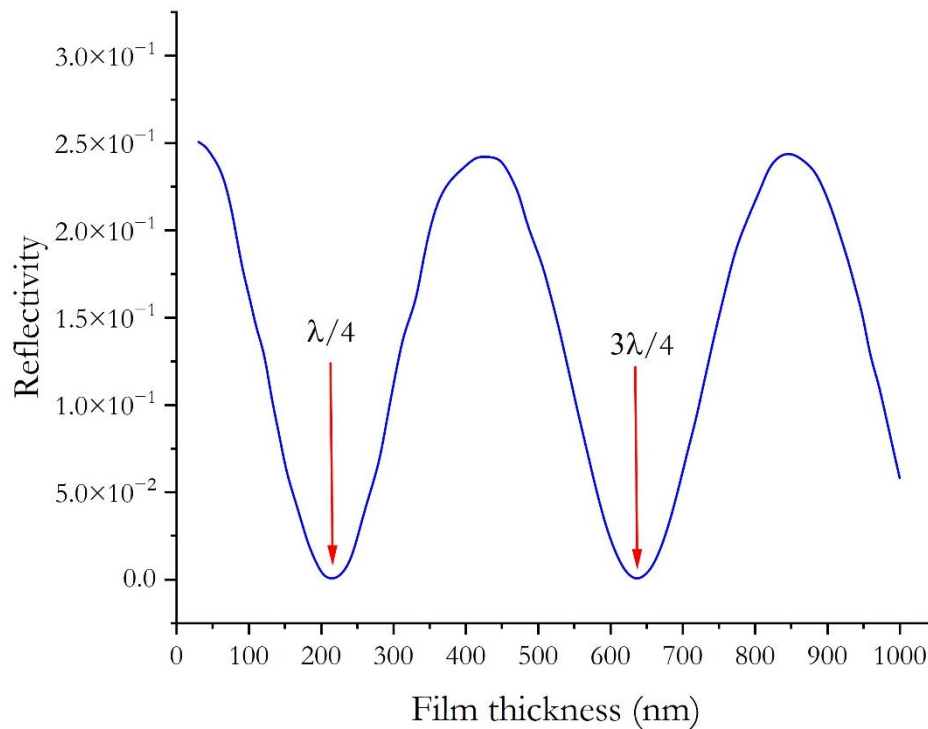
Figure 3.5.2: Simulated reflectivity as a function of film thickness from the simulation in Figure 3.5.1. 1550 nm planewave source is positioned at normal incidence to the film surface.

The simulation data shows two minima and two maxima of reflectivity across the 1000 nm thickness range. The two minima occur at approximately 215 nm and 645 nm which coincide with the expected quarter-wave thickness (or odd integer multiples of) detailed in Chapter 2. Theory suggests that the reflection coefficient, R, would be zero if the *ideal* film refractive index and thickness are met. However, as stated in Chapter 2 and 4, fabricating a thin film with such precise refractive index, and thickness is challenging, and mainly limited by both the technique and equipment used for depositing the thin film. Therefore, to account for this limitation, the n_{film} value is only specified to one decimal place and d varied to the nearest nm. This explains why, at 1550 nm, the simulated reflectivity minimum is approximately 2×10^{-6} instead of the theoretical value of zero.

3.5.3 AR-Coating STACK Simulations

The FDTD simulation software is useful for carrying out initial parameter sweeps and optimisations on 2D/3D structures, but running this simulation is data intensive and time consuming and therefore, to carry out further parameter sweeps, namely reflectivity as a function of wavelength, and refractive index, a 1D solver is used.

Figure 3.5.3 shows the layers in the GUI of the STACK solver. The reflection and transmission values of a planewave are found using the analytic transfer matrix method. The 'stackrt' function returns the fraction of transmitted and reflected power and the complex reflection and transmission coefficients for both polarisations **[12]**.
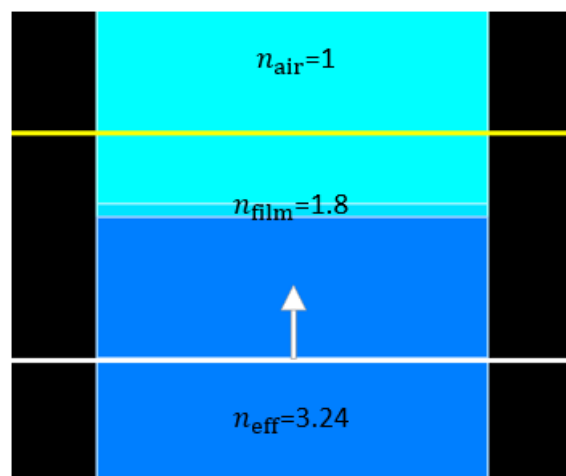
Figure 3.5.3: Planewave STACK simulation of a single layer anti-reflective thin film. The wavelength of the planewave source, λ_{source}, is varied from 1500-1600 nm.

Figure 3.5.4 shows the simulated power reflectivity as a function of wavelength, for film thickness, d=215 nm, and refractive index, $n_{\text{film}} = 1.80$. The angle of incidence is kept at 0°. The results seen in Figure 3.5.4 focus on the film thickness corresponding to the first reflectivity minimum in Figure 3.5.2, but with an increased number of data points, so that the reflectivity is measured in steps of 0.1 nm as opposed to 1 nm. This gives a more accurate value of reflectivity at 1550 nm (1.7×10^{-6}) as well as information about the change in magnitude of film reflectivity due to small changes in wavelength of emitted light. This is important because the TW-SOAs will emit light of varying wavelengths due to spontaneous emission events within the structure.

Additional simulations are carried out to understand how the minimum of the reflectivity curve shifts with changes in film thickness and refractive index, not only for optimising the coating for emission across the C-Band wavelengths, but to understand what film properties are expected

when considering the error in these parameters for the chosen deposition technique. Figures 3.5.5 and 3.5.6, and Table 3.1 show the details of these simulated parameter changes.
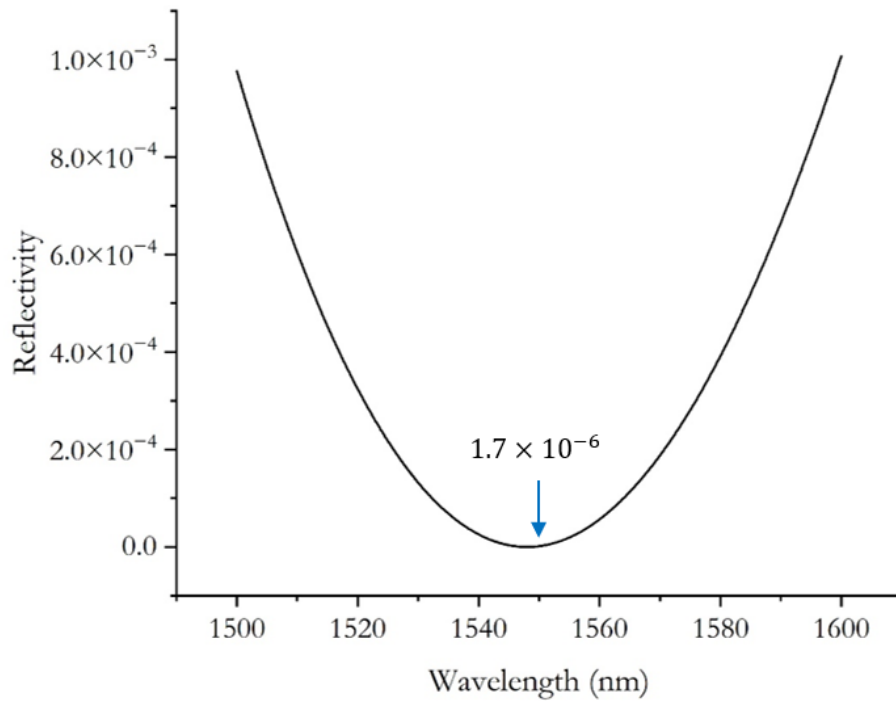
Figure 3.5.4: Planewave STACK simulation of a single layer anti-reflective thin film. The wavelength of the planewave source, λ_{source}, is varied from 1500-1600 nm. d =215 nm, n_{film} =1.80.
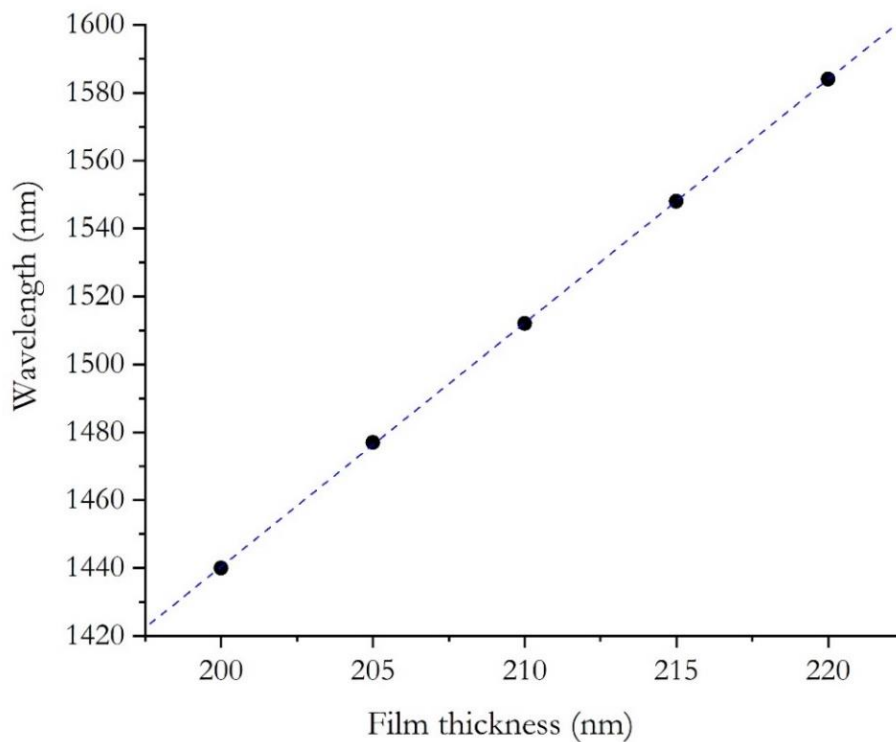
Figure 3.5.5: Simulated wavelength shift of minimum reflectivity as a function of film thickness, d. n_{film} = 1.80. Dashed blue line represents the linear fit with equation $y = 1.78x + 4.4$.

As expected for a single layer AR-coating, the minimum of reflectivity is sensitive to changes in film thickness, experiencing wavelength shifts of approximately 35 nm for a 5 nm difference in thickness, allowing tuning across the C-Band region. Previous work **[13]** using the chosen deposition technique has observed approximately 3 nm deviations from target film thickness, and errors of ± 0.03 for n_{film}. Table 3.1 shows the reflectivity as a function of wavelength for the films that are 212 nm and 217 nm – 3 nm deviations around the ideal 215 nm value. Despite this shift in thickness, the reflectivity is still no higher than of 10^{-4} across the region of interest.

Table 3.1: Simulated reflectivity as a function of wavelength for 3 nm error in film thickness. Ideal thickness is 215 nm and $n_{film} = 1.80$.

Film Thickness (nm)	Reflectivity 1530 nm	Reflectivity 1540 nm	Reflectivity 1550 nm	Reflectivity 1560 nm
212	5.4×10^{-6}	7.5×10^{-5}	2.2×10^{-4}	4.4×10^{-4}
215	1.3×10^{-4}	2.5×10^{-5}	1.7×10^{-6}	5.7×10^{-5}
217	4.3×10^{-4}	2.0×10^{-4}	6.1×10^{-5}	2.2×10^{-6}

Figure 3.5.6 shows the change in reflectivity for deviations in refractive index across the C-Band region. Again, the reflectivity remains low across the region of interest for the possible error in film refractive index.
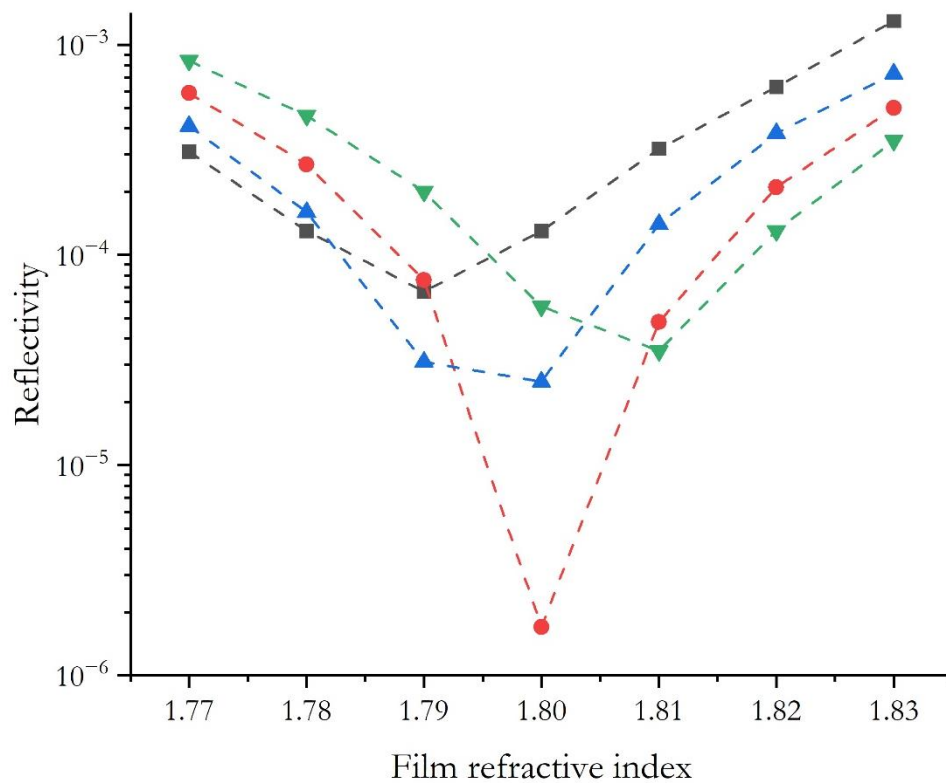
Figure 3.5.6: Simulated reflectivity due to changes in thin film refractive index. d=215 nm. Black (1530 nm), Blue (1540 nm), Red (1550 nm), and Green (1560 nm).

The FDE mode simulation work carried out in subsection 3.3 suggests that a 1.8-2.0 μm shallow-etched RWG design could be preferential for achieving single mode amplification in the TW-SOA whilst still preventing the mode from being exposed to the sidewalls of the ridge, thus leading to lower optical losses due sidewall recombination when the device is operated. Modelling the gain ripple versus geometric mean facet reflectivity, $\sqrt{R_1 R_2}$, in subsection 3.4, implies that at most $\sqrt{R_1 R_2} = 1.2 \times 10^{-4}$ for a functional TW-SOA. The FTDT and STACK simulations give indication of the ideal thickness and refractive indices for the TaO_x antireflection coating. In particular, the STACK simulation demonstrate that the minimum of the reflectivity curve appears at a one wavelength for a single layer antireflection coating, but if the ideal thickness and refractive index is obtained, the reflectivity remains low for the wavelengths of interest (1530-1565 nm). However, simulations of thickness and refractive index tolerances demonstrate a noticeable shift in the minimum of reflectivity over the C-Band region. The data in subsection 3.5.3 shows that a 5 nm deviation in thickness can shift the minimum of reflectivity by up to 20 nm, whilst a refractive index difference of 0.1 can increase the reflectivity by two orders of magnitude. This is useful in demonstrating the tunability of the TaO_x thin film, and therefore it's application in devices covering a wide range of wavelengths. However, it also highlights the importance of choosing a deposition technique that can deposit a TaO_x film with the level of precision necessary for a antireflection coating of optimum performance.

Chapter 3 References

[1] J. Minch, S. H. Park, T. Keating and S. L. Chuang, "Theory and experiment of In/sub 1-x/Ga/sub x/As/sub y/P/sub 1-y/ and In/sub 1-x-y/Ga/sub x/Al/sub y/As long-wavelength strained quantum-well lasers," in *IEEE Journal of Quantum Electronics*, vol. 35, no. 5, pp. 771-782, May 1999, doi: 10.1109/3.760325.

[2] Selmic. S.R, Chou. Tso-Min, Sih. Jiehping, Kirk. J, Mantle, A., Butler, Jerome, Bour. D. and Evans. Gary, (2001). Design and characterization of 1.3-μm AlGaInAs-InP multiple-quantum-well lasers. Selected Topics in Quantum Electronics, *IEEE Journal of.* 7. 340 - 349. 10.1109/2944.954148.

[3] MODE - Finite Difference Eigenmode (FDE) solver introduction, https://optics.ansys.com/hc/en-us/articles/360034917233-MODE-Finite-Difference-Eigenmode-FDE-solver-introduction, accessed on 28/06/2021.

[4] A. V. Ivanov, V. D. Kurnosov, K. V. Kurnosov, A. A. Marmalyuk, V. I. Romantsevich, Y. L. Ryaboshtan, R. V. Chernov, "Refractive indices of solid AlGaInAs solutions," *Quantum Electron.*, 37(6), pp. 545-548, 2007. DOI 10.1070/QE2007v037n06ABEH013442.

[5] M. Z. Iqbal, K. B. Ma, C. E. Zah, T. P. Lee and N. K. Cheung, "Effects of gain ripples in semiconductor optical amplifiers on very high speed lightwave systems," in *IEEE Photonics Technology Letters*, vol. 2, no. 1, pp. 48-50, Jan. 1990, doi: 10.1109/68.47039.

[6] Thorlabs C-Band Optical Amplifiers, https://www.thorlabs.com/newgrouppage9.cfm?objectgroup_id=3901, accessed on 30/06/23.

[7] Amonics, Specialist in Optical Amplifiers, https://www.amonics.com/product/7, accessed on 30/06/23.

[8] LD-PD INC, Singapore, C-Band Semiconductor Optical Amplifiers, http://www.ld-pd.com/?a=cp3&id=383#bkdd2, accessed on 30/06/23.

[9] M. J. Connelly, "Semiconductor Optical Amplifiers", Springer New York, NY, 978-0-7923-7657-6, pp. 16-17, 31 January 2002.

[10] X, Li, L. Liang, L. J. Wang, L. Qin, Y. Y. Chen, Y. B. Wang, Y. Song, Y. X. Lei, P. Jia, Y. G. Zeng, CHUAN T. Zheng, H. Zhao, "Monolithic Integrated Semiconductor Optical Amplifier With Broad Spectrum, High Power, and Small Linewidth Expansion," in IEEE Access, vol. 9, pp. 98863-98873, 2021, doi: 10.1109/ACCESS.2021.3096519.

[11] Finite Difference Time Domain (FDTD) solver introduction, https://optics.ansys.com/hc/en-us/articles/360034914633-Finite-Difference-Time-Domain-FDTD-solver-introduction, accessed on 28/06/2023.

[12] Ansys Optics, STACK Optical Solver Overview, https://optics.ansys.com/hc/en-us/articles/360034914653-STACK-Optical-Solver-Overview, accessed on 26/03/23.

[13] Private communication, SJ. Gillgrass, Cardiff University, November 2022.

Chapter 4

Fabrication and Sample Preparation Techniques

The following chapter outlines the various stages of device and thin film fabrication carried out to realise a TW-SOA, including a detailed description of the steps taken to prepare the samples for both coating and device characterisation. The device structures and TaO_x antireflective thin films detailed in this report were fabricated using the facilities available at the Institute for Compound Semiconductors (ICS) at Cardiff University in a class 1000 cleanroom.

Subsection 4.1 describes the fabrication stages undertaken to produce a set of shallow and deep-etched RWG F-P laser structures with four different ridge waveguide widths – namely 1.6/1.8/2.0/3.0 µm. A process flow document, listing the stages and details of device fabrication, can be found in Appendix C of this thesis. Subsection 4.2 details the steps taken to prepare the samples for testing, including the scribing, cleaving, and sample mounting procedure. Subsection 4.3 gives an overview of the fabrication and deposition of the TaO_x thin films, beginning with films deposited onto bare InP substrates during the optimisation stage, and onto the subsequent coating of the FP LD facets.

4.1 Fabrication of RWG Structures

The following subsection outlines the steps required to fabricate a set of RWG F-P laser diodes with different ridge widths and heights.

4.1.1 Wafer Cleave

To begin, two 15×15 mm tiles were cleaved from Wafer A using a straight diamond-tip scriber. The samples are processed in smaller tiles throughout this work to investigate the performance of each waveguide design. However, when the desired device structure is found, further processing work could be carried with an aim to process the devices on a full wafer scale. The area from which the tiles are cleaved is marked on a wafer map for future reference. Before processing begins, the tiles are cleaned in an ultrasonic bath using a combination of acetone, methanol, and isopropanol. The samples are subsequently dried and inspected to ensure all surface contaminants are removed. If debris remain, the cleaning process is repeated. Debris left on the material surface can be problematic to further processing steps.

4.1.2 SiO$_2$ Hard Mask

A 600 nm layer of silicon dioxide (SiO$_2$) is deposited via Physical Vapour Deposition (PVD) onto the InGaAs capping layer of the epitaxial structure to form the hard mask used for etching the defining features of the RWG devices. The SiO$_2$ layer is baked at 385 ºC in an inert, nitrogen rich atmosphere to enhance the structural properties of the material in preparation for the etching process. The baking process draws out moisture in the layer which promotes better adhesion to the semiconductor surface and prevents delamination of the SiO$_2$ layer during the mask etching process. This process is followed by a thickness measurement via Spectroscopic Ellipsometry (SE).

4.1.3 Spinning Resist

An adhesion promotor, called TI Prime is spun onto the tiles at around 3500 rpm followed by a bake of approximately 110 °C for 120 s. TI Prime is used to improves the adhesion of the photoresist onto the SiO$_2$ layer. This stage is followed by the application of AZ2020, a thermally stable negative tone resist which is spun and baked onto the adhesion promoter at 3000 rpm and 110 °C for 90 s. When exposed to UV light the negative resist will polymerise making it difficult to dissolve in a developer solution, meaning that the exposed resist pattern will remain on the tile and the developer will only remove the unexposed areas of resist **[1]**.

4.1.4 Maskless Lithography

Direct-write, a form of maskless projection photolithography, is used to pattern the resist. Conventional approaches to photolithography typically expose a pattern onto the sample surface through a chromium-glass mask, whereas the direct-write procedure uses computer-controlled optics to project a pattern directly onto the surface of the photoresist. The Durham Magneto Optics MicroWriter 3 Pro is used to directly transfer the desired pattern from a GDS file onto the photoresist at a resolution of 0.6 μm. This is followed by as post-exposure bake at 115 °C for 120 s before the tiles are placed in a photoresist developer, AZ7261, for 60 s. The tile is rinsed in DI water before the etching process takes place.

4.1.5 Inductively Coupled Plasma (ICP) Etching

ICP etching is a dry-etching technique that is used to define the dimensions of the RWG structure. This type of etching is chosen for Wafer A because it gives the user better control of the etch profile of the structure, which is particularly useful for the small ridge dimensions

required for the devices in this work. In addition to fast etch rates and good repeatability, the simple gas chemistry ($ArCl_2$) used during the etch process is particularly favourable for InP based structures, since it produces smooth sidewalls, less notching at the AlGaInAs layers and highly anisotropic etch profiles due to the low volatility of $InCl_x$ [2]. Using this technique, first the SiO_2 hard mask is etched using the resist mask. This is followed by oxygen plasma ashing for 120 s to remove the photoresist before the SiO_2 mask is used to etch the RWG structures. The endpoint of the etch is identified from monitoring the interferogram produced when signal from laser light is reflected off the surface of the sample during the etching process. For the shallow and deep-etch structures this etch stop point is different, and therefore each tile is etched separately.

4.1.7 Benzocyclobutene (BCB) Planarisation

BCB is applied to the samples to form an electrical isolation layer around the ridges. After a solvent-based cleaning process, a layer of AP3000 adhesion promoter is spun onto the tiles followed by a layer of BCB. This is spun at 500 rpm for 45 s to form a layer thick enough to planarise the etched ridges: slightly covering the InGaAs cap layer at the very top of the ridge. The BCB is cured in a Carbolite furnace at 210 °C for an hour, and when cooled the thickness of the BCB layer is determined using ellipsometry.

4.1.9 Reactive Ion Etching (RIE) of BCB

To expose the InGaAs capping layer of the material so the p-type metal contact can be applied, the BCB layer is back-etched using RIE. Under etching the BCB will leave the ridge encapsulated and the electrically isolated, with current unable to flow between the p and n type layers of the device structure. However, over-etching the BCB will expose both the InGaAs layer and the sidewalls of the ridge, allowing current to leak into unwanted regions of the structure and potentially cause an electrical "short" in the devices with the metal contact bridging the p-n junction.

4.1.10 P-type Metal Contact

With the InGaAs layer exposed, a Ti/Pt/Au (10/20/500 nm) p-type metal contact is deposited via thermal evaporation to the entire top surface of the tiles. A metal contact of this composition has shown to be superior choice for structures with InGaAs capping layers – namely better annealing and lower resistance under forward-bias. A "lift-off" process follows the deposition to

remove metal from unwanted areas, which is subsequently followed by a Rapid Thermal Annealing (RTA) process at 280 °C for 60 minutes. The annealing temperature cannot exceed this value to ensure no damage occurs to the BCB layer, which is more sensitive to higher temperature.

4.1.11 Substrate Thinning and Polish

Prior to the substrate thinning (lapping) a thin layer of polymethyl methacrylate (PMMA) is spun onto the top surface of the tiles to protect the p-contact layer during this stage. The tiles are placed p-contact side down onto a metal chuck and onto hot plate at 100°C for approximately 3-5 minutes. The four edges of the tiles are sealed in place with a small amount of wax, and the chuck removed from the hot plate to allow the wax to cool/harden in air. When the wax is set, the cooled chuck is secured to the handheld lapping tool and the starting thickness of the tile is measured. The tile is placed, substrate side down, onto silicon carbide paper continually rotating at approximately 150 rpm, until the substrate is physically thinned (ground) away. Intermittently, water is pipetted onto the rotating wheel to produce an InP slurry so fine dust is not inhaled during the process. The thickness is measured periodically until the total tile thickness is ~ 120 μm. Thinning the substrate will help to reduce the thermal and electrical resistance of the sample when under test, but more importantly will allow the devices to be cleaved to the required cavity length. A minimum 2:1 ratio of cavity length to sample thickness is required to cleave the sample and produce a good quality facet for coating. The lapping process is followed by a polishing stage, where the substrate is smoothed using a metal micro-polish and soft polishing cloth attached to an adjacent rotating wheel. The chuck is returned to the hot plate to melt the wax and remove the tiles, before they are placed in warm n-Butyl Acetate, followed by room temperature isopropanol, for several minutes. The tiles are removed and placed on cleanroom grade tissue to air dry. The sample is inspected to ensure the substrate is both clean and smooth for improved adhesion of the n-type metal contact.

4.1.12 N-type Metal Contact

The final stage of the device fabrication is the deposition of the n-type metal contact onto the thinned InP substrate. AuGe/Ni/Au (100nm/28nm/300nm) layers are deposited via thermal evaporation onto the substrate of the tiles to form the n-type electrical contact, followed by the same thermal annealing process as the p-contact layer. The samples are probed to check

intercontact resistance of the devices before being sealed in cleanroom grade boxes, ready for sample preparation and packaging.

4.2 Sample Preparation

To realise testable devices and expose the facets for coating, the tiles need to be cleaved and mounted onto copper blocks (heatsink) and subsequently electrical test boards. The following section describes the following process in detail.

4.2.1 Scribing and Cleaving

Figure 4.2.1 shows the equipment used to add scribe marks to the surface of the RWG samples. The sample is placed onto medium-tack cleanroom tape with the patterned p-contact facing up and held in position under vacuum. Whilst viewing the sample under a microscope, the tip of the scriber is manoeuvred into position using the translational stages, where it is adjusted until it is aligned with the vertical strips of the p-contact. This step is vital to ensure the cleave propagates long the intended crystallographic plane and doesn't cleave through the contacts or devices which can ultimately damage the sample. The tip of the scribe is gently lowered until it contacts the material in the desired location, and then moving the scribe in the backward direction, a small mark is scribed into the material. This process is repeated until there are scribe marks between the four different ridge widths on both the shallow and deep-etch samples. Small marks are placed in the blue tape opposite the scribe mark to help locate its position when the sample is removed from under the microscope. The mark in the tape indicates where pressure needs to be applied for the cleave.
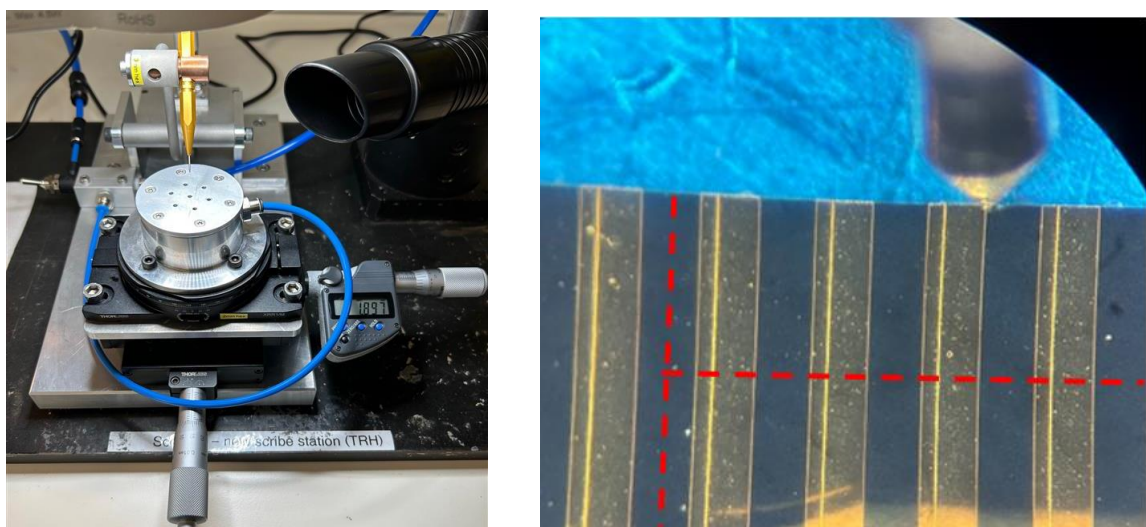
Figure 4.2.1: Equipment used for scribing semiconductor samples. Diamond-tip scriber mounted.

The vacuum is released, and the sample dismounted from the chuck. The samples are placed p-contact side down and using the mark in the tape as a guide, flat tip tweezers are gently run along the back of the sample near the scribe mark until a "click" is heard. The click is indicative that the sample has cleaved. These steps are repeated until all the devices are split into groups corresponding to the different RWG widths. A similar process is carried out to cleave the devices into the required cavity lengths, but the sample is rotated so the p-contact metal strips are positioned horizontally, or, more precisely, perpendicular to the tip of the scribe. This stage of the scribe/cleave forms the resonator cavity, where at either end of the cavity the shiny mirror-like facets will reflect light back into the waveguide. Therefore, it is imperative the scribe/cleave cause minimal damage to the facet. Tipping the scribe over the edge of the sample or making too large a scribe mark can cause the facet to shatter, leading to increased mirror losses from scattered light, and can be problematic when applying the AR-coating at a later stage. All facets are inspected after cleaving, and the highest quality samples are selected for testing.

4.2.2 Sample Packaging

To prepare the F-P RWG lasers for testing, and subsequent coating, they must first be secured to electrical test boards, as seen in Figures 4.2.2(a)-(b). The test boards and copper blocks (heatsink) are milled so their width matches the length of the laser cavity. This is a crucial step in the sample preparation process since it is essential that there is no obstruction to the facets during the TaO_x coating process. The impact of obstruction to the facet is discussed in more detail in the following subsections. The devices are secured to the copper blocks using a thin/uniform layer of silver conductive epoxy (EPO-TEK H20E) which is cured on the hot plate at approximately 180ºC for 2 minutes. The same process is used to affix the copper blocks to the test boards, but the baked time is slightly less (2 minutes) for the samples. The devices detailed in this work are all characterised using an electrical probe, removing the need for wire-bonding. The sample preparation stages are complete with a visual inspection of the devices, paying particular attention to the quality of the facet, which must not be damaged. Figures 4.2.3 (a)-(f) outline the necessary steps to prepare the samples for both testing as LD prior to coating, and for the application of the TaO_x antireflection coating.
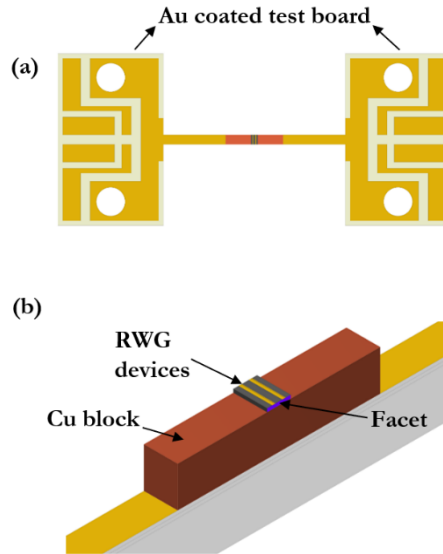
Figure 4.2.2: Sample mounting arrangement for RWG device. **(a)** Top-down view of samples mounted onto test boards. **(b)** close-up view showing the width of test boards and copper blocks matching the cavity length of the RWG devices with no obstruction to the facet.

(a) Using a diamond tip scriber, cleave 15X15 mm sample into groups of 6 devices with the desired cavity lengths, i.e., 1mm.	**(b)** Clean sample after cleaving to remove debris. Inspect both cleaved ends of sample for damage to the facet.	**(c)** Mill copper blocks and test boards to the required length, i.e., to match the length of the LD cavity. In the case of sample J3, 1mm.
(d) Inspect the edges of the copper blocks and test boards to ensure they are clean, and flat. Rough edges will compromise the mounting process.	**(e)** Affix copper block to test board using silver conductive epoxy, EPO-TEK H20E. Bake on hot plate at 180ºC for 3-5 minutes.	**(f)** Affix the RWG LD to test board using the same conductive epoxy. Bake on hot plate at 180ºC for 2 minutes.

Figure 4.2.3: Steps **(a)**-**(f)** outline of the necessary stages to prepare/package the LD samples for testing. Test boards are used specifically for ease of application of ARC to produce a TW-SOA.

4.3 Thin Film Deposition

Electron-beam evaporation is chosen as the AR-coating deposition technique for this work; a large scale and cost-effective approach to coating substrates at high deposition rates which is ideal for thicker single layer coatings. Controlling and monitoring the chamber conditions during the optimisation stage found a relationship between the measured refractive index of the TaO_x film and the oxygen flow rate within the evaporator chamber. Using this knowledge, several coating iterations were carried out on InP substrates until a film with the desired optical properties was achieved. These chamber conditions were replicated to apply the coating to the RWG LD facets.

4.3.1 Electron-Beam Evaporation

Electron-beam (e-beam) evaporation is a well-established process for depositing thin film optical coatings onto a variety of different substrates [2]. E-beam evaporation is a Physical Vapour Deposition (PVD) technique that is carried out under vacuum, phase changing the source material to a vapour before returning it to a solid as it strikes the substrate surface to form a thin layer of material of desired thickness.

Figure 4.3.1 shows a labelled photo of the evaporator used in this work for depositing the TaO_x AR coatings. The chamber is prepared by loading the substrate/samples into the evaporator and adding 2-3 Ta_2O_5 tablets to the crucible. The Ta_2O_5 source material used in this work is in the form of solid white tablets that are 8-9 mm in diameter and 4-5 mm in thickness. It is imperative the crucible is not overfilled, or the material will spill over the sides of the crucible, causing an electrical short. The evaporator door is locked, and the chamber evacuated to a base pressure of approximately 10^{-5} mbar. Initially, the e-beam is swept at low power to fuse the surface of the Ta_2O_5 source to avoid hole-drilling, as recommended by the material distributor [3].

The evaporation begins when current is passed through a tungsten filament resulting in the thermionic emission of electrons which are accelerated by a high voltage source. The ejected electrons, travelling at high kinetic energies, are focussed into a beam, and steered towards the Ta_2O_5 source by a magnetic field. As the electron beam strikes the surface of the source material, its kinetic energy is converted to thermal energy, causing the sublimation of Ta_2O_5 which travels through the chamber atmosphere towards the target, subsequently cooling and condensing onto the substrate surface. This process continues until the sample is covered by a thin film of specified thickness.
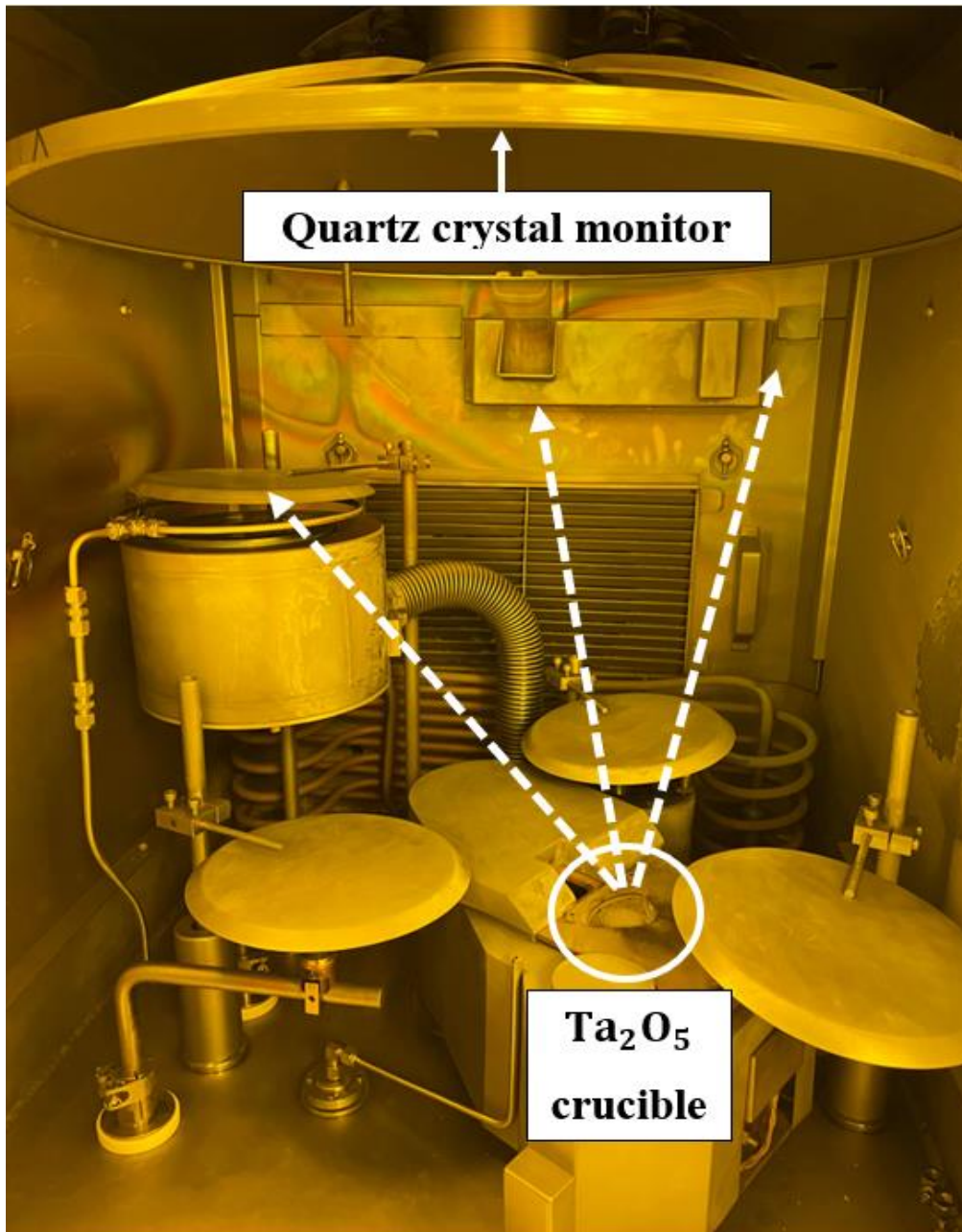
Figure 4.3.1: Buhler Syrus LC III Electron beam evaporation system used for TaO_x thin film deposition.

4.3.2 TaO_x Thin Film Optimisation

To deposit metal-oxides, a reactive gas is pumped into the chamber during the evaporation. Previous work has demonstrated the use of e-beam evaporation to tune the optical properties of metal-oxide thin films by varying the oxygen partial pressure during the deposition **[4]**. The same principle is applied here for TaO_x. Figure 4.3.2 shows the variation in refractive index as a function of oxygen flow rate for TaO_x AR coatings deposited onto bare InP substrates. The refractive index is measured using Spectroscopic Ellipsometry (SE) at an angle of 75° at the target wavelength of 1550 nm.
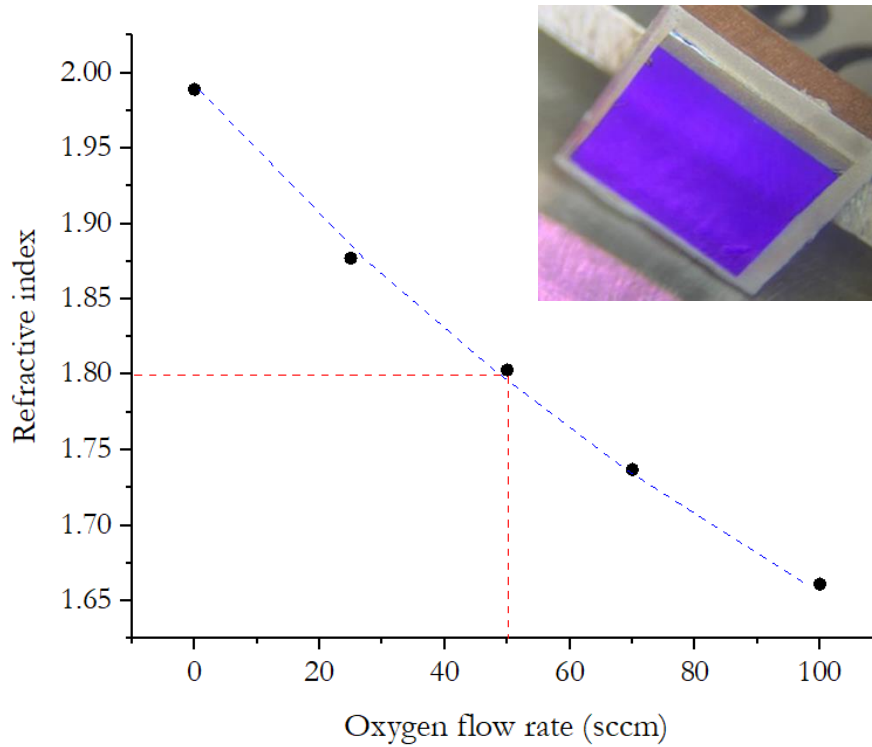
Figure 4.3.2: Refractive index of e-beam evaporated TaO_x thin films as a function of chamber oxygen flow rate. Measured at 1550 nm. The fit (dashed blue line) is given by $y = 1 \times 10^{-5}x^2 - 0.0043x + 1.986$. Permission of SJ Gillgrass [Cardiff University]. Inset: TaO_x coating at 50 sccm oxygen on InP substrate.

The refractive index of the film decreases as the oxygen flow rate increases. This can be explained by looking at Figure 4.3.3, where it's shown that increasing the oxygen flow rate during the evaporation increases the vacuum pressure within the chamber. During the evaporation the particles of source material collide with many oxygen molecules as travel through the oxygen-rich atmosphere created within the chamber which can lower their kinetic energy. The melting temperature of the source material is significantly higher than that of the substrate surface, since there is no applied substrate heating during the evaporation and therefore the substrate will only experience the heat emitted by the e-beam gun. These factors combined impact the structure of the thin film layer since particles of source material arrive at the substrate with decreased mobility and thermal energy which can lead to the formation of a TaO_x coating with a low packing density **[5-6]** and thus lower refractive index, at the wavelength of interest.
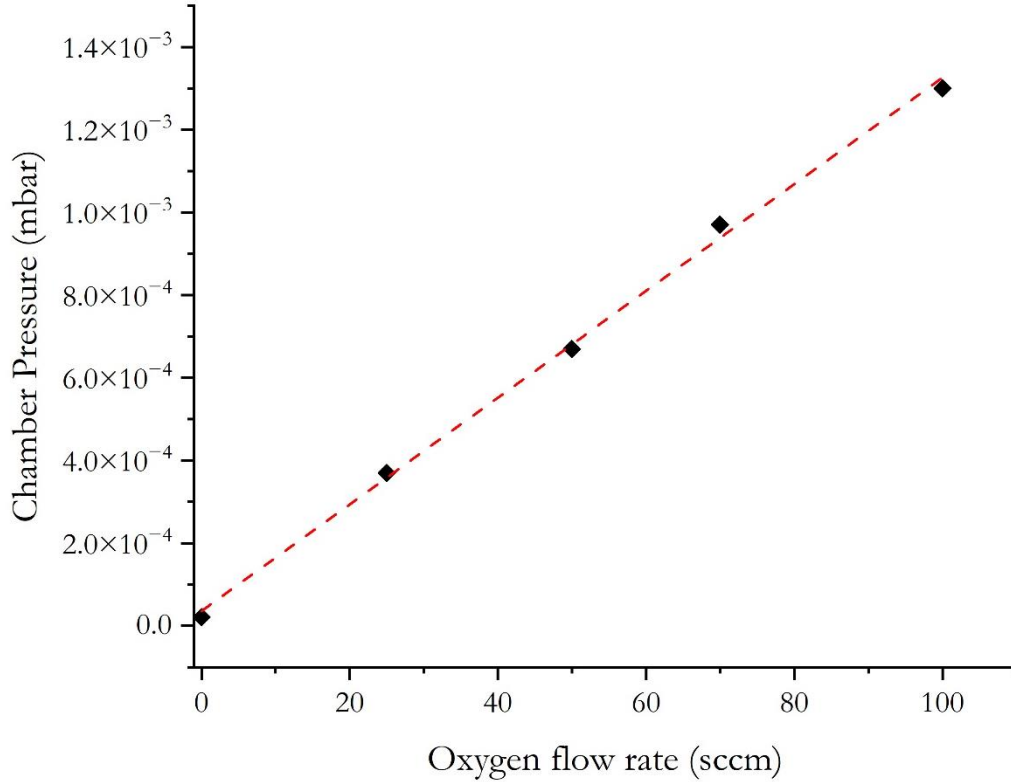
Figure 4.3.3: Refractive index of e-beam evaporated TaO_x thin films as a function of chamber pressure. Measured at 1550 nm. The fit (dashed red line) is given by $y = 1.3 \times 10^{-5}x + 3.6 \times 10^{-5}$.

Using the results obtained in the optimisation stage, an oxygen flow rate of 50 sccm is selected to achieve a film that is closest to the target refractive index, $n_{film} = 1.80$, as detailed in Chapter 3. The required film thickness, $d = 215$ nm, is set via the control panel of the evaporator. A crystal thickness monitor, positioned near the mounted samples, continuously monitors the deposited film thickness, automatically closing the shutter to cover the Ta_2O_5 source when this value has been reached, stopping additional material reaching the sample.

4.3.3 TaO_x Laser Facet Coating

Following the optimisation stage, the packaged LD samples were affixed to the evaporator plate using a custom-made mount, as seen in Figure 4.3.4. The fixture is designed to screw into the evaporator plate from either side, allowing each facet to be coated individually for improved thickness control. The mount can be easily unscrewed and flipped to coat each facet without the need to remove the test boards. The sample holder used in this work lowers the likelihood of device damage during the loading/unloading process and is different to the industrial standard where lapped bars are not mounted to test boards prior to coating but are stacked together instead and loaded directly into the evaporator in custom-made jigs.

The plate is fastened to the vertical rod, which remains stationary during the evaporation, and in direct line-of-sight to the Ta_2O_5 crucible, to ensure the lapped facet is sufficiently coated. The sample positioning in the evaporator is very important since e-beam evaporation is a directional deposition technique. An e-beam evaporated film coats planar surfaces very well, however, it is not conformal when coating structures with complex geometries. This is the reason the samples were prepared and packaged as outlined in subsection 4.2.2, with the test boards and copper blocks milled to the match the length of the TW-SOA cavity.
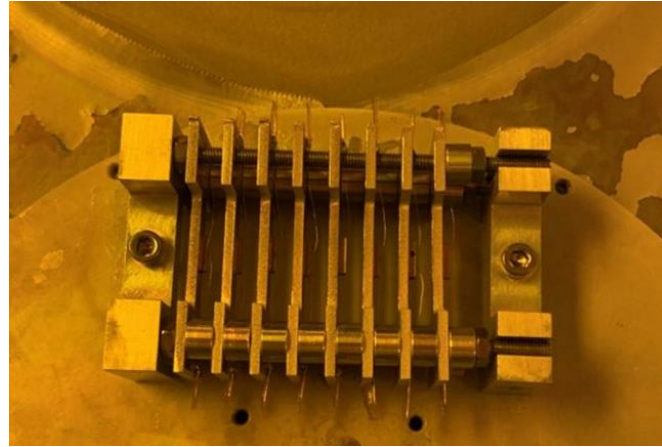
Figure 4.3.4: Holder for coating laser diode facets in evaporator.

Initial deposition tests noted that any obstruction to the facet during the evaporation leads to the formation of a TaO_x layer of insufficient thickness and consequently leads to a higher facet reflectivity. The first set of devices were affixed further away from the edge of the copper block, and it was noted that the end of the copper blocked stopped the device facet from being completely coated. Visual inspection of the facets saw a distinct colour difference between the devices that had too little coating (gold) and the devices that were coated closer to the correct thickness (purple), as seen in Figure 4.3.5. The undercoated devices exhibited significant ripples in the measured emission spectrum and in some cases, lasing was still observed.
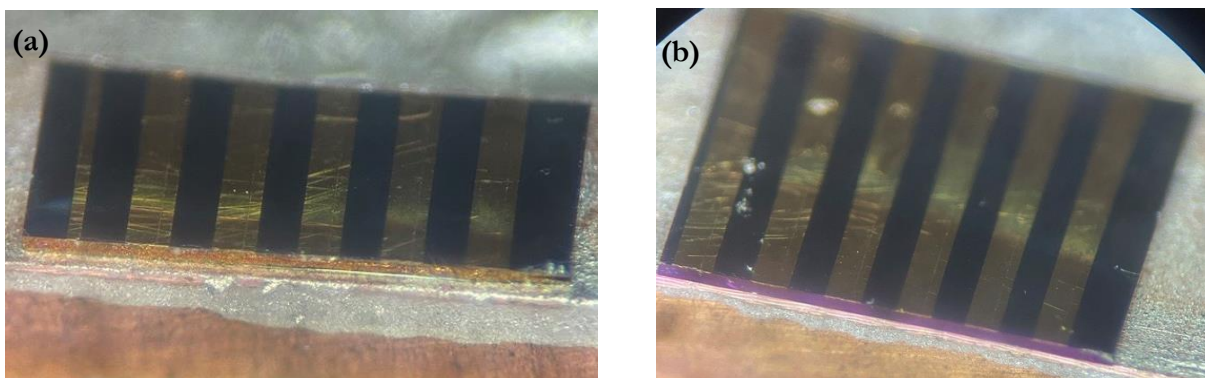
Figure 4.3.5: (a) undercoated facet (gold) **(b)** correct coating thickness (purple).

Table 4.1 details the evaporation parameters used for the set of samples that include Board J, in particular sample J3, which is described in detail in Chapter 5. The measured refractive index and thickness values are taken via ellipsometry measurements for the monitoring sample of bare InP substrate, placed next to test boards during the evaporation. The ellipsometry measurements revealed an extinction coefficient, $k = 0$, for the deposited TaO_x film, indicating no appreciable increase in absorption of light over the wavelength of interest, as discussed in subsection 2.5.1.

Table 4.1: E-beam evaporator parameters used to coat sample J3. Refractive index and thickness measured via ellipsometry on InP test sample positioned next to sample J3 during evaporation.

Oxygen Flow (sccm)	Chamber Pressure (mbar)	Deposition Rate (nm/s)	Measured Refractive Index	Measured Thickness (nm)
50	6.7×10^{-4}	0.15	1.803	216

Chapter 4 References

[1] Kayaku Advanced Materials, https://kayakuam.com/products/lithography-overviews, accessed on 28/05/2023.

[2] S. Shutts, "Monolithic Dual-Wavelength InP/AlGaInP Quantum Dot Lasers," PhD thesis, Cardiff University, pp. 66-74, September 2012.

[3] T. I. Awan, A. Bashir, A. Tehseen, "Chemistry of Nanomaterials: Fundamentals and Applications", Elsevier, 2020, Chp. 3, pp. 51-87.

[4] Kurt. J. Lesker, Tantalum Pentoxide (Ta2O5) Tablets & Pieces Evaporation Materials, https://www.lesker.com/newweb/deposition_materials/depositionmaterials_evaporationmaterials_1.cfm?pgid=ta4, accessed June 2022.

[5] Li S, Yang C, Zhang J, Dong L, Cai C, Liang H, Liu W, "Tunable Optical Properties of Amorphous-Like Ga_2O_3 Thin Films Deposited by Electron-Beam Evaporation with Varying Oxygen Partial Pressures", Nanomaterials (Basel). 2020 Sep 6;10(9):1760. doi: 10.3390/nano10091760.

[6] Seouk-Hoon Woo, Chang Kwon Hwangbo, Young Bae Son, Il Choon Moon, Geon Mo Kang, Kwang-Su Lee, "Optical Properties of Ta_2O_5 Thin Films Deposited by Plasma Ion-Assisted Deposition", *Journal of Korean Physical Society,* Vol. 46, pp. S187-S191, June 2005.

[7] Yus Rama Denny, Teguh Firmansyah, Suhk Kun Oh, Hee Jae Kang, Dong-Seok Yang, Sung Heo, JaeGwan Chung, Jae Cheol Lee, "Effect of oxygen deficiency on electronic properties and local structure of amorphous tantalum oxide thin films", *Materials Research Bulletin, Elsevier,* 82, pp. 1-6, 2016.

Chapter 5
Device and Thin Film Characteristics

This chapter outlines the experimental techniques used to characterise a single mode RWG F-P laser diode, which subsequently has both facets coated with a single layer TaO_x antireflective thin film to produce a TW-SOA.

Subsection 5.1 presents results for uncoated laser diodes with varying waveguiding geometry – namely shallow and deep-etch waveguides with different ridge widths. From the data gathered, justification for the chosen waveguide design is presented, which is used in the next stage to realise a functional TW-SOA device. Subsection 5.2 outlines the characterisation of the TW-SOA with the TaO_x thin film applied to both facets of the device, emphasising the successful realisation of a single layer AR coating that yields a facet reflectivity as low as 10^{-5} at 1550 nm. Subsection 5.3 compares the simulated and experimentally obtained values of facet reflectivity for a set of TW-SOA's, making suggestions for the observed differences in the two sets of data.

5.1 RWG Laser Diode Characteristics

To select the most appropriate waveguide structure for the TW-SOA, the shallow-etch RWG (S1) and deep-etch RWG (D2) samples detailed in Chapters 3 and 4, were first tested as standard uncoated cleaved facet F-P LDs, before subsequently being coated and tested as a TW-SOA.

The travelling-wave amplifiers in this work are designed to be implemented within optoelectronic systems that require coupling between single mode fibres and components to amplify optical signals across a narrow band of wavelengths (1530-1565 nm). Therefore, as previously stated, it is important for the fabricated structure to show single mode operation, for injection currents up to point of gain saturation, and low cavity losses so that the device demonstrates appreciable single-pass gain (25-30 dB). The electrical and optical properties of each device were explored by carrying out a set of standard experiments in the Optoelectronics laboratories at Cardiff University. Each measurement is repeated for all the different waveguide designs until sufficient data is collected to make a meaningful comparison between the different RWG geometries. For samples S1 and D2, approximately twelve F-P LD devices were tested for each RWG design. Before testing, SEM images were taken of the cleaved facets of samples S1 and D2 to verify the fabricated ridge width. An example of these images can be seen in Figures 5.1.1 (a)-(b) below.
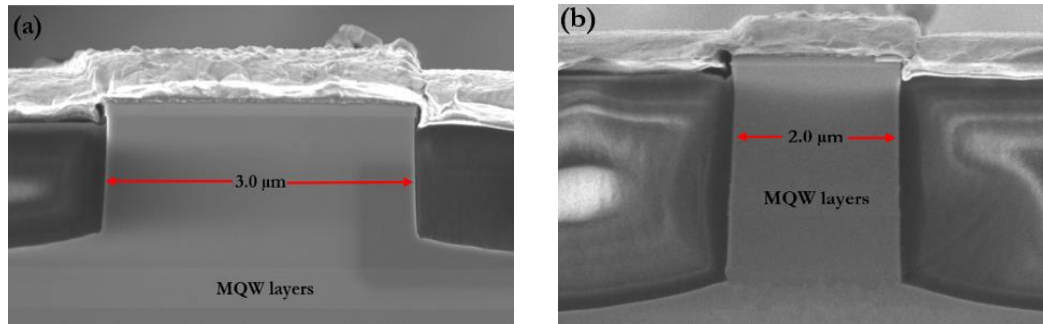
Figures 5.1.1: SEM images of **(a)** 3.0 µm shallow-etch and **(b)** 2.0 µm deep-etch RWG LD.

5.1.1 Experimental setup

The Power-Current (P-I) and spectral characteristics are measured using the experimental equipment seen in Figure 5.1.2. A tapered fibre, which is antireflection coated (1550 nm) is used to collect light from either end of the ridge waveguide, which is subsequently connected to a Thorlabs S145C integrating sphere for the P-I measurements and a Yokogawa AQ6370D spectrum analyser for measuring the emission spectrum of the device. The uncoated and coated devices were operated in forward-bias with a pulsed current source; duty cycle of 0.5%, frequency of 5.0 kHz, and pulse width of 1000 ns. The heating/cooling of the sample is achieved using a Thorlabs TED200C benchtop precision temperature controller. Of the twelve devices probed for each ridge width and etch-depth, devices most representative of each design, i.e., show similar performance to the devices with the same waveguide geometry, are used to make the following comparisons.
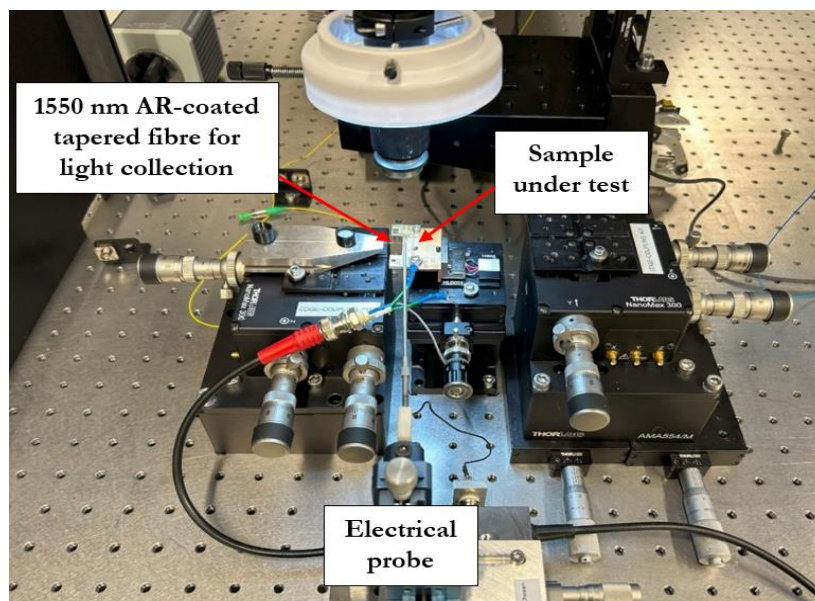
Figures 5.1.2: Experimental equipment used in pulsed P-I-V measurements. The fibre on the LHS is used for spectral measurements and connected to an optical spectrum analyser. This can be interchanged for a Thorlabs integrating sphere for P-I-V measurements.

5.1.2 FP Laser Diode Performance

P-I data is collected for each waveguide design, and the room temperature threshold current, I_{th}, interpolated from the second derivative of the P-I curve [1]. The current at which there is an on-set of lasing is identifiable from the distinct peak seen in Figure 5.1.3.
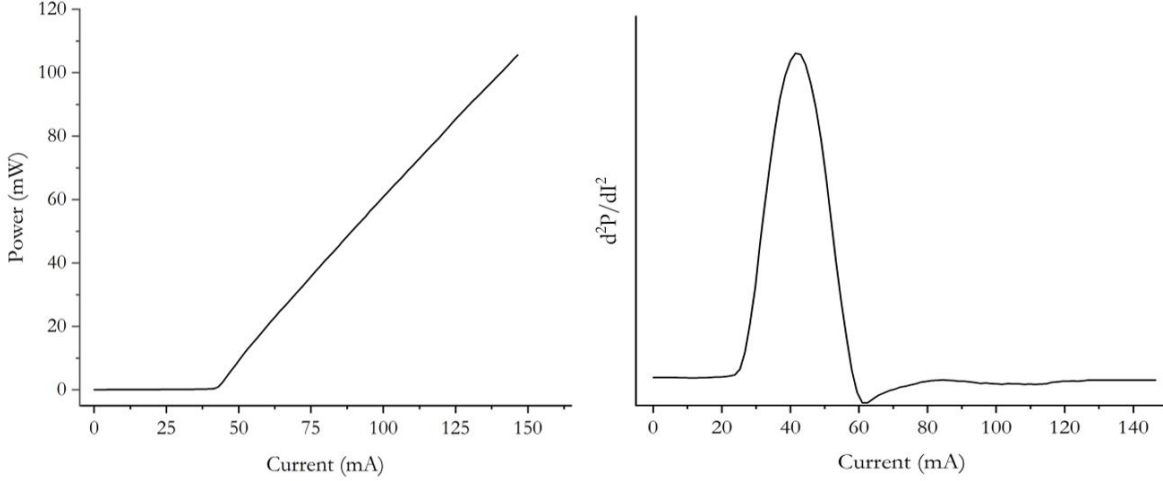
Figures 5.1.3: Second derivative $\frac{d^2 P}{dI^2}$ curve used to extract I_{th} values for LD devices. This method is used throughout this work.

Using the measured values of I_{th} , the threshold current density, J_{th}, is calculated for the varying ridge widths and etch-depths, using equation (5.1)

$$J_{th} = \frac{I_{th}}{L_c \times w_m} \tag{5.1}$$

where L_c is the length of the cavity and w_m is the width of the lasing mode.

Figure 5.1.4 shows the measured dependence of J_{th} on the varying waveguide geometries, where for the narrower ridge widths, there is a noticeable difference in threshold current density values between the shallow and deep-etch structures. The deep-etch devices, D2, show much higher threshold current density, J_{th}, values for the 1.6 μm and 1.8 μm ridge widths; these are 3.7 and 2.5 kA cm^{-2}, respectively. This can be attributed to increased scattering losses, where in very narrow, deep-etched structures, the mode is typically exposed to the sidewalls of the ridge. If the etched sidewalls are not perfectly smooth, the photons interact with this rough surface, being scattered in random directions, thus causing an increase in amplified spontaneous emission (ASE) and a subsequent decrease in stimulated emission, in the desired frequency range. [2]
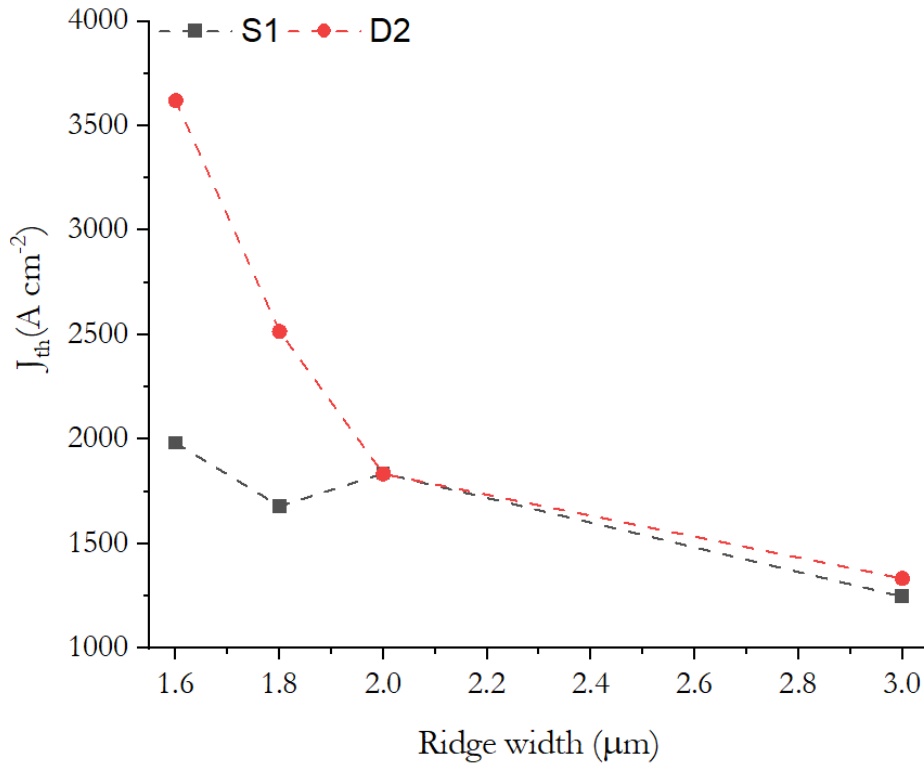
Figures 5.1.4: Plot of threshold current density, J_{th}, as a function of RWG width for samples S1 (black squares) and D2 (red circles).

As the ridge width increases, the mode is no longer exposed to the walls of the ridge, and therefore sidewall scattering losses decrease, resulting in the lower measured values of J_{th}, for the 2.0 μm and 3.0 μm ridge widths. The current density values for the 2.0 μm and 3.0 μm ridges are comparable for samples D2 and S1, however, as seen in Appendix A, as the ridge width exceeds 1.8 μm, the deep-etch structures demonstrate an increased overlap between higher-order modes and the amplifying region of the device. This is undesirable for the intended application and may result in spontaneously generated photons coupling into more than one waveguide mode, thus being amplified and leading to higher values of gain ripple across a broader range of wavelengths after the AR coating is applied. For the narrower 1.6 μm and 1.8 μm ridge widths the shallow-etch devices exhibit much lower J_{th} values, which are found to be below 2.0 kA cm^{-2}.

For samples S1, the FDE results (Appendix A) show single mode behaviour for these ridge widths, as well as mode profiles that are not fully confined under the ridge, and therefore do not "see" the sidewalls. This goes some way to explaining why the modes propagating in shallow-etch structures are less susceptible to scattering losses induced by rough sidewalls left behind during the etching process.

The experimental data gathered in this subsection, along with the simulation results, lead us to conclude that a shallow-etched 1.8 μm RWG would appear to be the most appropriate waveguide structure to realise a single-mode TW-SOA that exhibits lower cavity losses. Therefore, the remainder of this work focusses on the uncoated and coated devices with a ridge waveguide width of 1.8 μm an etch-depth of approximately 1.4 μm. The waveguide dimensions were confirmed using a Scanning Electron Microscope (SEM).

5.2 TaO$_x$ AR Coated TW-SOA Characteristics

Using the sample preparation procedures outlined in Chapter 4, a set of shallow-etched 1.8 μm RWG laser diodes were cleaved from the main sample to form a cavity of length of 1 mm. Each end of the cavity has a mirror-like facet with a reflectivity of R_1 at Facet 1, and R_2 at Facet 2. The P-I and spectral characteristics of the uncoated devices were measured to monitor device performance before coating to establish whether the device is initially lasing and if there is equal output power from each facet before the coating is applied. These characteristics are vitally important when analysing the effectiveness of the ARC, as described in the following subsections.

Following data collection from the uncoated lasers, a thin layer of TaO$_x$ is deposited via electron-beam evaporation onto each cleaved facet of the devices. The chamber conditions are replicated using the information retrieved from the thin film optimisation stage outlined in the previous chapter. Sufficient control over the chamber environment aided the deposition of a film that exhibits measured facet reflectivity values near the simulated values reported in Chapter 3. This would indicate a TaO$_x$ film, close to the target values of refractive index, $n_{\text{TaO}_x} = 1.80$ (at 1550 nm) and thickness $d = 215 \text{ nm}$, has been successfully deposited onto the cleaved facet of the RWG structures.

5.2.1 Power-Current Characteristics

Measuring the P-I characteristics of uncoated samples allows us to pinpoint devices (typically closest to the scribe mark) that do not lase and/or show an imbalance in output power, P_{out}, from either end of the cavity. Cleaved facets can suffer damage from the diamond-tip scriber used to break the semiconductor into the required cavity lengths. Damage to one/both mirrors leads to increased scattering losses at this interface, whilst creating a non-uniform surface which can be problematic for the adhesion of the coating. If the devices show non-comparable output

power from either facet *only* after the coating is applied, this could indicate an issue with the AR coating instead of an issue that has originated from the original cleaving procedure.

Table 5.1: Measured output power from each facet of J3 before and after TaO_x AR-coating at 150 mA pulsed current.

	P_{out} (%) Facet 1	P_{out} (%) Facet 2
Uncoated	51	49
Coated	53	47

Table 5.1 shows the percentage of output power P_{out} from Facet 1 and 2 of device J3 before and after coating. The error in the quoted values is approximately ±1% due to positioning of the integrating sphere when collecting the emitted light. It can be seen that prior to coating, P_{out} from each facet is the comparable, but after coating, there is slight increase in light output from Facet 1 compared to Facet 2. This may indicate that Facet 1 has a lower reflectivity than Facet 2 which could be attributed to a slight difference in coating thickness on each facet.

Figure 5.2.1 shows the room temperature $(T = 25°C)$ pulsed P-I curves for Facet 1 of J3 before and after coating. The uncoated device (solid line) shows clear signs of a lasing, where there is a sharp "up-turn" in the P-I curve at a current value of 46 mA ± 0.3 mA. This behaviour is characteristic of lasing via stimulated emission, due to self-sustained oscillations within the cavity from the partially reflective mirrors at each end, which have Fresnel reflectivity $R_l = 0.28$.
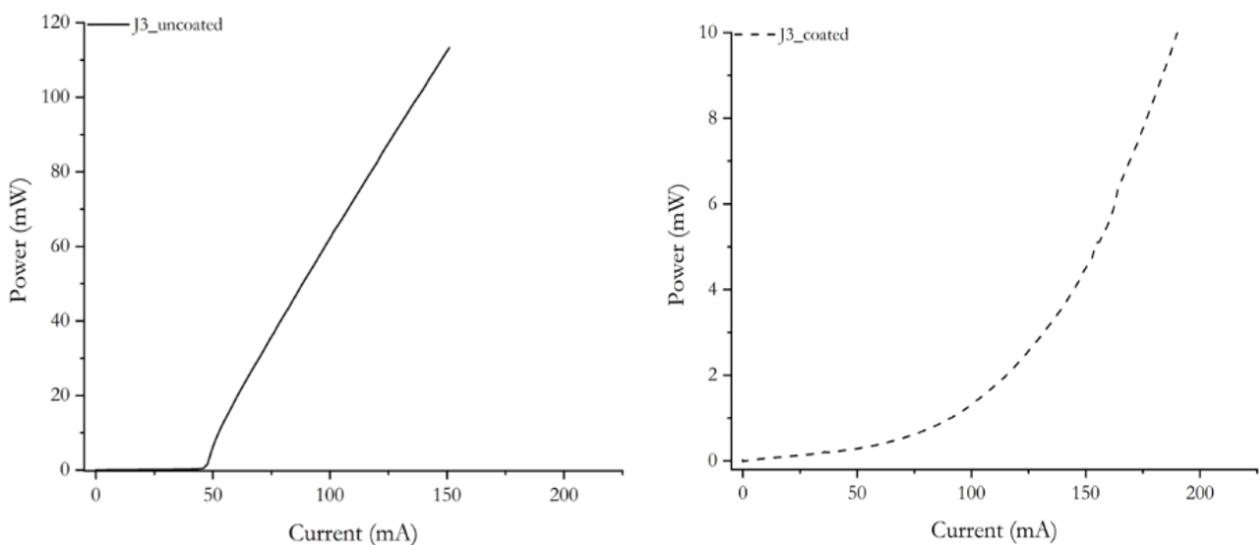
Figures 5.2.1: Pulsed current P-I curve for device J3. The uncoated device (solid line) and both facets coated (dashed line).

After the TaO_x thin film is applied (dashed line), we see a gradual increase in output power as the injection current increases. At current values below 100 mA, the P-I relationship is characteristic of spontaneously emitted photons, but as the injection current is increased further, we see a more exponential increase in output power, but the total output power is still noticeably lower than that of the uncoated device. The behaviour seen at higher currents is typically associated with that of ASE, which is discussed in Chapter 2.

The P-I characteristics are the first indication that the coating has been effective in inhibiting lasing. However, since the coated devices are no longer lasing, up to the point of gain saturation, it is difficult to infer $\sqrt{R_1 R_2}$ from a plot of gain threshold, G_{th}, versus cavity length. To evaluate the coated facet reflectivity, direct measurements of the emission spectrum of the coated devices is necessary.

5.2.2 Device Emission Spectrum

To quantitatively analyse the change in facet reflectively after the application of the TaO_x coating, it is necessary to measure the intensity, and bandwidth of the emitted light from both Facet 1 and 2, before and after coating – depicted in Figure 5.2.2 (a) and (b), respectively. Figure 5.2.2 (a) shows the emission spectrum of J3 before coating. A signal modulation depth $m = 1$ is observed, which is consistent with lasing behaviour, as previously mentioned. The centre wavelength of sample J3 is 1568.83 nm ± 0.02 nm.
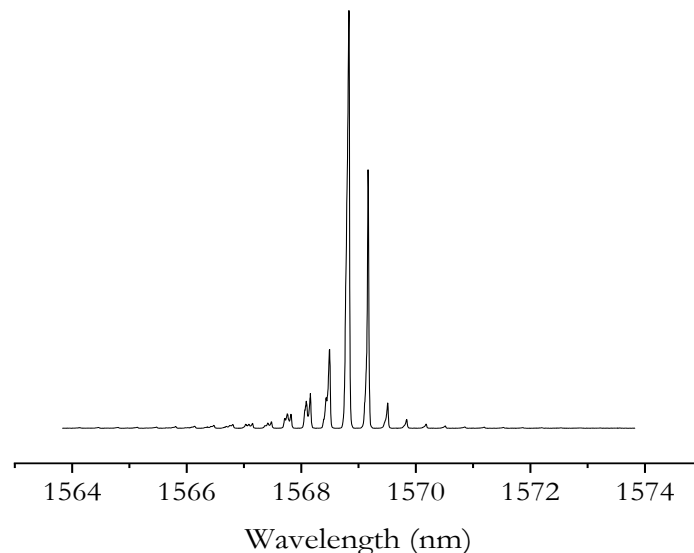
Figures 5.2.2 (a): Measured spectrum for device J3 uncoated at lasing threshold, $I_{th} = 46$ mA, $T = 25°C$.

After the coating is applied, the emission spectrum is re-measured, first at the original I_{th}, and then subsequently at increased injection currents. Figure 5.2.2 (b) shows the spectrum of J3 after coating, where it is evident that device is no longer lasing at the original threshold current of 46 mA. What we now observe is a set of broadband peaks, spanning approximately 60-100 nm, across the normalised current range. The injected current increases the carrier density in the conduction band, where the electrons are free to occupy any one of the wide range of available energy levels. Consequently, electron-hole recombination leads to the spontaneous emission of photons with a broad range of energies [3-4] which are amplified by the gain medium as they travel along the cavity. Most of the light exits at facet instead of being reflected which is a direct consequence of the TaO_x coating. This gives rise to the ASE spectrum seen below, which spans a broad range of wavelengths that coincide with the emitted photons with many optical frequencies – lasing has been suppressed.
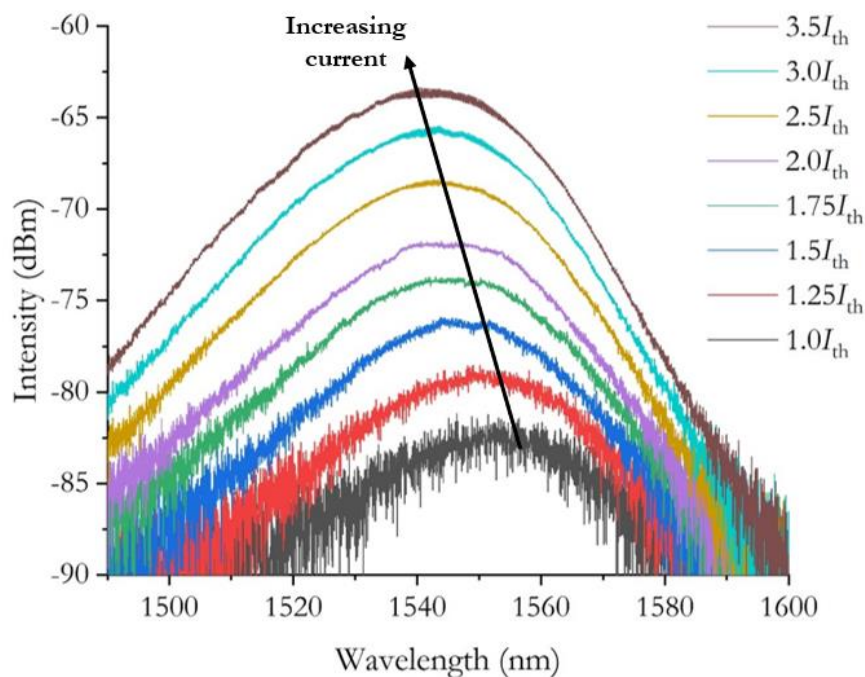
Figures 5.2.2 (b): Measured spectrum for device J3 after both Facet 1 and Facet 2 are coated. Device is measured as a function of normalised current, $\frac{I}{I_{th}}$, where the uncoated lasing threshold current, I_{th}, is 46 mA.

When higher values of current are injected into the device, the ASE spectrum broadens and the peak of the ASE shifts to shorter wavelengths, as indicated by the solid black arrow in Figure 5.2.2(b). These observations can be explained by the band filling effect [5] which is a consequence of increased carrier concentration in the device. Recalling from chapter 2, the probability of a photon, of a given energy, being emitted depends upon the number of energy states available close to the photon energy (DOS) as well as the number of carriers available to

populate those states. At lower pump currents, the carriers populate the states closest to the band edges, and therefore there is an increased probability of emission of photons closest to the band gap E_{g}, of the material, which corresponds to the longer wavelength ASE peak of 1552 nm, seen at $1.0I_{\mathrm{th}}$. However, as the injection current increases, so does the electron density of the conduction band, where, due to the Pauli exclusion principle, these electrons are forced to occupy states of higher energy. This leads to the increased probability of the emission and amplification of photons with of a higher energy, thus shorter wavelengths, and therefore at $3.5I_{\mathrm{th}}$ the peak of the ASE is at approximately 1541 nm.

A lower facet reflectivity suppresses the optical feedback within the cavity, up to and including current values of $3.5I_{\mathrm{th}}$. It is evident that lasing has been suppressed in sample J3, but as discussed previously, it is incredibly challenging to achieve $\sqrt{R_1 R_2}=0$ and therefore some light is coupled back into the waveguiding region of the TW-SOA, giving rise to the "ripples" seen across the ASE spectrum. Figure 5.2.3 shows the ASE spectrum of J3 across the C-Band region where the remaining resonances are most distinguishable.
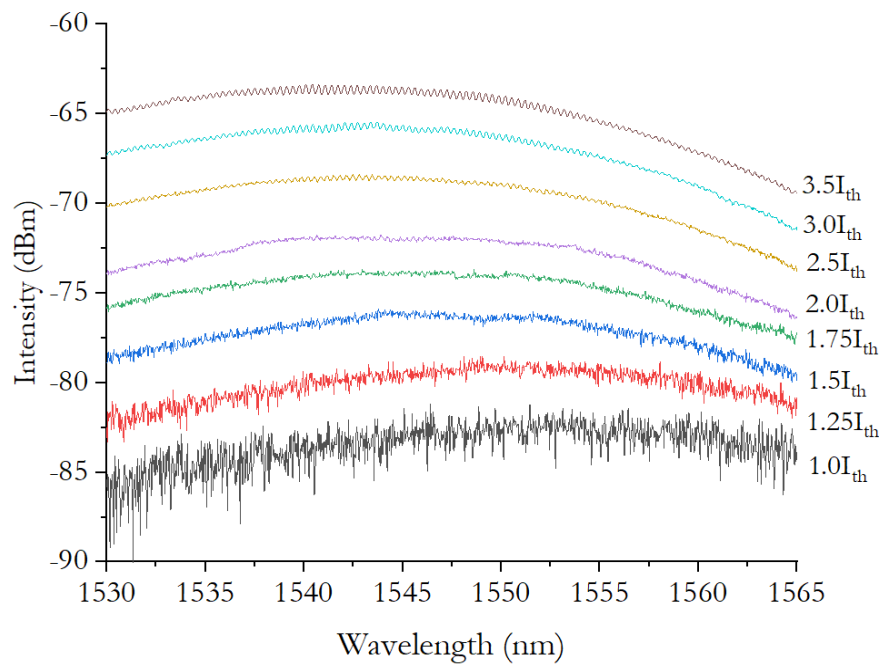
Figures 5.2.3: ASE spectrum of J3 (coated) as a function of normalised current across the C-Band region. Note the difference in depth of the "ripples" across the various wavelengths.

Resolving the peaks and troughs in the plotted data allows the depth of the modulated optical signal, m, and thus the roundtrip amplification factor, a, to be calculated for each of the normalised currents. These values can be used to calculate the geometric mean facet reflectivity, $\sqrt{R_1 R_2}$, for the coated TW-SOA device.

5.2.3 SOA Gain Ripple

The gain ripple, G_r, of an SOA is related to the effectiveness of the chosen mechanism for reducing cavity resonances. In the case of sample J3, the observed values of G_r are linked to the performance of the ARC. If the coating is not optimised for the device operation wavelength, back reflections of light will give rise to larger gain ripple across the emission spectrum, depleting the single pass gain and reducing the gain bandwidth of the optical amplifier [6].

For the uncoated devices, at the point of lasing, the difference between the maximum and minimum points for the modulated signal is unity. This is typical behaviour for F-P lasers. Measuring the difference in the amplitude of the resonant and anti-resonant feature in the ASE spectrum of the coated TW-SOA, we obtain values for the gain ripple of sample J3 over the C-Band region. Table 5.2 summarises the measured values of gain ripple, G_r, as a function of wavelength. The minimum and maximum values are quoted for injection current values where cavity resonances first become visible, and where they are most prominent, i.e., where the injection current is a maximum.

Table 5.2: Minimum and maximum values of gain ripple for device J3 as a function of wavelength. Periodicity or ripples is 0.3 nm ± 0.05 nm.

Wavelength (nm)	G_r minimum (dB)	G_r maximum (dB)
1530	0.1	0.2
1540	0.05	0.5
1550	0.04	0.5
1560	0.02	0.3

Previous work has shown the development of SOAs with gain ripple <0.1 dB and facet reflectivity's around 10^{-4} which have demonstrated single pass gain, G_s, of 20-30 dB [7]. When impressively low facet reflectivity values are reached (10^{-5}) the gain ripple is lower and therefore single pass gain values in the region of $40\ dB$ may be possible. Commercially available SOAs have typical gain ripple values around 0.1-.02 dB, with a maximum of 0.5 dB [8] but these typically rely on double-layer coatings such as TiO_2/SiO_2 or even multiple layers of Si_4N_4/SiO_2. This would imply that a single layer TaO_x AR-coating could be used to produce C-Band SOAs with competitively low gain ripple, that could outperform some of the already commercially available products.

5.2.4 SOA Facet Reflectivity

The coated facet reflectivity of device J3 can be determined by using the method outlined in subsection 2.4 **[9]**. To begin, the modulation depth, m, is extracted from the remaining F-P fringes for each of the injection current values and using equation (2.17) the roundtrip amplification factor, a, is subsequently calculated. Table 5.3 shows the calculated values for m and a at a wavelength of 1550 nm, for each of the normalised current values. When there is little to no optical feedback within the cavity, particularly at low injection currents, the modulation depth of the F-P fringes is negligible. Therefore, the values presented in the Table 5.3 are for current values above the original threshold current of the uncoated device J3.

Table 5.3: Calculated values of m and a for J3 (coated) as a function of normalised current at $\lambda = 1550$ nm. $a = 1$ for the uncoated device at and above I_{th}.

Normalised current $\left(\frac{I}{I_{\text{th}}}\right)$	m	a
1.5	0.0018	0.0009
1.75	0.003	0.0015
2.0	0.005	0.003
2.25	0.01	0.005
2.5	0.02	0.01
3.0	0.04	0.02
3.5	0.06	0.03

When device J3 is under electrical injection, the spontaneously generated optical field travelling between the coated facets with reflectivity R_1 at Facet 1 and R_2 at Facet 2, will experience a logarithmic power gain, and therefore, a plot of $\ln|a|$ as a function $\frac{I}{I_{\text{th}}}$ allows us of to extract the coated facet reflectivity of the TW-SOA, that is $\sqrt{R_1 R_2}$ when $\frac{I}{I_{\text{th}}}$ is extrapolated to zero. Figure 5.2.4 shows the plotted data from Table 5.3. There is some scatter amongst the data points at lower normalised current values, this is due to very little feedback of reflected light at low injected carrier densities. This gives an indication of the effectivness of the TaO_x AR coating at 1550 nm since there are very few F-P fringes at at this wavelength, leading to a flatter ASE spectrum for lower injection currents, it could be concluded that the ARC has been effective in significanlty reducing the feedback of light at 1550 nm.
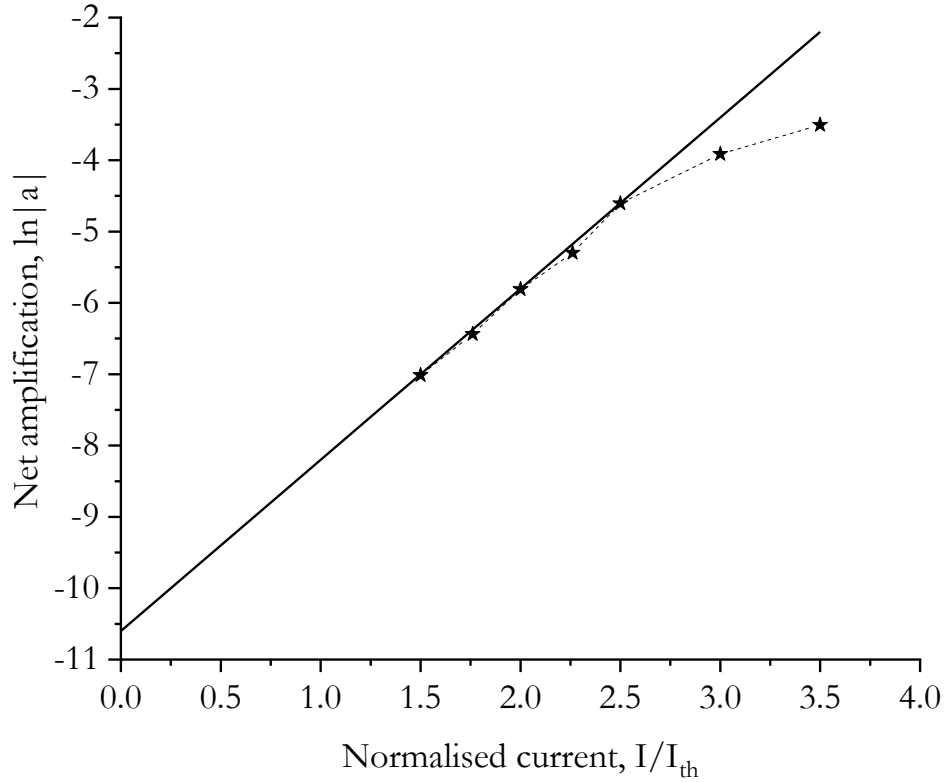
Figures 5.2.4: $\ln|a|$ versus $\dfrac{I}{I_{th}}$ for calculated values of roundtrip amplification, $|a|$, (from Table 5.2) at 1550 nm where $I_{th} = 46$ mA and $R_l = 0.28$ for the uncoated device. The equation of the fit (solid line) is $\ln|a| = 2.41\dfrac{I}{I_{th}} - 10.61$.

Figure 5.2.4 shows that for current values up to and including $2.5I_{th}$ there is a linear increase in $|a|$ with current. As the injection current is increased further, we begin to see a non-linear realtionship in the data where the dashed line starts to "roll-over" - this behaviour can be explained by gain saturation **[10]**. Below the saturation point, the amplitude of the rountrip oscillations within the optical cavity increases with increasing current and therefore we observe a linear increase in gain. However, under high current injection, the gain starts to saturate which reduces the number of photons trasmitted at ouput facet of the SOA and therfore less light (at 1550 nm) is detected by the Optical Spectrum Analyser (OSA). The amplitude of the ripples seen in the ASE spectrum no longer increase proportionally with injection current.

To calculate the coated facet reflectivity of the SOA, it is imporant to focus on the linear region of Figure 5.2.4, and omit from the fitting procedure the data points where gain stauration is present. To find a value of $\sqrt{R_1 R_2}$ for J3 at 1550 nm, we recall from subsection 2.4 that the line in Figure 5.4.2 is given by equation (5.2) below,

$$\ln|a| = (\gamma L_c)\frac{I}{I_{th}} - \left(\gamma L_c - \ln\frac{\sqrt{R_1 R_2}}{R_l}\right) \tag{5.2}$$

when $\frac{I}{I_{th}} = 0$ equation (5.2) reduces to

$$\ln|a| = -\left(\gamma L_c - \ln\frac{\sqrt{R_1 R_2}}{R_l}\right) \tag{5.3}$$

Rearranging equation (5.3) gives an expression for the coated facet reflectivity $\sqrt{R_1 R_2}$ assuming $R_1 = R_2$

$$\sqrt{R_1 R_2} = (e^{-10.61 + \gamma L_c} \times R_l) \tag{5.4}$$

where the value $\ln|a| = -10.61$ is found from the intercept at $\frac{I}{I_{th}} = 0$, $\gamma = 24$ cm^{-1} is the power gain coefficient and is found from the slope of the curve in Figure 5.2.4, $L_c = 0.1$ cm is the length of the cavity, and $R_l = 0.28$ is the facet reflectivity of the uncoated laser diode.

Inputting the data above into equation (5.4) we find that the coated facet reflectivity, at 1550 nm, is $\sqrt{R_1 R_2} = 7.7 \times 10^{-5}$ which confirms that the TaO_x has been successful in significantly reducing the optical feedback of light at the desired wavelength. The procedure above is repeated to find the reflectivity of device J3 across the C-Band region. At wavelengths of 1540 and 1560 nm, the reflectivity values are 2.0×10^{-4} and 6.0×10^{-5}, respectively. The F-P fringes are much less defined at 1530 nm and therefore, there were not enough datapoints on the plot of $\ln|a|$ versus $\frac{I}{I_{th}}$ to give an accurate value of reflectivity at 1530 nm.

The error associated with the quoted values of $\sqrt{R_1 R_2}$ at 1540-1560 nm, arise from the fitting of the F-P fringes in the ASE spectrum. Below values of $1.75 I_{th}$ typically the spectrum is flatter, and therefore m is very small, and more difficult to fit. This leads to an increased error in a and therefore $\ln|a|$ at smaller values of injection current. This could lead to some deviation in the fitting of datapoints in the plot of $\ln|a|$ versus $\frac{I}{I_{th}}$. The fitting procedure for the error calculation is detailed in Appendix D. The possible maximum and minimum reflectivity values, due to this error, can be found in Table 5.4 below.

Table 5.4: Maximum and minimum values of $\sqrt{R_1 R_2}$ due to an induced error in m from fitting rippled in ASE spectrum of device J3.

Wavelength (nm)	Maximum $\sqrt{R_1 R_2}$	Measured $\sqrt{R_1 R_2}$	Minimum $\sqrt{R_1 R_2}$
1540	3.4×10^{-4}	2.0×10^{-4}	1.5×10^{-4}
1550	1.8×10^{-4}	7.7×10^{-5}	1.1×10^{-5}
1560	1.3×10^{-4}	6.0×10^{-5}	2.0×10^{-5}

The values presented in Table 5.4 shows that the TaO_x has been effective in suppressing optical feedback across the C-Band region, where the measured value of $\sqrt{R_1 R_2}$ at 1540 nm is very close to original target value specified in subsection 3.4 (1.2×10^{-4}) and even lower at 1550 nm and 1560 nm. Taking into consideration the error in the fitting procedure, the maximum values of the reflectivity remain very close to the target value, but the reflectivity is slightly higher than the target value at 1540 nm. The TaO_x coating was designed to have a minimum of reflectivity centred at 1550 nm, but it can be seen from Table 5.4 that the minimum is closer to 1560 nm than 1550 nm. This observation is explored further in the following subsections of this chapter.

5.3 Measured Reflectivity versus Modelled Reflectivity

The experimentally extracted values of reflectivity are compared with the values obtained during the planewave simulations detailed in Chapter 3. Similarities in the two datasets are shown in the following section as well as a discussion of how deviations from the target values of thickness and/or refractive index of the TaO_x thin film could be responsible for the variation between the measured and simulated values of reflectivity.

5.3.1 Comparing Experimental and Simulated Reflectivity

Figure 5.3.1 shows the simulated planewave reflectivity, as a function of wavelength, for a thin film of $n_{film} = 1.80$ and a thickness of $d = 215$ nm on a substrate of $n_{eff} = 3.24$. The datapoints positioned near the solid curve are the experimental values of $\sqrt{R_1 R_2}$ extracted using the procedure outlined section 5.2.4. Although there is some discrepancy between the simulated and measured values, it is evident that the deposited AR coating shows good anti-reflective properties around the wavelength region of interest.
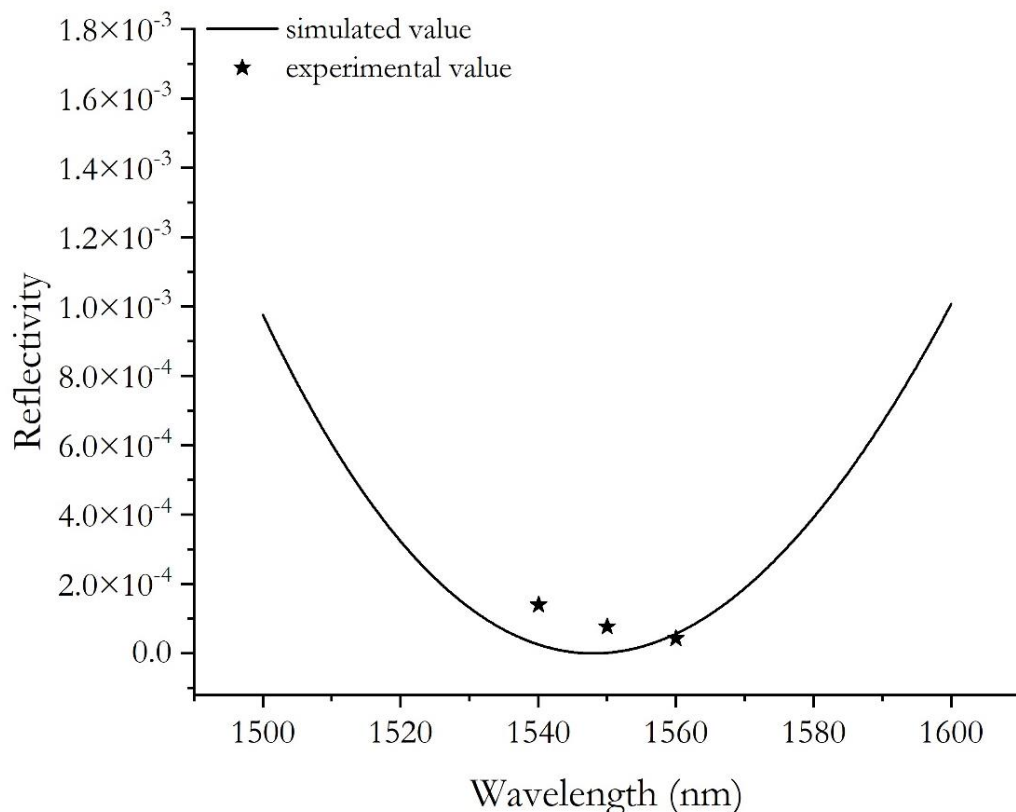
Figures 5.3.1: Reflectivity as a function of wavelength. Solid line indicates simulated data with $n_{film} = 1.80$ and $d = 215$ nm. Datapoints are experimentally measured values.

As Figure 5.3.1 suggests, although there are similarities in the experimental and *ideal* simulated values of reflectivity, the values do not perfectly match. The experimental data appears to lie along a curve where the minimum is positioned towards the longer wavelength region, rather than being centred at 1550 nm. The measured $\sqrt{R_1 R_2}$ value is greater at shorter wavelengths. At 1540 nm this is 2.0×10^{-4} and at 1550 nm 7.7×10^{-5} – these values sit further from the ideal simulated values (solid black line). To try to identify the cause for the difference between the experimental reflectivity data and that of the original simulated data in Chapter 3, additional simulation work is conducted. One possibility is that the TaO_x film thickness is different to the target value. Figure 5.3.2 and show the experimental and simulated data from Figure 5.3.1, but with the addition of simulation data for a constant film refractive index but varying film thickness.
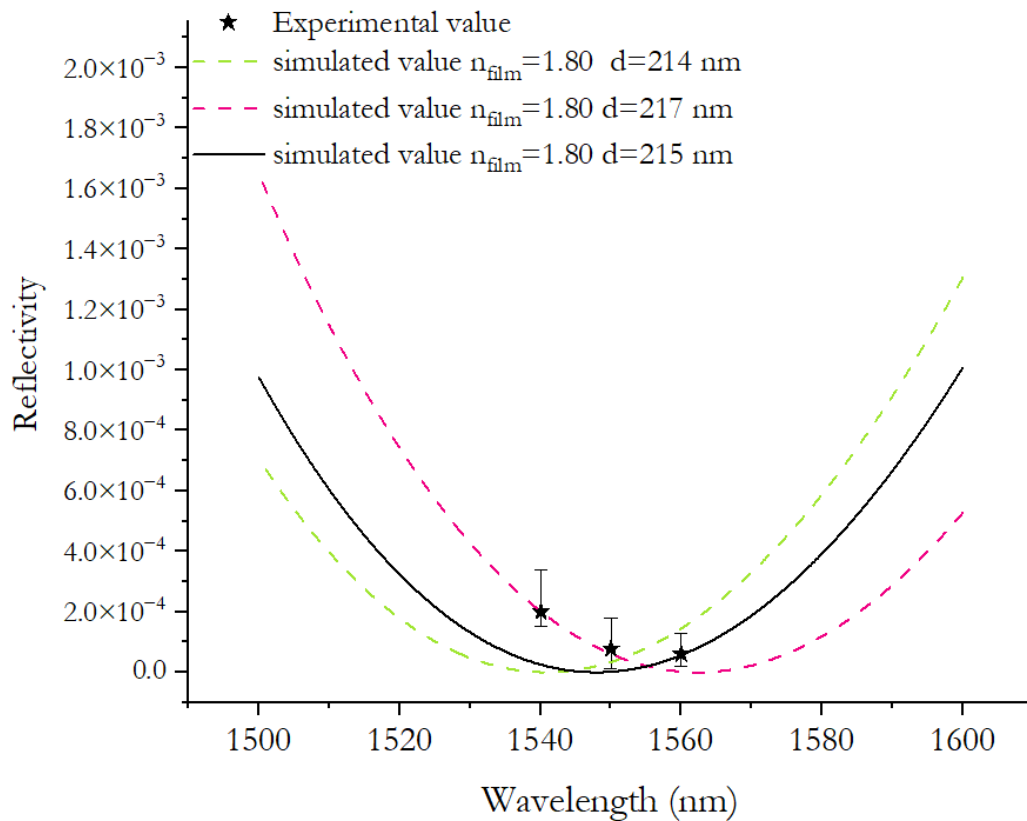
Figures 5.3.2: Reflectivity as a function of wavelength for both experimental and simulated data. $n_{film} = 1.80$ and varying film thickness, d.

Figure 5.3.2 shows good agreement between the experimental data and the simulated data for a film of thickness $d = 217$ nm (pink dashed line). The experimentally measured values of reflectivity at 1540 nm and 1550 nm are very similar to the simulated datapoints and sit within the error bars. There is a small difference between measured and simulated reflectivity values at

1560 nm and the simulated value sits just outside the minimum error bar at this wavelength. However, it is possible that the film thickness could be slightly thicker than the target value since there may have been a very short delay between the crystal monitor detecting that the target thickness has been reach and the shutter triggering to cover the sample from the source material. The data in Figure 5.3.2 shows that it is less likely that the deposited film is thinner than the target value, since the experimental and simulated values of reflectivity are only similar around 1550 nm. It is worth noting that a different film thickness is not the only possibility for the observation seen in the experimental data, and therefore it is sensible to explore the possibility that the deposited film has a different refractive index than the target value.

Figure 5.3.3 shows the experimental values of reflectivity as a function of wavelength, but this time the simulated values have a constant film thickness of $d = 215$ nm but different values of refractive index.

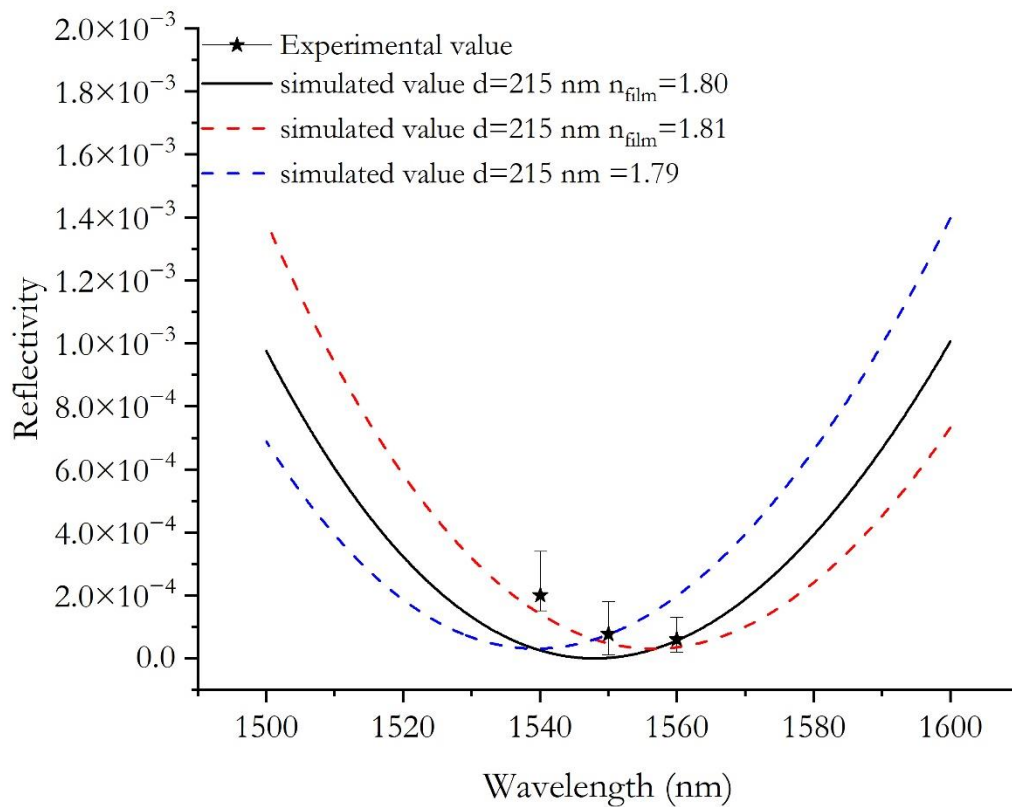
Figures 5.3.3: Reflectivity as a function of wavelength for both experimental and simulated data. $d = 215$ nm and varying film refractive index, n_{film}.

The simulated data in Figure 5.3.3 would imply that small changes in refractive index can lead to a shift in reflectivity minima by about 10 nm – that is, when $n_{film} = 1.79$ the minimum is shifted to 1540 nm, and for $n_{film} = 1.81$ it is shifted to 1560 nm. When $n_{film} = 1.79$ and

$n_{film} = 1.81$ there is good agreement between the measured and simulated values of reflectivity at 1550 nm. However, at both 1540 nm and 1560 nm, there is better agreement between the experimental and simulated values when the refractive index of the film is higher ($n_{film} = 1.81$) compared with the lower index films ($n_{film} = 1.79$ and $n_{film} = 1.80$) where these values differ more considerably. This implies that the TaO_x film deposited onto sample J3 could have a higher refractive index than the targeted value, giving rise greater destructive interference of light of longer wavelengths and therefore the ripples seen at 1560 nm have a much smaller amplitude than those seen at shorter wavelengths. The cause of the higher refractive index could originate from fluctuations in oxygen flow rate, thus chamber pressure, during the deposition. If the chamber pressure drops below the ideal value, then as detailed in Chapter 4, a film of higher packing density, and therefore higher refractive index can form [11]. This seems plausible since it is somewhat challenging to control the chamber pressure to the precision required to consistently produce a film of refractive index with an error less than 0.01.

Figures 5.3.2 and 5.3.3 show that it is reasonable to assume that the ARC deposited onto sample J3 could be thicker or have a higher refractive index than the target values, since there is good agreement between the experimental and simulated data. However, it is worth considering other possibilities that may impact the performance TaO_x coating. One such possibility is the formation of an interfacial oxide between the semiconductor facet and TaO_x layer [12]. Recalling that the layers within the structure contain aluminium, which has an affinity for oxygen, this likelihood cannot be ruled out, and consequently when light is emitted from the device it encounters the aluminium oxide layer first, undergoing refraction and a possible phase shift before it even passes through the tantalum oxide layer. This could lead to an insufficient phase difference between the light reflected at the back and front surfaces of the film and therefore more light coupling back into the waveguide of the TW-SOA. Another possibility is that the TaO_x film is inhomogeneous throughout the 215 nm thickness. The samples presented in this work did not undergo applied (intentional) heating, to keep the sample temperature constant during the evaporation process but the samples may experience a variation in temperature throughout the deposition due to the heating effects of the electron gun. The temperature difference between sample and TaO_x material over the duration of the evaporation could lead to the formation of a film with a graded refractive index in the direction of growth instead of a single ideal refractive index. Of course, it could be a case that the observed TW-SOA device characteristics are a consequence of more than one of the possibilities mentioned above, and therefore further work could be done to narrow this window of uncertainty.

Chapter 5 References

[1] P. Blood, "Quantum Confined Laser Devices," *Oxford Uni. Press.* pp. 240-241, 2015.

[2] N. Deepal, "Characterisation of Lateral Carrier Out-Diffusion and Surface Recombination in Ridge Waveguide Devices," PhD thesis, Cardiff University, 2009.

[3] M. Summerfield, "Optical Amplifiers (Semiconductors)", Encyclopedia of Physical Science and Technology, pp. 221-223, 2003.

[4] W. W. Chow and R. R. Craig, "Amplified spontaneous emission effects in semiconductor laser amplifiers," in *IEEE Journal of Quantum Electronics*, vol. 26, no. 8, pp. 1363-1368, Aug. 1990, doi: 10.1109/3.59683.

[5] R. Nagarajan, T. Kamiya and A. Kurobe, "Band filling in GaAs/AlGaAs multiquantum well lasers and its effect on the threshold current," in *IEEE Journal of Quantum Electronics*, vol. 25, no. 6, pp. 1161-1170, June 1989, doi: 10.1109/3.29242.

[6] J.Ann. Constable, "Semiconductor optical amplifiers for analogue applications", PhD thesis, University of Bath, 1993.

[7] K. Sato and X. B. Zhang,"Semiconductor optical amplifier and gain chip used in wavelength tunable lasers," *ZTE Communications*, vol. 19, no. 3, pp. 81–87, Sept. 2021

[8] Thorlabs, C-Band Optical Amplifiers (BOAs and SOAs), 1550 nm, https://www.thorlabs.com/newgrouppage9.cfm?objectgroup_id=3901, accessed on 30/05/2023.

[9] I. Kaminow, G. Eisenstein and L. Stulz, "Measurement of the modal reflectivity of an antireflection coating on a superluminescent diode," in *IEEE Journal of Quantum Electronics*, vol. 19, no. 4, pp. 493-495, April 1983, doi: 10.1109/JQE.1983.1071887.

[10] O.M. Kharraz, A.S.M. Supa'at, A. Atieh, A.K. Zamzuri, and M.A. Mahdi, "Enhanced gain saturation model of non-linear semiconductor optical amplifiers", *IET Optoelectronics,* Vol.12, No.6, 2018.

[11] Seouk-Hoon Woo, Chang Kwon Hwangbo, Young Bae Son, Il Choon Moon, Geon Mo Kang, and Kwang-Su Lee, "Optical Properties of Ta_2O_5 Thin Films Deposited by Plasma Ion-Assisted Deposition", *Journal of Korean Physical Society,* Vol. 46, pp. S187-S191, June 2005.

[12] R. Drevet, P. Souček, P. Mareš, M. Dubau, Z. Czigány, K. Balázsi, and P. Vašina, "Multilayer thin films of aluminum oxide and tantalum oxide deposited by pulsed direct current magnetron sputtering for dielectric applications", Vacuum, Volume 210, April 2023. https://doi.org/10.1016/j.vacuum.2023.111870.

Chapter 6
Conclusion and Future Work

6.1 Conclusion

The work in this thesis studies the feasibility of using tantalum oxide, TaO_x, as a single layer AR coating to suppress optical feedback in C-Band (1530-1565 nm) TW-SOAs. The results presented throughout suggest it is possible to achieve a TaO_x coating that significantly reduces the facet reflectivity of laser devices to realise a competitively low gain ripple TW-SOA operating over the wavelength region of interest.

A TaO_x thin film, with the desired optical properties, is successfully deposited onto cleaved facets of single mode $Al_xGa_yIn_{1-x-y}As/InP$ RWG laser diodes via e-beam evaporation. The refractive index of the film is tuned to meet the target value, $n_{film} = \sqrt{n_{eff}}$, by exploiting the measured relationship between film refractive index and the evaporator chamber pressure. The chosen deposition technique allows both facets to be coated with a film thicker than 200 nm at a rate of 0.15 nm/s.

The emission spectrum of the coated devices is consistent with that of ASE which demonstrates the TaO_x film has stopped lasing in the devices. The modulation depth of the remaining F-P fringes indicates that the coated facet reflectivity is 10^{-4} at 1540 nm and even lower (10^{-5}) at 1550 and 1560 nm, with the minimum centred at 1560 nm. The TW-SOA exhibits a minimum gain ripple, G_r, value of <0.1 dB with the maximum being 0.5 dB, both with a periodicity of 0.3 nm $\pm$ 0.05 nm. However, comparing the experimental and simulated data leads us to believe the deposited film may have a different optical path length than the target value, arising from a variation in film refractive index and/or thickness. A thicker film ($d = 217$ nm) or film of higher refractive index ($n_{film} = 1.81$) could've been deposited onto sample J3 which, as shown in Chapter 5, leads to the minimum of the reflectivity curve shifting to a longer wavelength (1560 nm) resulting in a higher reflectivity value at 1550 nm.

The differences observed in the experimental and the simulated values of reflectivity could be a consequence of the deposition technique, in particular a variation in film packing density, and thus refractive index, due to pressure fluctuations in the evaporator chamber throughout the coating process. It is plausible that the coating thickness could be different from the target value since there can be a $\pm$ 3 nm error in deposited film thickness using this technique. However, it is worth noting that there are other possibilities to consider, including the formation of an

inhomogeneous coating with a graded refractive index in the direction of growth; or even the formation of an interfacial oxide between the device facets and TaO_x layer.

6.2 Future Work

Further research could be carried out to test the repeatability of the work outlined in this thesis. At the time of writing, only a small number of devices have been coated and shown performance consistence with sample J3, therefore it is necessary to coat a larger number of samples to ensure the process can be repeated and produce the same standard of coating. The number of devices coated per evaporation was limited to the holder used to affix the samples to the plate in the evaporator chamber. It would seem worthwhile to increase the number of samples per evaporation to determine the effect of changes in sample position relative to the Ta_2O_5 source.

Additional work could be carried out to understand the origin of the higher values of gain ripple observed at 1550 nm since a higher film refractive index and/or thickness are not the only possibility. Carrying out more depositions could provide a better understanding of whether the issues can be mitigated by altering chamber conditions during the evaporation or whether further optimisation does not lead to an improved film quality and therefore the film optical properties are limited by the deposition technique. Since the facet is exposed to an oxygen-rich environment throughout the evaporation, the formation of an interfacial aluminium oxide layer is plausible and therefore facet passivation could be carried out prior to application of the TaO_x layer to see if this reduces the noise in the SOA spectrum. Heat emitted from the electron gun during the evaporation of metal-oxide films can lead to the formation of a film which has a refractive index that is inhomogeneous in the direction of growth. This is typically controlled by heating of the sample/substrate during the evaporation. The samples in this work were not subjected to substrate heating during coating process and therefore could be vulnerable to this issue and therefore it is worthwhile to investigate the impact of sample heating on the optical properties of the TaO_x film.

Different coating techniques could be explored, such as sputtering, which would still allow the refractive index of the TaO_x film to be tuned by controlling gas flow rates during the deposition but may allow the refractive index and thickness of the film to be controlled with greater precision. Additionally, sputtering can be advantageous because this technique can be more effective when coating samples with complex geometries, unlike e-beam evaporation which is a non-conformal and directional coating technique.

Appendix A

Deriving equation (2.17) from subsection 2.4

$$P(\lambda) = P_z(1 - R_1)|1 - a|^{-2}$$

$$a = \sqrt{R_1 R_2}\, e^{2j\beta L} e^{\frac{1}{2}(G_+ + G_+)}$$

$$|1 - a|^{-2} = (1 - \sqrt{R_1 R_2}\, e^{2j\beta L} e^{\frac{1}{2}(G_+ + G_=)} \cos(2\beta L))^2 + R_1 R_2 e^{(G_+ + G_+)} \sin^2 2\beta L$$

$$= 1 - 2\sqrt{R_1 R_2}\, e^{2j\beta L} e^{\frac{1}{2}(G_+ + G_+)} \cos(2\beta L) + R_1 R_2 e^{(G_+ + G_+)} \cos^2(2\beta L) + \sin^2(2\beta L).$$

$$= 1 + |a|^2 - 2|a| \cos(2\beta L).$$

The maximum value of $|1 - a|^2$ is when $\cos(2\beta L) = 1$ that is when $2\beta L = \pi$ and the minimum value of $|1 - a|^2$ is when $\cos(2\beta L) = -1$ that is when $2\beta L = 2\pi$.

The output power at the facet is given by $P \propto \frac{1}{|1-a|^2}$, therefore $P_{\max}$ is when $2\beta L = 2\pi$ and $P_{\min}$ is when $2\beta L = \pi$. Substituting this into equation (2.16) gives

$$m = \frac{P_{\max} - P_{\min}}{P_{\max} + P_{\min}}$$

$$= \frac{\dfrac{1}{1 + |a|^2 + 2|a|} - \dfrac{1}{1 + |a|^2 - 2|a|}}{\dfrac{1}{1 + |a|^2 + 2|a|} + \dfrac{1}{1 + |a|^2 - 2|a|}} \times \frac{(1 + |a|^2 + 2|a|)(1 + |a|^2 - 2|a|)}{(1 + |a|^2 + 2|a|)(1 + |a|^2 - 2|a|)}$$

$$= \frac{(1 + |a|^2 - 2|a|) - (1 + |a|^2 + 2|a|)}{(1 + |a|^2 - 2|a|) + (1 + |a|^2 + 2|a|)}$$

$$= \frac{4|a|}{2 + 2|a|^2}$$

$$= \frac{2|a|}{1 + |a|^2}.$$

Appendix B

(a)   TE$_{00}$ mode 1.6 µm ridge width

(b)   TE$_{10}$ mode 1.6 µm ridge width

(c)   TE$_{00}$ mode 1.8 µm ridge width

(d)   TE$_{10}$ mode 1.8 µm ridge width

(e)   TE$_{00}$ mode 2.0 µm ridge width

(f)   TE$_{10}$ mode 2.0 µm ridge width

(g)   TE$_{00}$ mode 3.0 µm ridge width

(h)   TE$_{10}$ mode 3.0 µm ridge width
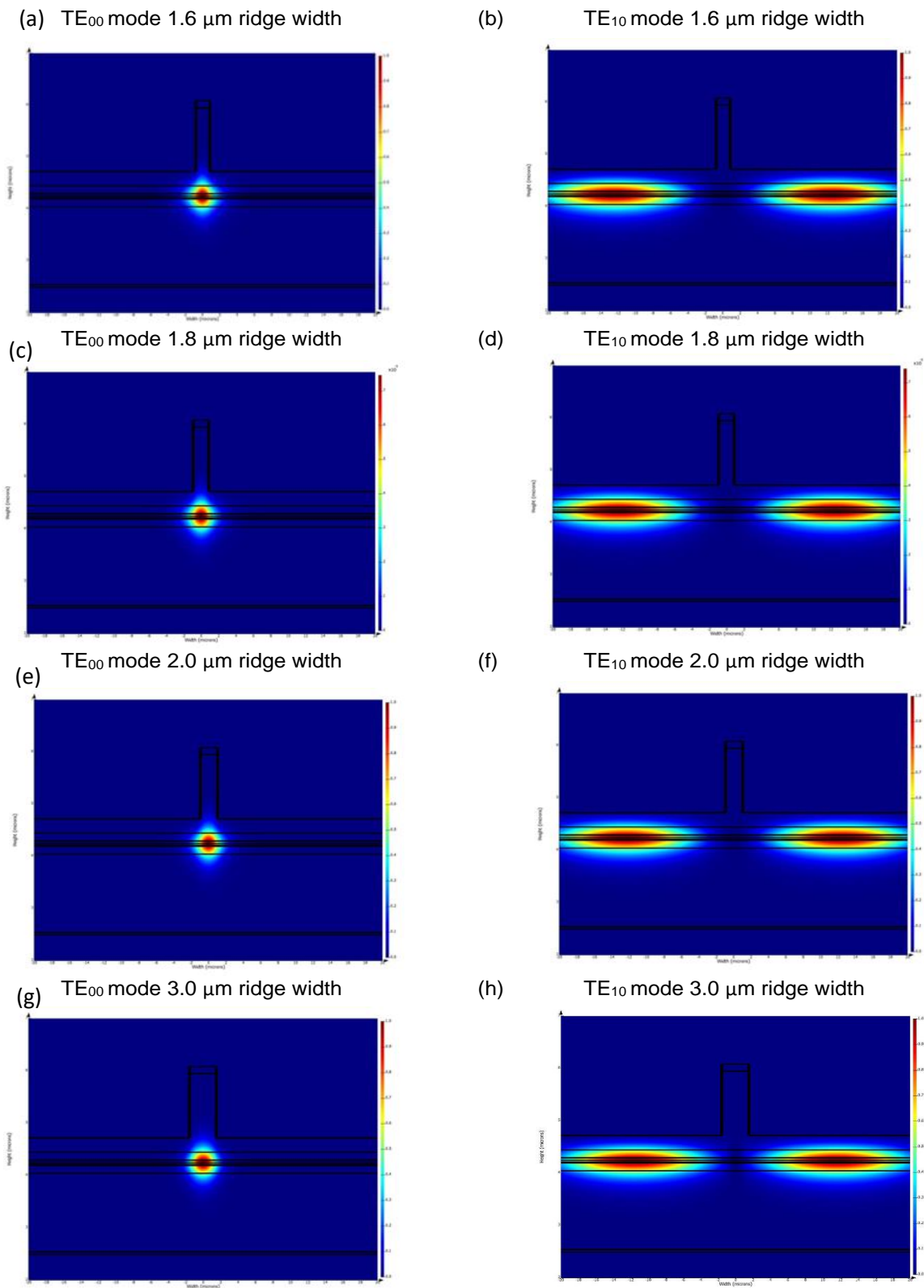
Figure B1(a-h): FDE simulation for shallow-etch quantum well structure with varying ridge waveguide width.

(a)   TE$_{00}$ mode 1.6 µm ridge width   (b)   TE$_{10}$ mode 1.6 µm ridge width

(c)   TE$_{00}$ mode 1.8 µm ridge width   (d)   TE$_{10}$ mode 1.8 µm ridge width

(e)   TE$_{00}$ mode 2.0 µm ridge width   (f)   TE$_{10}$ mode 2.0 µm ridge width

(g)   TE$_{00}$ mode 3.0 µm ridge width   (h)   TE$_{10}$ mode 3.0 µm ridge width
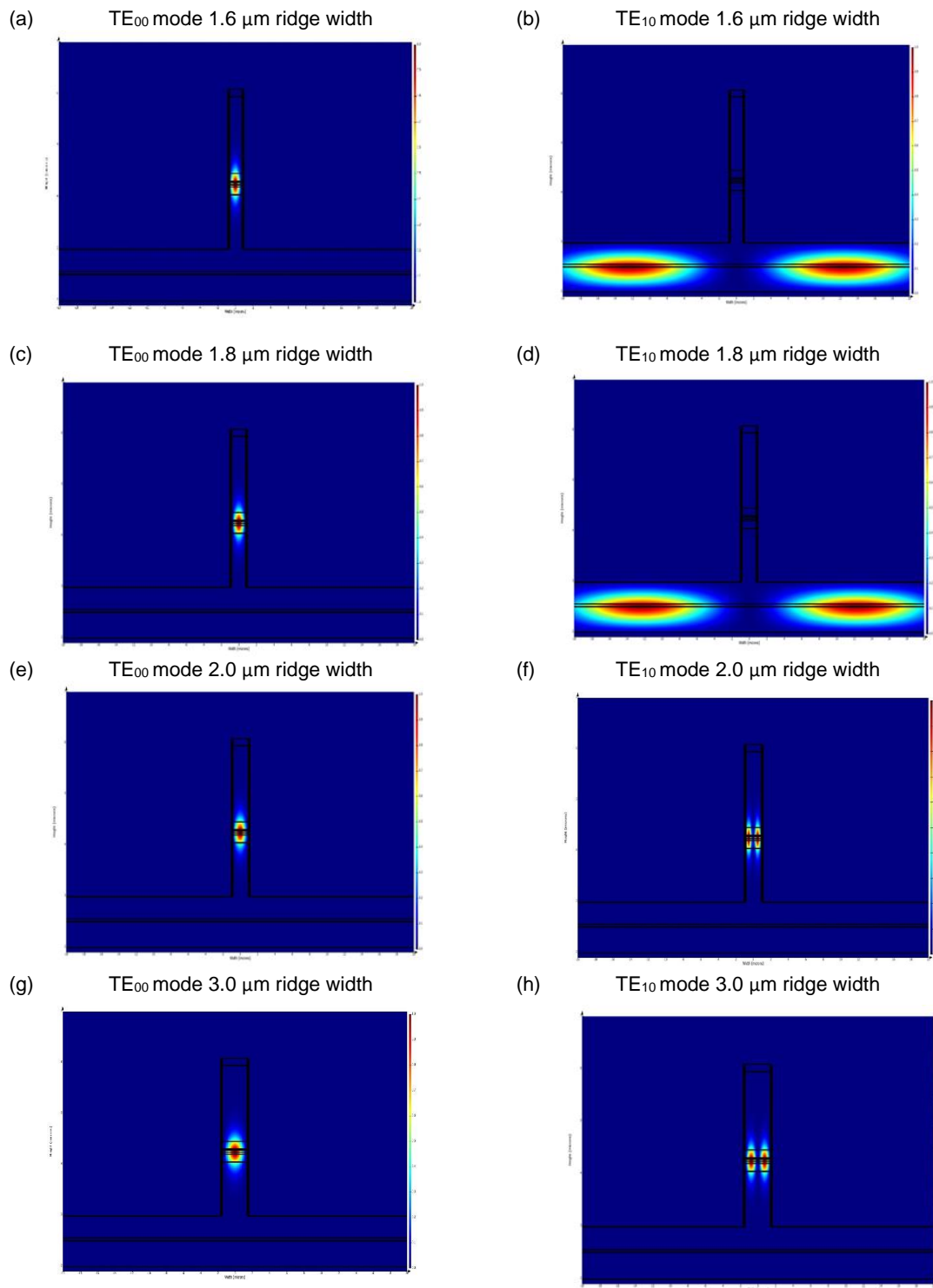
Figure B2(a-h): FDE simulation for deep-etch quantum well structure with varying ridge waveguide width.

Appendix C

Table C: List of typical fabrication and sample preparation stages required for releasing AlGaInAs/InP RWG laser diode devices.

	Step	Process	Details
1	Cleave sample from wafer	Cleave 15 x 15 mm tile from main wafer.	Tile should not be smaller than 15 x 15 mm for a 12 x 12 mm device pattern. Fill out wafer map.
2	Pre-processing solvent clean	Acetone ultrasonic bath (5 mins) Methanol ultrasonic bath (5 mins) IPA ultrasonic bath (5 mins) Rinse DI water and blow dry	Ensure solvent clean is completed in this order.
3	Etch mask deposition	Deposit layer of SiO_2 via PVD	SiO_2 layer should be 600 nm
4	Anneal etch mask	Place sample in RTA to anneal SiO_2 layer	RTA temperature 385 °C
5	Quality check of etch mask	Visually inspect SiO_2 layer Measure thickness of SiO_2 layer	Spectroscopic ellipsometry
6	Spin resist adhesion promoter	Spin a layer of TI Prime onto sample. Bake the TI Prime layer on hot plate.	Spin speed 3500 rpm for 30 s Bake at 110 °C for 120 s Allow to cool for approx. 30 s
7	Spin photoresist	Spin layer of AZ2020 onto sample Bake photoresist on hot plate	Spin speed 3500 rpm for 45 s Bake at 110 °C for 90 s
8	Pattern photoresist	Load sample into DMO Open GDS file Expose sample to transfer pattern	Quality: super Resolution: 0.6 um Wavelength:365 nm
9	Post-exposure bake	Bake sample on hot plate	110 °C for 120 s
10	Develop pattern	Place sample in AZ726 developer solution and rinse in DI water afterwards	Developer for 1 min
11	Plasma ash	Place sample in asher	50 W for 2 mins
12	Etch SiO_2 mask	ICP etching	Recipe (confidential)
13	Remove photoresist	NMP ultrasonic bath (5 mins) Acetone ultrasonic bath (5 mins) IPA ultrasonic soak (5 mins) Nitrogen blow dry Oxygen plasma clean	Plasma clean 100W for 5 mins
14	Etch ridge waveguide	ICP etching	InP etch recipe (confidential)
15	SEM sample	Place sample in SEM to confirm ridge dimensions	If etch dimensions meet spec. continue
16	Etching away remaining SiO_2	Reactive Ion Etch (RIE)	Recipe (confidential)
17	Spin BCB onto sample	Ridge planarisation using BCB	Spin 500 rpm for 45 s

18	Cure BCB layer	**Cure in Carbolite furnace**	**210 ºC for 60 mins**
19	Estimate thickness of BCB	Ellipsometry	
20	Etch BCB	Back-etch BCB to expose capping layer via RIE	Recipe (confidential)
21	Repeat steps 6-10 to prepare sample for metal contact deposition	Photoresist used AZ2035	Adjustment spin speeds and bake times accordingly and adjust DMO settings based on metal contact dimensions
22	Deposit p-type metal contact	Thermal evaporation	10 nm Ti/20 nm Pt/500 nm Au
23	p-type metal contact lift-off process	1165 ultrasonic bath (15 mins) Acetone, IPA rinse, blow dry	Ash at 100W 5 mins
24	Thermal annealing of p-type contact		280 ºC (60 mins)
25	Thinning and polishing InP substrate	Thin to approximately 120 μm thickness Polish (2 mins)	Clean in n-butyl acetate followed by IPA (5 mins)
26	Deposit n-type metal contact	Thermal evaporation	100 nm AuGe/28 nm Ni/300 nm Au
27	Thermal annealing of n-type contact	Thermal evaporation	280 ºC for 60 mins
28	Cleave sample for testing	Diamond tip scriber to cleave required cavity lengths	Clean sample to remove debris and inspect facet
29	Prepare copper blocks and test bards	Mill copper blocks and test boards to required width. Affix copper blocks to test boards using EPOTEK H20E.	Hot plate bake at 180 ºC (3-5 mins)
30	Affix samples to test boards	EPOTEK H20E	Hot plate bake at 180 ºC (1-2 mins)

Appendix D

Figure D1 shows a plot of $\ln|a|$ versus $\dfrac{I}{I_{th}}$ for device J3 at 1550 nm including error bars. The error bars are asymmetrical based on the nature of taking the natural logarithm of the roundtrip amplification factor, a. The ripples across the ASE spectrum were fit with a sine wave using Origin Labs. The error associated with the fit is found to vary based on the amplitude of the resonances, for the different injection current values. At lower injection currents, the ASE spectrum is flatter, less defined, and therefore more challenging to fit. Therefore, the extracted values of P_{max} and P_{min} may have a larger associated error. Consequently, this leads to a larger error in the calculated value of modulation depth, m, and roundtrip amplification factor, a. This explains why the error bars are more significant for the lower normalised current values. This best fit is taken for the average value, represented by the solid black line, which is detailed in Chapter 5. The solid red and blue lines show the fit associated with the maximum and minimum values of $\ln|a|$. The deviations in the two fits account for the maximum and minimum values of reflectivity, $\sqrt{R_1 R_2}$, quoted in Table 5.4. This procedure is repeated for each wavelength.
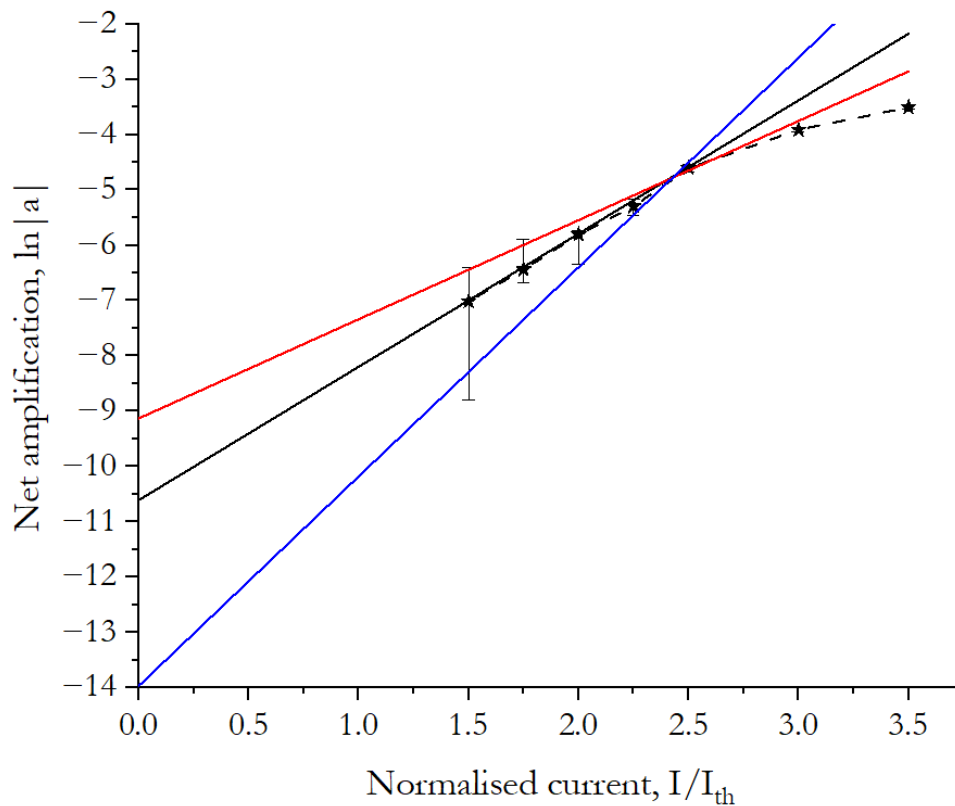
Figure D1: Plot of $\ln|a|$ versus $\dfrac{I}{I_{th}}$ for J3 at 1550 nm with error bars. Red line is fit for the maximum value of $\ln|a|$ and blue line is a fit for the minimum value of $\ln|a|$ due to measured error of m.